9. Nanowires

Mildred S. Dresselhaus, Marcie R. Black, Vincent Meunier, Oded Rabin

This chapter provides an up-to-date overview of research on inorganic nanowires, particularly metallic and semiconducting nanowires. Nanowires are one-dimensional, anisotropic structures, small in diameter, and large in surface-to-volume ratio. Their physical properties are different than those of structures of other scales and dimensionality. While the study of nanowires is particularly challenging, scientists have made immense progress in developing synthetic methodologies for the fabrication of nanowires, developing instrumentation for their characterization, and incorporating nanowires as functional elements in advanced materials and devices. The chapter is divided into three main sections addressing the synthesis, the physical properties, and the applications of nanowires. Yet, the reader will discover many links that make these aspects of nanoscience intimately interdependent.

Nanowires are attracting much interest from those seeking to apply nanotechnology and (especially) those investigating nanoscience. Nanowires, unlike other low-dimensional systems, have two quantum-confined directions but one unconfined direction available for electrical conduction. This allows nanowires to be used in applications where electrical conduction, rather than tunneling transport, is required. Because of their unique density of electronic states, in the limit of small diameters nanowires are expected to exhibit significantly different optical, electrical, and magnetic properties to their bulk three-dimensional (3-D) crystalline counterparts. Increased surface area, very high density of electronic states and joint density of states near the energies of their van Hove singularities, enhanced exciton binding energy, diameter-dependent bandgap, and increased surface scattering for electrons and phonons are just some of the ways in which nanowires differ from their corresponding bulk materials. Yet the sizes of nanowires are typically large enough (> 1 nm in the quantum-confined directions) to result in local crystal structures that are closely related to their parent materials, allowing theoretical predictions about their properties to be made based on knowledge of their bulk properties.

Not only do nanowires exhibit many properties that are similar to, and others that are distinctly different from, those of their bulk counterparts, nanowires also have the advantage from an applications standpoint that material parameters critical for certain properties can be independently controlled in nanowires but not in their bulk counterparts. Certain properties can also be enhanced nonlinearly in small-diameter nanowires, by exploiting the singular aspects of the one-dimensional (1-D) electronic density of states.

Furthermore, nanowires have been shown to provide a promising framework for applying the *bottom-up*

B. Bhushan (Ed.), *Springer Handbook of Nanotechnology*, DOI 10.1007/978-3-319-49347-3_9

approach [9.1] to the design of nanostructures for nanoscience investigations and for potential nanotechnology applications.

Driven by (1) these new research and development opportunities, (2) the smaller and smaller length scales now being used in the semiconductor, optoelectronics, and magnetics industries, and (3) the dramatic development of the biotechnology industry where the action is also at the nanoscale, the nanowire research field has developed with exceptional speed in the last decade. Therefore, a review of the current status of nanowire research is of significant broad interest at the present time. It is the aim of this review to focus on nanowire properties that differ from those of their parent crystalline bulk materials, with an eye toward possible applications that might emerge from the unique properties of nanowires and from future discoveries in this field.

For quick reference, examples of typical nanowires that have been synthesized and studied are listed in Table 9.1. Also of use to the reader are review articles that focus on a comparison between nanowire and nanotube properties [9.2] and the many reviews that have been written about carbon nanotubes [9.3–5], which can be considered as model one-dimensional systems.

9.1 Synthesis

In this section we survey the most common synthetic approaches that have successfully afforded high-quality nanowires of a large variety of materials (Table 9.1). In Sect. 9.1.1, we discuss methods that make use of various templates with nanochannels to confine the nanowire growth in two dimensions. In Sect. 9.1.2, we present the synthesis of nanowires by the vapor–liquid–solid mechanism and its many variations. In Sect. 9.1.3, etching methods for vertically aligned silicon nanowires are reviewed. In Sect. 9.1.4, examples of other synthetic methods of general applicability are presented. The last part of this section (Sect. 9.1.5) features several approaches that have been developed to organize nanowires into simple architectures.

9.1.1 Template-Assisted Synthesis

The template-assisted synthesis of nanowires is a conceptually simple and intuitive way to fabricate nanostructures [9.67–69]. In this context, templates are synthetic or naturally occurring host materials that contain small-diameter cylindrical pores or voids. These empty volumes are filled with a material of choice, which adopts the pore morphology, to form nanowires. In this section, commonly used templates and techniques for filling the templates to make nanowires are described.

Templates and Fabrication Thereof

In template-assisted synthesis of nanostructures, the chemical stability and mechanical properties of the template, as well as the diameter, uniformity, and density of the pores are important characteristics to consider. Templates frequently used for nanowire synthesis include anodic alumina (Al_2O_3) and ion-track–etched polymer films. Both are commercially available (as filtration membranes). Nanochannel glass, mica films, mesoporous materials, block-copolymers, inorganic nanotubes, viruses, and biopolymers have also been used as nanowire templates.

Porous anodic alumina templates are produced by anodizing pure Al films in selected acids [9.70–72]. Under carefully chosen anodization conditions, the resulting oxide film possesses a regular hexagonal array of parallel and nearly cylindrical channels, as shown in Fig. 9.1a. The self-organization of the pore structure in an anodic alumina template involves two coupled processes: pore formation with uniform diameters and pore ordering. The pores form with uniform diameters because of a delicate balance between electric field–enhanced diffusion, which determines the growth rate of the alumina, and dissolution of the alumina into the acidic electrolyte [9.73]. The pores self-order because of mechanical stress at the aluminum-alumina interface due to volume expansion during the anodization process. This stress produces a repulsive force between the pores, causing them to arrange in a close-packed lattice [9.74]. Depending on the anodization conditions, the pore diameter can be systematically varied from ≤ 10 up to 200 nm with a pore density in the range of 10^9–10^{11} pores/cm^2 [9.22, 34, 70, 71]. It has been shown by many groups that the pore size distribution and the pore ordering of the anodic alumina templates can be significantly improved by a two-step anodization technique [9.75–77], where the aluminum oxide layer is dissolved after the first anodization in an acidic solution followed by a second anodization under the same conditions. Alternatively, the locations of the pores can be controlled by pretexturing the surface of the aluminum [9.78, 79].

Track-etched polymer foils are nanowire templates produced by bombardment of polymer films in a heavy-ion accelerator followed by chemical etching [9.81]. The ion-beam bombardment creates latent tracks of

Table 9.1 Selected syntheses of nanowires by material

Material	Growth Technique	Reference
ABO_4-type	Template[a]	[9.6]
Ag	DNA-template, redox	[9.7]
	Template, pulsed ECD[b]	[9.8]
	Liquid-phase	[9.9–11]
Au	Template, ECD[b]	[9.12, 13]
	Liquid-phase	[9.14]
Bi	Stress-induced	[9.15, 16]
	Template, vapor-phase	[9.17]
	Template, ECD[b]	[9.18–20]
	Template, pressure injection	[9.21–23]
BiSb	Pulsed ECD[b]	[9.24]
Bi_2Te_3	Template, DC ECD[b]	[9.25]
CdS	Liquid-phase (surfactant), recrystallization	[9.26]
	Template, AC ECD[b]	[9.27, 28]
CdSe	Liquid-phase (surfactant), redox	[9.29]
	Template, AC ECD[b]	[9.30, 31]
Cu	Vapor deposition	[9.32]
	Template, ECD[b]	[9.33]
Fe	Template, ECD[b]	[9.34, 35]
	Shadow deposition	[9.36]
GaN	Template, CVD[c]	[9.37, 38]
	VLS[d]	[9.39, 40]
GaAs	Template, liquid/vapor MOCVD[e]	[9.41]
Ge	High-T, high-P liquid-phase, redox	[9.42]
	VLS[d]	[9.43]
	Oxide-assisted	[9.44]
InAs	VLS[d]	[9.45]
MgO	VLS[d]	[9.46]
Mo	Step decoration, ECD[b] + redox	[9.47]
Ni	Template, ECD[b]	[9.20, 48, 49]
Pb	Liquid-phase[f]	[9.50]
PbSe	Liquid-phase	[9.51]
	Self-assembly of nanocrystals[g]	[9.52]
Pd	Step decoration, ECD[b]	[9.53]
	Liquid-phase	[9.54]
Se	Liquid-phase, recrystallization	[9.55]
	Template, pressure injection	[9.56]
Si	VLS[d]	[9.57]
	Laser-ablation VLS[d]	[9.58]
	Oxide-assisted	[9.59]
	Low-T VLS[d]	[9.60]
	MACE[h]	[9.61]
W	Vapor transport	[9.62]
Zn	Template, vapor-phase	[9.63]
	Template, ECD[b]	[9.64]
ZnO	VLS[d]	[9.65]
	Template, ECD[b]	[9.64, 66]

[a] Template synthesis, [b] Electrochemical deposition (ECD), [c] Chemical vapor deposition (CVD), [d] Vapor–liquid–solid (VLS) growth, [e] Metalorganic chemical vapor deposition (MOCVD), [f] Liquid phase synthesis, [g] Self-assembly of nanocrystals (in liquid phase), [h] Metal-assisted chemical etching

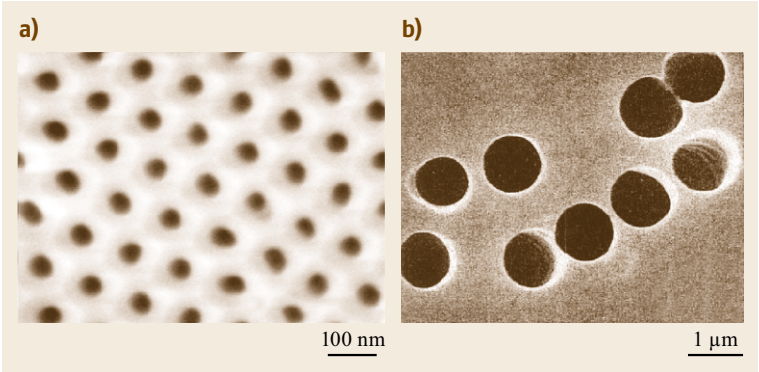

Fig. 9.1 **(a)** Scanning electron microscope (SEM) images of the top surfaces of porous anodic alumina templates anodized with an average pore diameter of 44 nm (after [9.75]). **(b)** SEM image of the particle track-etched polycarbonate membrane, with a pore diameter of 1 μm (after [9.80])

damage in the polymer. These areas are susceptible to chemical etch and can be selectively removed to create hollow channels [9.82]. This technique offers control over pore size, pore aspect ratio, pore shape, and pore density; however, the pores are randomly distributed. Track-etched polycarbonate membranes (Fig. 9.1b) are economical, easy to handle, and dissolve in organic solvents [9.83, 84]. The track-etching technique can be applied also to hard materials: irradiated single-crystal mica films etched with hydrofluoric acid afford nanochannels of diamond-shaped cross-section in a refractory host material [9.48].

Other porous materials can be used as host templates for nanowire growth, as discussed by *Ozin* [9.67]. Nanochannel glass (NCG), for example, contains a regular hexagonal array of glass capillaries similar to the pore structure in anodic alumina with a packing density as high as 3×10^{10} pores/cm^2 [9.68]. Porous Vycor glass that contains an interconnected network of pores less than 10 nm was also employed for the early study of nanostructures [9.85]. The nanochannel array template with the smallest pore diameter may have been identified in mesoporous molecular sieves termed MCM-41 [9.86] that possess hexagonally packed pores with very small channel diameters, which can be varied between 2 and 10 nm. Conducting organic filaments have been fabricated in the nanochannels of MCM-41 [9.87].

Templates for nanowire growth can be produced also using diblock copolymers, polymers that consist of two chain segments of different chemistries covalently linked to each other. When the two components are immiscible in each other, phase segregation occurs, and depending on their volume ratio, spheres, cylinders, or lamellae may self-assemble. To form self-assembled arrays of nanopores:

1. The block copolymer must adopt the cylinder morphology.
2. The cylinders must be parallel and oriented perpendicular to the surface.
3. The component in the cylinders must be etched away selectively.

With polystyrene and polymethylmethacrylate (PMMA) block copolymers (P(S-b-MMA)), by applying an electric field while the copolymer was heated above the glass transition temperature of the two constituent polymers, the self-assembled cylinders of PMMA could be aligned with their main axis perpendicular to the film [9.88]. Selective removal of the PMMA component afforded the preparation of 14 nm-diameter ordered pore arrays with a packing density of 1.9×10^{11} cm^{-3}.

To conclude the list of templates used to fabricate nanowires, we note efforts to utilize biology for the task. Biological systems can produce high-aspect-ratio structures with remarkably consistent dimensions and in high volumes. Coating these filamentous structures with inorganic materials results in useful nanowires. But unlike with the porous templates described above, the nanowire growth is not restricted in any direction; and diameter control is implemented through the process conditions. Additionally, the organic material remains trapped inside the nanowire. For example, the DNA molecule has been used as a template for growing nanometer-sized wires [9.7], as were M13 bacteriophages and the tobacco mosaic virus [9.89–92].

Nanowire Template-Assisted Growth by Pressure Injection

The pressure injection technique can be employed for fabricating highly crystalline nanowires from a low-melting point material in porous templates with robust mechanical strength. In the high-pressure injection method, the nanowires are formed by pressure-injecting the desired material in liquid form into the evacuated pores of the template. Due to the heating and pressurization processes, the templates used for the pressure injection method must be chemically stable and be able to maintain their structural integrity at high tempera-

tures and at high pressures. Anodic aluminum oxide films and nanochannel glass are two typical materials used as templates in conjunction with the pressure-injection filling technique. Metal nanowires (Bi, In, Sn, and Al) and semiconductor nanowires (Se, Te, GaSb, and Bi_2Te_3) have been fabricated in anodic aluminum oxide templates using this method [9.21, 56, 93].

The pressure P required to overcome the surface tension for the liquid material to fill pores with a diameter d_W is determined by the Washburn equation [9.94]

$$d_W = -4\frac{\gamma \cos\theta}{P} ,$$

where γ is the surface tension of the liquid, and θ is the contact angle between the liquid and the template. To reduce the required pressure and to maximize the filling factor, some surfactants are used to decrease the surface tension and the contact angle. For example, the introduction of Cu into the Bi melt can facilitate the filling of the pores in the anodic alumina template with liquid Bi and can increase the number of nanowires that are formed [9.22]. However, some surfactants might cause contamination problems and should therefore be avoided. Nanowires produced by the pressure-injection technique usually possess high crystallinity and a preferred crystal orientation along the wire axis. For example, Fig. 9.2 shows the x-ray diffraction (XRD) patterns of Bi nanowire arrays of three different wire diameters with an injection pressure of ≈ 5000 psi [9.93], showing that the major ($> 80\%$) crystal orientation of the wire axis in the 95 and 40 nm diameter Bi nanowire arrays are, respectively, normal to the (202) and (012) lattice planes, which are denoted by $[10\bar{1}1]$ and $[01\bar{1}2]$ when using a hexagonal unit cell, suggesting a wire diameter–dependent crystal growth direction. On the other hand, 30 and 200 nm Bi nanowires produced using a much higher pressure of $> 20\,000$ psi show a different crystal orientation of (001) along the wire axis [9.23], indicating that the preferred crystal orientation may also depend on applied pressure, with the most dense packing direction along the wire axis for the highest applied pressure.

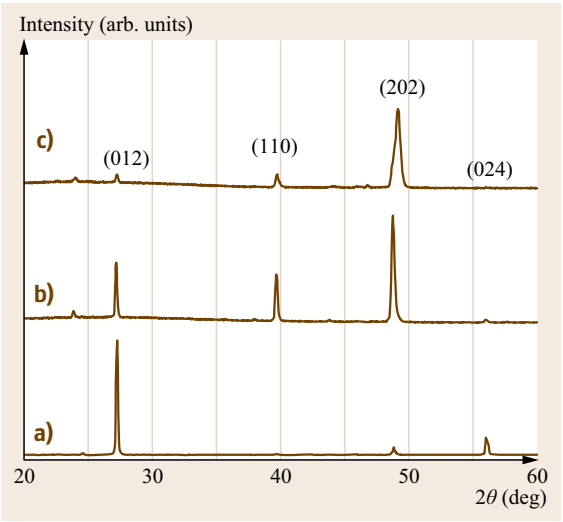

Fig. 9.2a–c XRD patterns of bismuth/anodic alumina nanocomposites with average bismuth wire diameters of **(a)** 40 nm, **(b)** 52 nm, and **(c)** 95 nm [9.93]. The Miller indices corresponding to the lattice planes of bulk Bi are indicated above the individual peaks. The majority of the Bi nanowires are oriented along the $[10\bar{1}1]$ and $[01\bar{1}2]$ directions for $d_W \geq 60$ nm and $d_W \leq 50$ nm respectively (after [9.22, 93]). The existence of more than one dominant orientation in the 52 nm Bi nanowires is attributed to the transitional behavior of *intermediate*-diameter nanowires as the preferential growth orientation is shifted from $[10\bar{1}1]$ to $[01\bar{1}2]$ with decreasing d_W

Electrochemical Deposition

The electrochemical deposition (ECD) technique has attracted increasing attention as a versatile method for fabricating nanowires in templates. Traditionally, electrochemistry has been used to grow thin films on conducting surfaces. Since electrochemical growth is usually controllable in the direction normal to the substrate surface, this method can be readily extended to fabricate 1-D or 0-D nanostructures, if the deposition is confined within the pores of an appropriate template. In the electrochemical methods, a thin conducting metal film is first coated on one side of the porous membrane to serve as the cathode for electroplating. The length of the deposited nanowires can be controlled by varying the duration of the electroplating process. The ECD method has been used to synthesize a wide variety of nanowires, such as metals (Bi [9.18, 84]; Co [9.95, 96]; Fe [9.34, 97]; Cu [9.83, 98]; Ni [9.48, 95]; Ag [9.99]; Au [9.12]); conducting polymers [9.18, 80]; superconductors (Pb [9.100]); compound semiconductors (CdS [9.28]; Bi_2Te_3 [9.25]); and even superlattice nanowires with A/B constituents (such as Cu/Co [9.83, 98]) (Table 9.1). The ECD method offers a low-cost, low-temperature, and rapid approach to template-assisted nanowire synthesis.

In the ECD process, the chosen template has to be chemically stable in the electrolyte during the electroplating process. Cracks and defects in the templates are detrimental to nanowire growth, because deposition rates are higher in the more accessible cracks, leaving most of the nanopores unfilled. Particle-track–etched polymer membranes or mica films are typical templates used in ECD employing a direct current (DC). To use

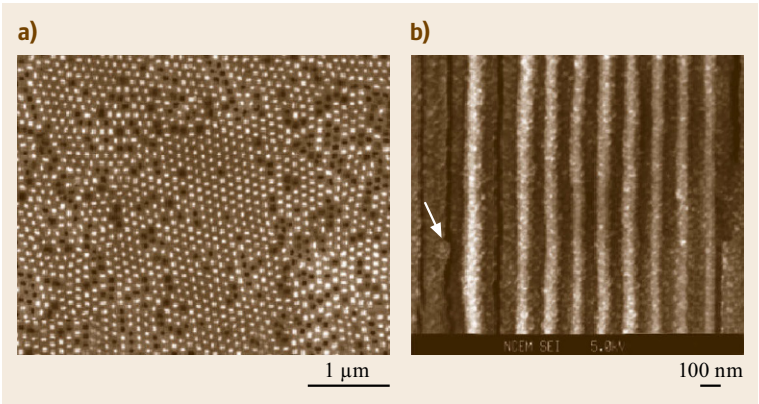

Fig. 9.3 (a) SEM image of a Bi_2Te_3 nanowire array in cross-section showing a relatively high pore filling factor. (b) SEM image of a Bi_2Te_3 nanowire array cross-sectioned along the wire axis (after [9.25])

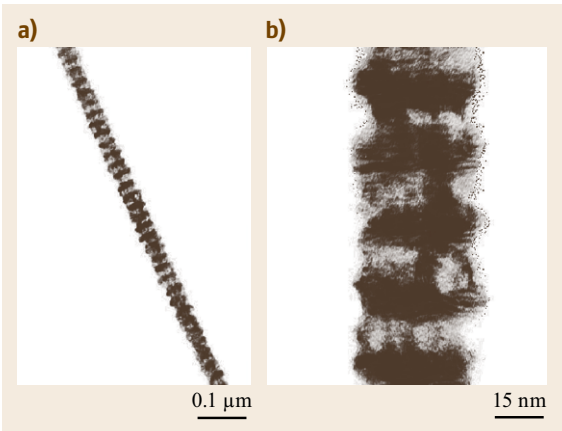

Fig. 9.4 (a) TEM image of a single Co(10 nm)/Cu(10 nm) multilayered nanowire. (b) A selected region of the sample at high magnification (after [9.98])

anodic aluminum oxide films in DC ECD, the insulating barrier layer, separating the pores from the bottom aluminum substrate, has to be removed and a metal film is then evaporated onto the back of the template membrane [9.101]. At the end of the ECD in anodic alumina templates, the surfaces can be polished to even out the variations in nanowire length and reveal the ends of the nanowires. Figure 9.3 presents SEM images of cross-sectional views of a Bi_2Te_3 nanowire array electrodeposited in porous anodic alumina [9.25]. The light areas are associated with Bi_2Te_3 nanowires, the dark regions denote empty pores, and the surrounding gray matrix is alumina. Optimization of the electrochemical conditions and good laboratory practices result in high pore filling factors of close to 100% for ECD methods.

It is possible to employ an alternating current (AC) electrodeposition method in porous anodic alumina templates without the removal of the barrier layer, by utilizing the rectifying properties of the oxide barrier. In AC electrochemical deposition, although the applied voltage is sinusoidal and symmetric, the current is greater during the cathodic half-cycles (deposition current) than in the anodic half-cycles (stripping current). Since no current rectification occurs at defect sites lacking the barrier layer, the deposition and stripping rates are similar and material does not effectively deposit in cracks in the template. In this fashion, metals such as Co [9.96] and Fe [9.34, 97], and semiconductors such as CdS [9.28], have been deposited into the pores of anodic aluminum oxide templates without removing the barrier layer.

In contrast to nanowires synthesized by the pressure injection method, nanowires fabricated by the ECD process are usually polycrystalline, with no preferred crystal orientation, as observed by XRD studies. However, some exceptions exist. For example, anisotropy in crystal growth rates may result in polycrystalline nanowires having a preferred wire growth orientation [9.28]. In addition, *Xu* et al. have prepared a number of single-crystal II–VI semiconductor nanowire arrays, including CdS, CdSe and CdTe, by DC ECD in anodic alumina templates using nonaqueous electrolytes [9.27, 31]. Pulsed electrodeposition techniques can achieve or improve single-crystal nanowire array growth and orientation. The use of pulsed currents is believed to be advantageous for the growth of crystalline wires because the concentration of ions in the electrolyte inside the pores can recover in the period between the electrical pulses and therefore uniform deposition conditions can be produced for each deposition pulse. Single-crystal Ag and Pb nanowires were fabricated by pulse electrodeposition [9.8, 100].

One advantage of the ECD technique is the possibility of fabricating multilayered structures within nanowires. With electrolytes that contain two or more different metal ions, by varying the cathodic potential with time, different metal layers can be controllably

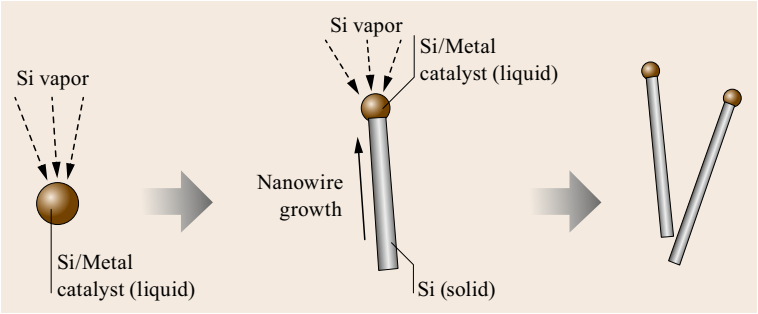

Fig. 9.5 Schematic diagram illustrating the growth of silicon nanowires by the VLS mechanism

deposited in sequence. Co/Cu multilayered nanowires have been synthesized in this way [9.83, 98]. Figure 9.4 shows transmission electron microscopy (TEM) images of a single Co/Cu nanowire about 40 nm in diameter [9.98]. The light bands correspond to Co-rich layers and the dark bands correspond to Cu-rich layers. This electrodeposition method provides a low-cost approach to preparing multilayered 1-D nanostructures.

Vapor Deposition

Vapor deposition of nanowires includes physical vapor deposition (PVD) [9.17], chemical vapor deposition (CVD) [9.38], metalorganic chemical vapor deposition (MOCVD) [9.41] and atomic layer deposition (ALD) [9.102]. Like electrochemical deposition, vapor deposition is usually capable of preparing smaller-diameter (≤ 20 nm) nanowires than pressure injection methods, since surface tension is typically not a barrier for inserting the material into the pores. The main challenge with these techniques is the deposition of material on the surface of the template blocking the pore openings before the pores are filled.

In the PVD process, the material for the nanowires is first vaporized by heat or other means, and is then introduced through the pores of the template and cooled to solidify. Using a specially designed experimental setup [9.17], nearly single-crystal Bi nanowires in anodic aluminum templates with pore diameters as small as 7 nm have been synthesized, and these Bi nanowires were found to possess a preferred crystal growth orientation along the wire axis, similar to the Bi nanowires prepared by pressure injection [9.17, 22].

In the CVD and ALD processes, reacting gas(es) decompose on the surface of the template to form elemental or compound materials. The decomposition is promoted by the CVD reactor temperature and/or a catalyst on the surface. For example, single-crystal GaN nanowires have been synthesized in anodic alumina templates through a gas reaction of Ga_2O vapor with a flowing ammonia atmosphere [9.37, 38]. Templates were filled with TiO_2 by ALD to produce an array of nanowires [9.102], but with high-aspect-ratio pores the ALD product is typically a conformal coating, that is to say, an array of nanotubes [9.103, 104]. A hybrid liquid-/gas-phase CVD approach has been used to prepare polycrystalline GaAs and InAs nanowires in a nanochannel glass array [9.41]. In this method, the nanochannels are filled with one liquid precursor (such as Me_3Ga or Et_3In) via a capillary effect and the nanowires are formed within the template by reactions between the liquid precursor and the other gas reactant (such as AsH_3).

9.1.2 VLS Method for Nanowire Synthesis

A significant number of notable modern syntheses of semiconductor nanowires are based on the so-called vapor–liquid–solid (VLS) mechanism of anisotropic crystal growth. This mechanism was first proposed for the growth of single-crystal silicon whiskers, 100 nm to hundreds of micrometers in diameter [9.105]. The proposed growth mechanism (Fig. 9.5) involves the absorption of source material from the gas phase into a liquid droplet of catalyst (a molten particle of gold on a silicon substrate in the original work [9.105]). Upon supersaturation of the liquid alloy, a nucleation event generates a solid precipitate of the source material. This seed serves as a preferred site for further deposition of material at the interface of the liquid droplet, promoting the elongation of the seed into a nanowire or a whisker, and suppressing further nucleation events on the same catalyst. Since the liquid droplet catalyzes the incorporation of material from the gas source to the growing crystal, the deposit grows anisotropically as a whisker whose diameter is dictated by the diameter of the liquid alloy droplet. The nanowires thus obtained are of high purity, except for the end containing the solidified catalyst as an alloy particle (Figs. 9.5 and 9.6a). Real-time observations of the alloying, nucleation, and elongation steps in the growth of germanium nanowires from gold nanoclusters by the VLS method were recorded by in-situ TEM [9.106].

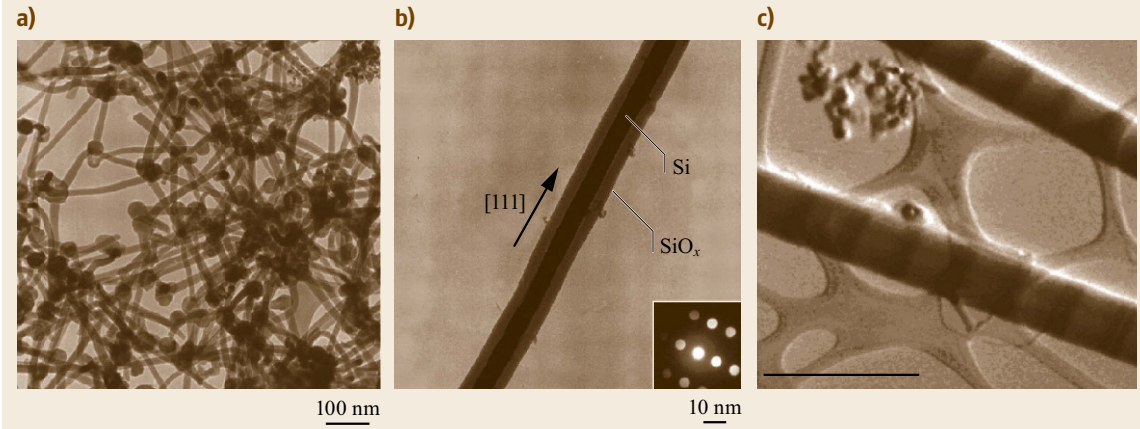

Fig. 9.6 **(a)** TEM images of Si nanowires produced after laser-ablating a $Si_{0.9}Fe_{0.1}$ target. The *dark spheres* with a slightly larger diameter than the wires are solidified catalyst clusters (after [9.58]). **(b)** Diffraction contrast TEM image of a Si nanowire. The crystalline Si core appears *darker* than the amorphous oxide surface layer. The *inset* shows the convergent beam electron diffraction pattern recorded perpendicular to the wire axis, confirming the nanowire crystallinity (after [9.58]). **(c)** Scanning transmission electron microscope (STEM) image of $Si/Si_{1-x}Ge_x$ superlattice nanowires in the bright field mode. The scale bar is 500 nm (after [9.107])

Reduction of the average wire diameter to the nanometer scale requires the generation of nanosized catalyst droplets. However, due to the balance between the liquid-vapor surface free energy and the free energy of condensation, the size of a liquid droplet, in equilibrium with its vapor, is usually limited to the micrometer range. This obstacle has been overcome by several modern methodologies:

1. Advances in the synthesis of metal nanoclusters have made monodispersed nanoparticles commercially available. These can be dispersed on a solid substrate in high dilution so that when the temperature is raised above the melting point, the liquid clusters do not aggregate [9.57].
2. Alternatively, metal islands of nanoscale sizes can self-form when a strained thin layer is grown or heat-treated on a non-epitaxial substrate [9.43].
3. Laser-assisted catalytic VLS growth is a method used to generate nanowires under non-equilibrium conditions. Using laser ablation of a target containing both the catalyst and the source materials, a plasma is generated from which catalyst nanoclusters nucleate as the plasma cools down. Single-crystal nanowires grow as long as the particle remains liquid [9.58].
4. Interestingly, by optimizing the material properties of the catalyst-nanowire system, conditions can be achieved for which nanocrystals nucleate in a liquid catalyst pool supersaturated with the nanowire material, migrate to the surface due to a large surface tension, and continue growing as nanowires perpendicular to the liquid surface [9.60]. In this case, supersaturated nanodroplets are sustained on the outer end of the nanowire due to the low solubility of the nanowire material in the liquid [9.108].

A wide variety of elemental, binary, and compound semiconductor nanowires have been synthesized via the VLS method, and relatively good control over the nanowire diameter and diameter distribution has been achieved. The nanowires are often single crystals with a preferred crystallographic orientation along the wire axis, and may be oriented with respect to the substrate by epitaxy relations [9.109, 110]. Researchers are currently focusing their attention on the controlled variation of the material properties along the nanowire axis. In this context, researchers have modified the VLS synthesis apparatus to generate compositionally modulated nanowires. GaAs/GaP–modulated nanowires have been synthesized by alternately ablating targets of the corresponding materials in the presence of gold nanoparticles [9.111]. p-Si/n-Si nanowires were grown by chemical vapor deposition from alternating gaseous mixtures containing the appropriate dopant [9.111]. $Si/Si_{1-x}Ge_x$ nanowires were grown by combining silicon from a gaseous source with germanium from a periodically ablated target (Fig. 9.6c) [9.107]. NiSi-Si nanowires have been successfully synthesized that directly incorporate a nanowire metal contact into active nanowire devices [9.112]. Finally, using an ultra-high vacuum chamber and molecular beams, InAs/InP

nanowires with atomically sharp interfaces were obtained [9.113]. These compositionally modulated nanowires are expected to exhibit exciting electronic, photonic, and thermoelectric properties.

Interestingly, silicon and germanium nanowires grown by the VLS method consist of a crystalline core coated with a relatively thick amorphous oxide layer (2−3 nm) (Fig. 9.6b). These layers are too thick to be the result of ambient oxidation, and it has been shown that these oxides play an important role in the nanowire growth process [9.59, 114]. Silicon oxides were found to serve as a special and highly selective catalyst that significantly enhances the yield of Si nanowires without the need for metal catalyst particles [9.59, 114, 115]. A similar yield enhancement was also found in the synthesis of Ge nanowires from the laser ablation of Ge powder mixed with GeO_2 [9.44]. The Si and Ge nanowires produced from these metal-free targets generally grow along the [112] crystal direction [9.116], and have the benefit that no catalyst material is found on either ends of the nanowires. Based on these observations and other TEM studies [9.44, 114, 116], an oxide-enhanced nanowire growth mechanism different from the classical VLS mechanism was proposed, where no metal catalyst is required during the laser ablation-assisted synthesis [9.114]. It is postulated that the nanowire growth is dependent on the presence of SiO (or GeO) vapor, which decomposes in the nanowire tip region into both Si (or Ge), which is incorporated into the crystalline phase, and SiO_2 (or GeO_2), which contributes to the outer coating. The initial nucleation events generate oxide-coated spherical nanocrystals. The (112) crystal faces have the fastest growth rate, and therefore the nanocrystals soon begin elongating in the perpendicular direction to form one-dimensional structures. The Si_mO or Ge_mO ($m > 1$) layers on the nanowire tips may be in or near their molten states, catalyzing the incorporation of gas molecules in a directional fashion [9.116]. Besides nanowires with smooth walls, a second morphology of chains of unoriented nanocrystals linked by oxide necks is frequently observed (indicated by an arrow in Fig. 9.7). In addition, scanning tunneling microscope (STM) studies revealed that about 1% of the wires consist of a third morphology: zigzag nanowires 3 nm in diameter and microns in length [9.117]. The recurring structure of two alternating straight wire segments, 10 and 5 nm in length respectively, whose junctions form an angle of 30°, is probably a result of alternating growth along different crystallographic orientations [9.117].

Other variations of the VLS mechanism of nanowire growth include synthesis at low temperatures where the catalysts are solid nanoparticles (i. e., vapor-solid-solid or VSS) [9.109, 118, 119] and synthesis in a liquid phase where the catalyst is suspended in a liquid solution in which the reactants are dissolved (i. e., solution–liquid–solid or SLS) [9.120].

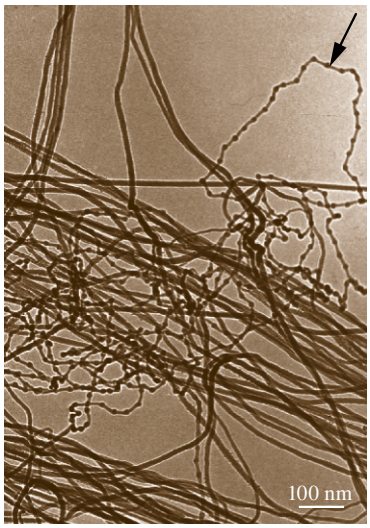

Fig. 9.7 TEM image showing the two major morphologies of Si nanowires prepared by the oxide-assisted growth method (after [9.114]). Notice the absence of metal particles when compared to Fig. 9.6a. The *arrow* points at an oxide-linked chain of Si nanoparticles

9.1.3 Etching Methods

For applications that require uniform nanowires, specific crystallographic orientation, control of the nanowire array dimensions, and/or high-density vertical nanowires, etching methods offer a practical *top-down* alternative method to fabricate nanowire arrays. The two most common methods of making etched nanowires are reactive ion etching (RIE) and metal-assisted chemical etching (MACE). Both methods result in vertically aligned nanowire arrays with high densities. In addition, in versions of both methods, the diameter and density of the nanowires can be controlled. Furthermore, MACE and RIE etched nanowires can result in large arrays of nanowires with uniform heights. Silicon, due to its favorable properties for electronic and photonic applications and its prevalence in the semiconductor industry, is the dominant material used to make etched nanowires.

Reactive ion etching is a vacuum technique used in the semiconductor industry to etch silicon and III–V semiconductors. Energetic charged particles bombarding the substrate remove material by a combination of sputtering and chemical attack. Process engineers have long known that when process conditions are not set a certain way unpatterned regions in the RIE-etched silicon wafers will turn into black silicon [9.121]. The black silicon is in fact a dense array of vertical nanowires, also known as silicon grass. An example of silicon grass is shown in Fig. 9.8. While unwanted by the complementary metal-oxide-semiconductor (CMOS)

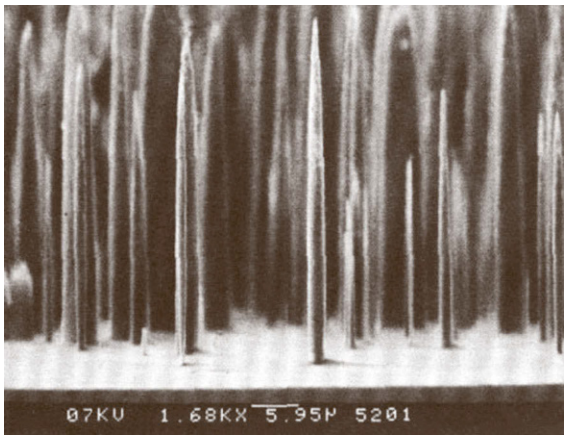

Fig. 9.8 A SEM image of silicon grass formed by RIE. ©IOP Publishing. Reproduced with permission. All rights reserved (after [9.121])

industry, black silicon has proven useful for making and studying nanowire arrays. Ultimately, RIE methods have been used to form patterned silicon nanowire arrays in a controllable fashion. RIE and often deep RIE (DRIE) are used in combination with a mask to pattern where nanowires form [9.122]. The ordered arrays of vertical nanowires shown in Fig. 9.9 are examples of wire arrays formed by using e-beam lithography in combination with deep RIE.

Metal-assisted chemical etching to make silicon nanowire arrays is a well explored research topic. The resulting silicon structure made from MACE is often called *black silicon*, *silicon whiskers*, *nanotexture*, *porous silicon,* or *nanowires*. Recently several reviews have covered the process and the capabilities of MACE [9.123–125]. In MACE a thin metal is deposited onto a silicon surface and then immersed into an etch solution containing hydrofluoric acid and an oxidizer. The metal catalyzes the etching of silicon. Thus silicon is etched where the metal is in contact with the silicon and is not etched where the metal is absent. As the etching progresses, the metal moves down the silicon with the etching front. In the case where the metal is put down such that there are holes in the metal, nanowires form as the metal etches the silicon around the nanowires. MACE results in very anisotropic etched structures. See Fig. 9.10 for an example of a MACE-etched array of nanowires. In this particular example, the metal was masked using a silica colloidal crystal template such that the metal was blocked from touching the silicon wherever a silica sphere was present, thus forming a nanowire [9.61].

9.1.4 Other Synthesis Methods

In this section we review several other general procedures available for the synthesis of a variety of nanowires. We focus on *bottom-up* approaches, which afford many kinds of nanowires in large numbers, and do not require highly sophisticated equipment (such as scanning microscopy or lithography-based methods), and exclude cases for which the nanowires are not self-sustained (such as in the case of atomic rows on the surface of crystals).

A solution-phase synthesis of nanowires with controllable diameters has been demonstrated [9.55, 126], without the use of templates, catalysts, or surfactants.

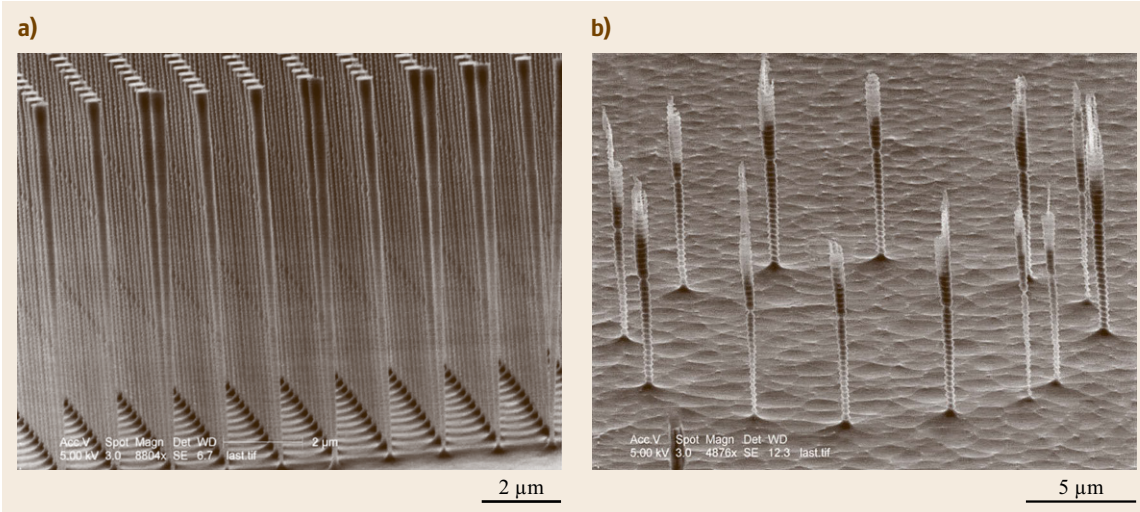

Fig. 9.9 Examples of patterned RIE etched nanowires. In these examples the RIE was patterned by using e-beam lithography. Copyright 2009, American Vacuum Society. Reprinted with permission from [9.122]

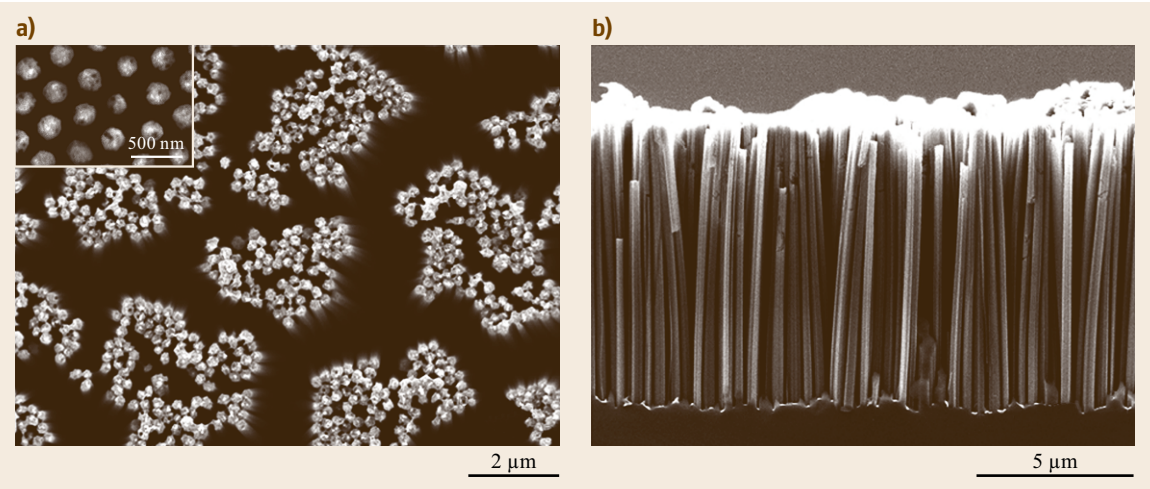

Fig. 9.10a,b MACE silicon nanowires formed by masking the metal with colloidal silica spheres. The silicon is etched wherever the metal touches the silicon. The nanowires form where the metal is blocked from touching the silicon. **(a)** Top view and **(b)** cross-section view of the array. The long nanowires bundle at the tips during drying, while short nanowires (up to 1 µm) retain the arrangement of the silica spheres (*inset*). (Reprinted from [9.61], with permission of AIP Publishing)

Instead, Gates et al. make use of the anisotropy of the crystal structure of trigonal selenium and tellurium, which can be viewed as rows of 1-D helical atomic chains. Their approach is based on the mass transfer of atoms during an aging step from a high free-energy solid phase (e.g., amorphous selenium) to a seed (e.g., trigonal selenium nanocrystal), which grows preferentially along one crystallographic axis. The lateral dimension of the seed, which dictates the diameter of the nanowire, can be controlled by the temperature of the nucleation step. Furthermore, Se/Te alloy nanowires were synthesized by this method, and Ag_2Se compound nanowires were obtained by treating selenium nanowires with $AgNO_3$ [9.127–129]. In a separate work, tellurium nanowires were transformed into Bi_2Te_3 nanowires by their reaction with $BiPh_3$ [9.130].

More often, however, the use of surfactants is necessary to promote the anisotropic 1-D growth of nanocrystals in solution. Solution-phase synthetic routes have been optimized to produce monodispersed quantum dots (zero-dimensional isotropic nanocrystals) [9.131]. Surfactants are necessary in this case to stabilize the interfaces of the nanoparticles and to retard oxidation and aggregation processes. Detailed studies on the effect of growth conditions revealed that they can be manipulated to induce a directional growth of the nanocrystals, usually generating nanorods (aspect ratio of ≈ 10), and in favorable cases, nanowires with high aspect ratios. *Heath* and *LeGoues* synthesized germanium nanowires by reducing a mixture of $GeCl_4$ and phenyl-$GeCl_3$ at high temperature and high pressure. The phenyl ligand was essential for the formation of high-aspect-ratio nanowires [9.42]. In growing CdSe nanorods [9.29], *Alivisatos* et al. used a mixture of two surfactants, whose concentration ratio influenced the shape of the nanocrystal. It is believed that different surfactants have different affinities, and different absorption rates, for the different crystal faces of CdSe, thereby regulating the growth rates of these faces. In the liquid-phase synthesis of Bi nanowires, the additive $NaN(SiMe_3)_2$ induces the growth of nanowires oriented along the [110] crystal direction from small bismuth seed clusters, while water solely retarded the growth along the [001] direction, inducing the growth of hexagonal-plate particles [9.130]. A coordinating alkyl-diamine solvent was used to grow polycrystalline PbSe nanowires at low temperatures [9.51]. Here, the surfactant-induced directional growth is believed to occur through the formation of organometallic complexes in which the bidentate ligand assumes the equatorial positions, thus hindering the ions from approaching each other in this plane. Additionally, the alkyl-diamine molecules coat the external surface of the wire, preventing lateral growth. The aspect ratio of the wires increased as the temperature was lowered in the range $10\,°C < T < 117\,°C$. Noble metal nanowires were grown by the polyol-reduction method utilizing polyvinylpyrrolidone as a surfactant [9.9–11, 54]. These nanowires have a pentagonal cross-section. The 1-D growth is a consequence of extending the twin boundaries in the dodecahedral seed nanoparticles that

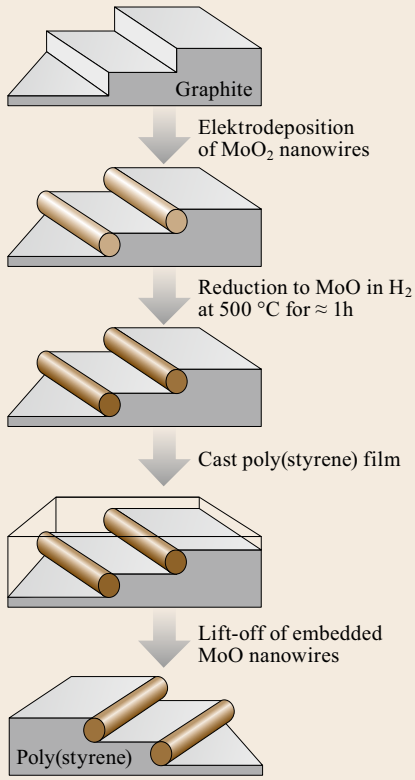

Fig. 9.11 Schematic of the electrodeposition step edge decoration of HOPG (highly oriented pyrolytic graphite) for the synthesis of molybdenum nanowires (after [9.47, 132])

form upon nucleation and passivation of the (100) surfaces by the surfactant.

Stress-induced crystalline bismuth nanowires have been grown from sputtered films of layers of Bi and CrN. The nanowires presumably grow from defects and cleavage fractures in the film, and are up to several millimeters in length with diameters ranging from 30 to 200 nm [9.15]. Other elemental and metal chalcogenide nanowires of soft, low-melting point metals (Bi, Pb, Ga) have been observed to grow from polycrystalline films under stress. This approach offers the benefits of being low-cost and free of contaminants [9.16, 133, 134].

Selective electrodeposition along the step edges in highly oriented pyrolytic graphite (HOPG) was used to obtain MoO_2 nanowires as shown in Fig. 9.11. The site selectivity was achieved by applying a low overpotential to the electrochemical cell in which the HOPG served as cathode, thus minimizing the nucleation events on less favorable sites (i. e., plateaus). While these nanowires cannot be removed from the substrate, they can be reduced to metallic molybdenum

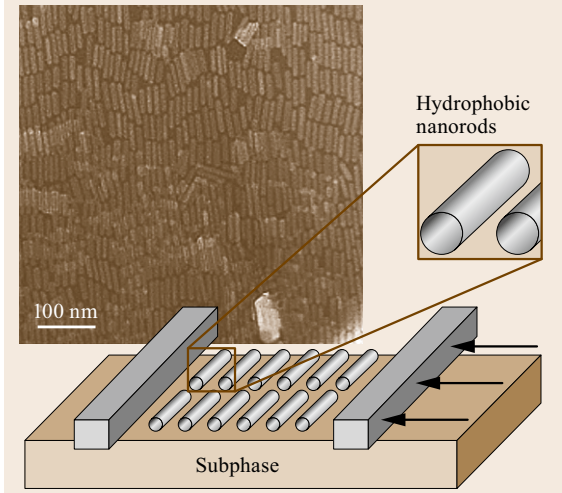

Fig. 9.12 A TEM image of a smectic phase of a $BaCrO_4$ nanorod film (*left inset*) achieved by the Langmuir–Blodgett technique, as depicted by the illustration (after [9.136])

nanowires, which can then be released as free-standing nanowires. Other metallic nanowires were also obtained by this method [9.47, 132]. In contrast to the template synthesis approaches described above, in this method the substrate only defines the position and orientation of the nanowire, not its diameter. In this context, other surface morphologies, such as self-assembled grooves in etched crystal planes, have been used to generate nanowire arrays via gas-phase shadow deposition (for example, Fe nanowires on (110)NaCl [9.36]). The cross-section of artificially prepared superlattice structures has also been used for site-selective deposition of parallel and closely spaced nanowires [9.135]. Nanowires prepared on the above-mentioned substrates have semicircular, rectangular, or other unconventional cross-sectional shapes.

9.1.5 Nanowire Alignment and Superstructures of Nanowires

Controlling the position of a nanowire in the growth process is important for preparing devices or test structures containing nanowires, especially when it involves a large array of nanowires. Post-synthesis methods to align and position nanowires include microfluidic channels [9.137], Langmuir–Blodgett assemblies [9.136], and electric-field–assisted assembly [9.138]. The first method involves the orientation of the nanowires by the liquid flow direction when a nanowire solution is injected into a microfluidic channel assembly and by the interaction of the nanowires with the side walls of

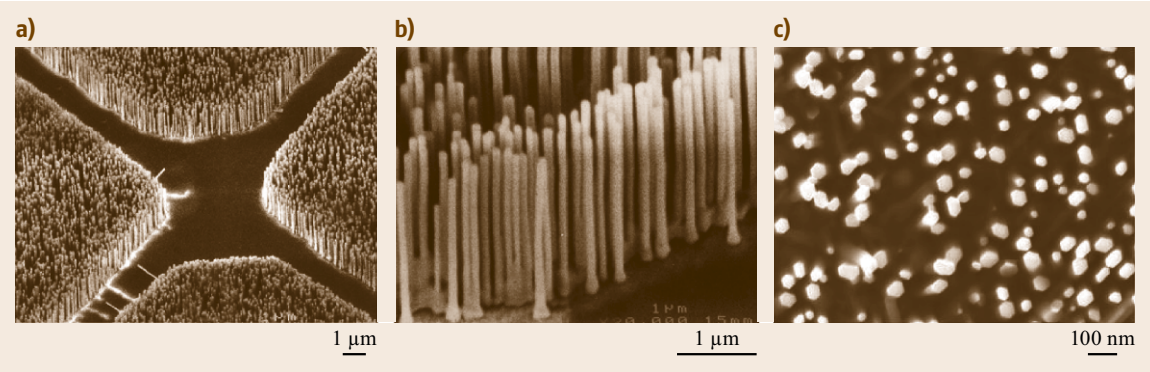

Fig. 9.13a–c SEM images of ZnO nanowire arrays grown on a sapphire substrate, where **(a)** shows patterned growth, **(b)** shows a higher-resolution image of the parallel alignment of the nanowires, and **(c)** shows the faceted side-walls and the hexagonal cross-section of the nanowires. For nanowire growth, the sapphire substrates were coated with a 1.0–3.5 nm-thick patterned layer of Au as the catalyst, using a TEM grid as the shadow mask. These nanowires have been used for nanowire laser applications (after [9.110])

the channel. The second method involves the alignment of nanowires at a liquid-gas or liquid-liquid interface by the application of compressive forces on the interface (Fig. 9.12). The aligned nanowire films can then be transferred onto a substrate and lithography methods can be used to define interconnects. This allows the nanowires to be organized with a controlled alignment and spacing over large areas. Using this method, centimeter-scale arrays containing thousands of single silicon nanowire field-effect transistors with high performance could be assembled to make large-scale nanowire circuits and devices [9.139, 140]. The third technique is based on dielectrophoretic forces that pull polarizable nanowires toward regions of high field strength [9.141, 142]. The nanowires align between two isolated electrodes that are capacitively coupled to a pair of buried electrodes biased with an AC voltage. Once a nanowire shorts the electrodes, the electric field is eliminated, preventing more nanowires from depositing. The above techniques have been successfully used to prepare electronic circuitry and optical devices out of nanowires (Sects. 9.3.1 and 9.3.2). Alternatively, alignment and positioning of the nanowires can be specified and controlled during their growth by the proper design of the synthesis method. For example, ZnO nanowires prepared by the VLS method were grown into an array in which both their position on the substrate and their growth direction and orientation were controlled [9.65]. The nanowire growth region was defined by patterning the gold film, which serves as a catalyst for the ZnO nanowire growth, employing soft lithography, e-beam lithography, or photolithography. The orientation of the nanowires was achieved by selecting a substrate with a lattice structure matching that of the nanowire material to facilitate the epitaxial growth. These conditions result in an array of nanowire posts at predetermined positions, all vertically aligned with the same crystal growth orientation (Fig. 9.13). Similarly, GaN nanowire arrays have been synthesized epitaxially on (100)$LiAlO_2$ and (111)MgO single-crystal substrates. The lattice matching conditions enabled control over the crystallographic growth directions of the nanowires. For example, GaN nanowires on (100)$LiAlO_2$ substrates grow oriented along the [110] direction, whereas (111)MgO substrates result in the growth of GaN nanowires with an [001] orientation, due to the different lattice-matching constraints [9.143]. A similar structure could be obtained by the template-mediated electrochemical synthesis of nanowires (Sect. 9.1.1), particularly if anodic alumina with its parallel and ordered channels is used. The control over the location of the nucleation of nanowires in the electrochemical deposition is determined by the pore positions and the back-electrode geometry. The pore positions can be precisely controlled by imprint lithography [9.78]. By growing the template on a patterned conductive substrate that serves as a back-electrode [9.144–146], different materials can be deposited in the pores at different regions of the template.

9.2 Characterization and Physical Properties of Nanowires

In this section we review the structure and properties of nanowires and their interrelationship. The discovery and investigation of nanostructures were spurred on by advances in various characterization and microscopy techniques that enabled material characterization to take place at smaller and smaller length scales, reaching length scales down to individual atoms. For applications, characterizing the structural properties of nanowires is especially important, so that a reproducible relationship between their desired functionality and their geometrical and structural characteristics can be established. Due to the enhanced surface-to-volume ratio in nanowires, their properties may depend sensitively on their surface conditions and geometrical configurations. Even nanowires made of the same material may possess dissimilar properties due to differences in their crystal phase, crystalline size, surface conditions, and aspect ratios, which depend on the synthesis methods and conditions used in their preparation.

9.2.1 Structural Characterization

Structural and geometric factors play an important role in determining the various attributes of nanowires, such as their electrical, optical, and magnetic properties. Therefore, various novel tools have been developed and employed to obtain this important structural information at the nanoscale. At the micrometer scale, optical techniques are extensively used for imaging structural features. Since the sizes of nanowires are usually comparable to or, in most cases, much smaller than the wavelength of visible light, traditional optical microscopy techniques are usually limited when characterizing the morphology and surface features of nanowires. Therefore, electron microscopy techniques play a more dominant role at the nanoscale. Since electrons interact with matter more strongly than photons, electron microscopy is particularly sensitive relative to x-rays for the analysis of tiny samples.

In this section we review and give examples of how scanning electron microscopy, transmission electron microscopy, scanning probe spectroscopies, and diffraction techniques are used to characterize the structure of nanowires. To provide the necessary basis for developing reliable structure-property relations, multiple characterization tools are applied to the same samples.

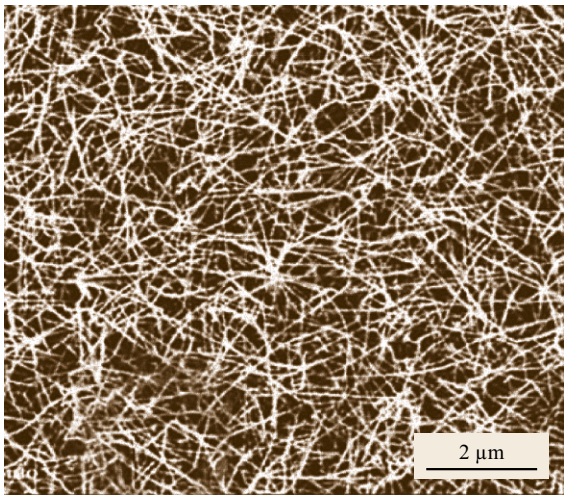

Fig. 9.14 SEM image of GaN nanowires in a mat arrangement synthesized by laser-assisted catalytic growth. The nanowires have diameters and lengths on the order of 10 nm and 10 μm respectively (after [9.39])

Scanning Electron Microscopy

SEM usually produces images down to length scales of ≈ 10 nm and provides valuable information regarding the structural arrangement, spatial distribution, wire density, and geometrical features of the nanowires. The examples of SEM micrographs shown in Figs. 9.1 and 9.3 indicate that structural features at the 10 nm to 10 μm length scales can be probed, providing information on the size, size distribution, shapes, spatial distributions, density, alignment, fill-factors, granularity, etc. As another example, Fig. 9.13a shows an SEM image of ZnO nanowire arrays grown on a sapphire substrate [9.110], which provides evidence for the non-uniform spatial distribution of the nanowires on the substrate, which was attained by patterning the catalyst film to define high-density growth regions and nanowire-free regions. Figure 9.13b, showing a higher magnification of the same system, indicates that these ZnO nanowires grow perpendicular to the substrate, are well aligned with approximately equal wire lengths, and have wire diameters in the range 20−150 nm. The SEM micrograph in Fig. 9.13c provides further information about the surface of the nanowires, showing it to be well faceted, forming a hexagonal cross-section, indicative of nanowire growth normal to the (0001) plane. Both the uniformity of the nanowires' size, their alignment perpendicular to the substrate, and their uniform growth direction, as suggested by the SEM data, are linked to the good epitaxial interface between the (0001) plane of the ZnO nanowire and the (110) plane of the sapphire substrate. (The crystal structures of ZnO and sapphire are essentially incommensurate, with the exception that the *a*-axis of

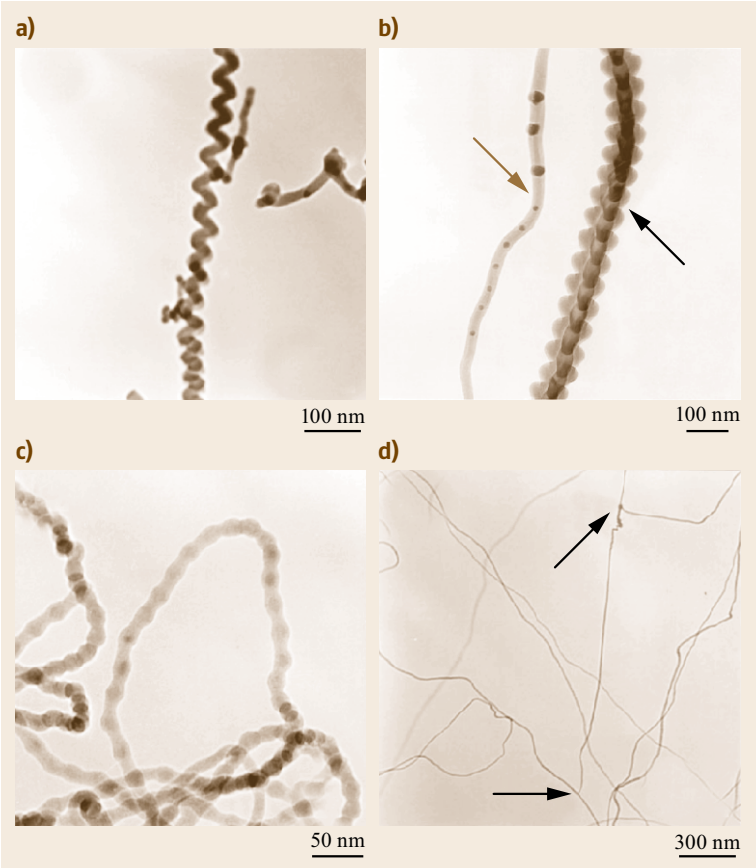

Fig. 9.15a–d TEM morphologies of four special forms of Si nanowires synthesized by the laser ablation of a Si powder target. **(a)** A spring-shaped Si nanowire; **(b)** fishbone-shaped (indicated by a *black arrow*) and frogs' egg-shaped (indicated by a *brown arrow*) Si nanowires; and **(c)** pearl-shaped nanowires. **(d)** shows polysites for the nucleation of silicon nanowires (indicated by *arrows*) (after [9.147])

ZnO and the *c*-axis of sapphire are related almost exactly by a factor of four, with a mismatch of less than 0.08% at room temperature [9.110].) The well-faceted nature of these nanowires has important implications for their lasing action (Sect. 9.3.2). The SEM image of GaN nanowires synthesized by a laser-assisted catalytic growth method [9.39] featured in Fig. 9.14 revals that random spatial orientation of the nanowire axes and a wide diameter distribution for these nanowires, in contrast to the ZnO wires in Fig. 9.13 and to arrays of well-aligned nanowires prepared by template-assisted growth (Fig. 9.3).

Transmission Electron Microscopy

TEM and high-resolution transmission electron microscopy (HRTEM) are powerful imaging tools for studying nanowires at the atomic scale, and they usually provide more detailed geometrical features than are seen in SEM images (SAED). As an example, the TEM images in Fig. 9.15a–c show four different morphologies for Si nanowires prepared by the laser ablation of a Si target: spring-shaped, fishbone-shaped, frogs' egg-shaped, and pearl-shaped nanowires [9.147].

TEM studies also yield information regarding the crystal structure, crystal quality, grain size, and crystal orientation of the nanowire axis. The crystal quality of nanowires is revealed from high-resolution TEM images with atomic resolution, along with selected area electron diffraction (SAED) patterns. For example, Fig. 9.16 shows a TEM image of one of the GaN nanowires from Fig. 9.14, indicating single crystallinity and showing (100) lattice planes, thus indicating the growth direction of the nanowire. This information is supplemented by the corresponding electron diffraction pattern in the upper right. A more comprehensive review of the application of TEM for growth orientation indexing and crystal defect characterization in nanowires is available elsewhere [9.148].

The high resolution of the TEM also permits the surface structures of the nanowires to be studied. In many cases, the nanowires are sheathed with native oxides, an amorphous oxide layer that forms during the growth process. This can be seen in Fig. 9.6b for silicon nanowires and in Fig. 9.17 for germanium nanowires [9.44], showing a mass-thickness contrast TEM image and a selected area electron diffraction pattern of a Ge nano-

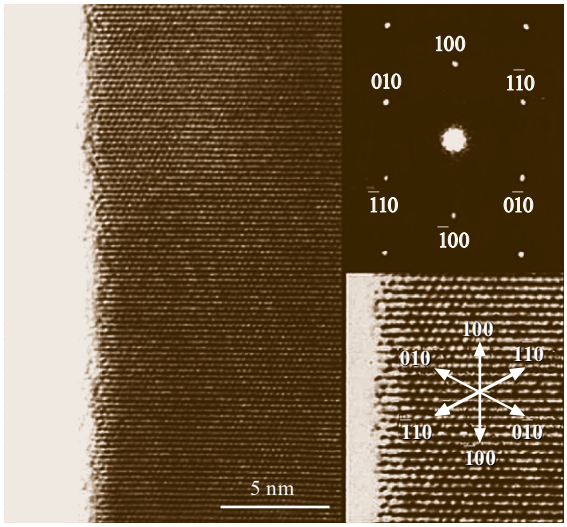

Fig. 9.16 Lattice-resolved high-resolution TEM image of one GaN nanowire (*left*) showing that (100) lattice planes are visible perpendicular to the wire axis. The electron diffraction pattern (*top right*) was recorded along the [001] zone axis. A lattice-resolved TEM image (*lower right*) highlights the continuity of the lattice up to the nanowire edge, where a thin native oxide layer is found. The directions of various crystallographic planes are indicated in the *lower right figure* (after [9.39])

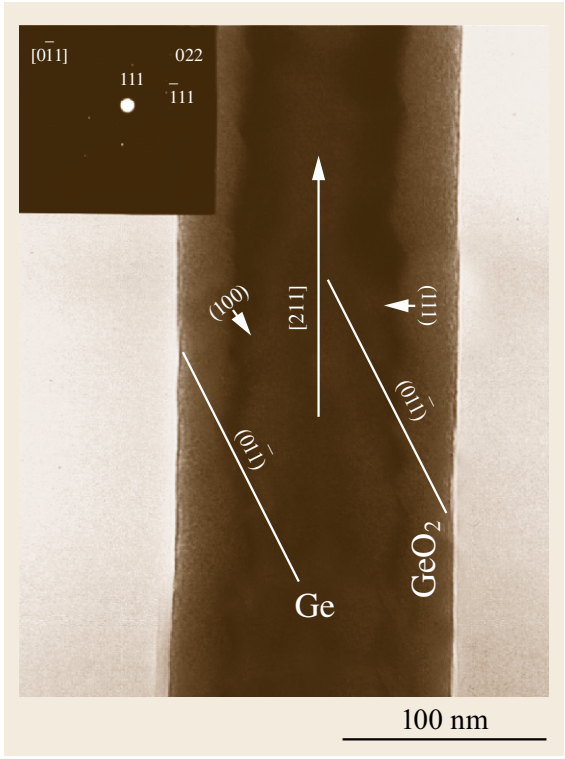

Fig. 9.17 A mass-thickness contrast TEM image of a Ge nanowire taken along the $(0\bar{1}1)$ zone axis and a selected area electron diffraction pattern (*upper left inset*) (after [9.44]). The Ge nanowires were synthesized by laser ablation of a mixture of Ge and GeO_2 powder. The core of the Ge nanowire is crystalline, while the surface GeO_2 is amorphous

wire. The main TEM image shows that these Ge nanowires possess an amorphous GeO_2 sheath with a crystalline Ge core that is oriented in the [211] direction.

Dynamical processes of the surface layer of nanowires can be studied in situ using an environmental TEM chamber, which allows TEM observations to be made while different gases are introduced or as the sample is heat treated at various temperatures, as illustrated in Fig. 9.18. The figure shows high-resolution TEM images of a Bi nanowire before and after a dynamic oxide removal process carried out within the environmental chamber of the TEM [9.149]. The amorphous bismuth-oxide layer coating the nanowire (Fig. 9.18a) is removed by exposure to hydrogen gas within the environmental chamber of the TEM, as indicated in Fig. 9.18b.

By coupling the powerful imaging capabilities of TEM with other characterization tools, such as an electron energy loss spectrometer (EELS) or an energy dispersive x-ray spectrometer (EDS) within the TEM instrument, additional properties of the nanowires can be probed with high spatial resolution. With the EELS technique, the energy and momentum of the incident and scattered electrons are measured in an inelastic electron scattering process to provide information on the energy and momentum of the excitations in the nanowire sample. Figure 9.19 shows the dependence on nanowire diameter of the electron energy loss spectra of Bi nanowires. The spectra were taken from the center of the nanowire, and the shift in the energy of the peak position (Fig. 9.19) indicates the effect of the nanowire diameter on the plasmon frequency in the nanowires. The results show that there are changes in the electronic structure of the Bi nanowires as the wire diameter decreases [9.150]. Such changes in electronic structure as a function of nanowire diameter are also observed in their transport (Sect. 9.2.2) and optical (Sect. 9.2.3) properties, and are related to quantum confinement effects.

EDS measures the energy and intensity distribution of x-rays generated by the impact of the electron beam on the surface of the sample. The elemental composition within the probed area can be determined to a high degree of precision. The technique was par-

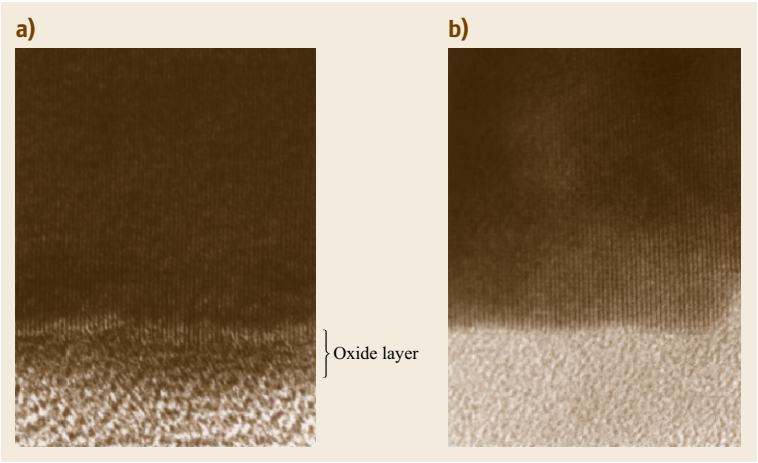

Fig. 9.18 High-resolution transmission electron microscope (HRTEM) image of a Bi nanowire **(a)** before and **(b)** after annealing in hydrogen gas at 130 °C for 6 h within the environmental chamber of the HRTEM instrument to remove the oxide surface layer (after [9.149])

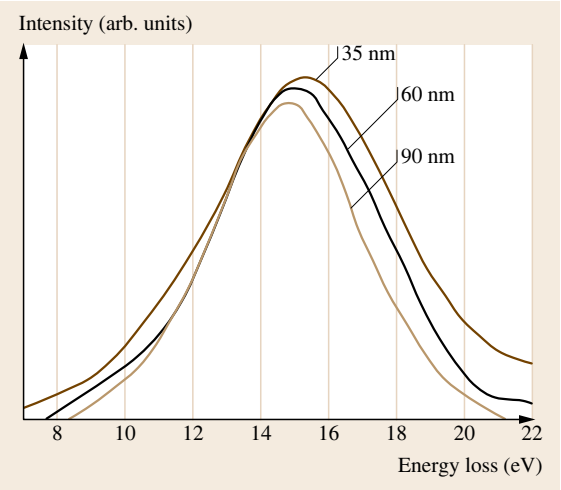

Fig. 9.19 Electron energy loss spectra (EELS) taken from the centers of bismuth nanowires with diameters of 35, 60 and 90 nm. The shift in the volume plasmon peaks is due to the effect of wire diameter on the electronic structure (after [9.150])

ticularly useful for the compositional characterization of superlattice nanowires [9.107] and core-shell nanowires [9.151] (Sect. 9.1.2).

Scanning Probe Techniques

Several scanning probe techniques, such as scanning tunneling microscopy (STM) [9.152], electric field gradient microscopy (EFM) [9.22], magnetic force microscopy (MFM) [9.49], and scanning thermal microscopy (SThM) [9.153], combined with atomic force microscopy (AFM), have been employed to study the structural, electronic, magnetic, and thermal properties of nanowires. A scanning tunneling microscope can be employed to reveal both topographical structural information, such as that illustrated in Fig. 9.20, as well as information on the local electronic density of states of a nanowire, when used in the STS (scanning tunneling spectroscopy) mode. Figure 9.20 shows STM height images (taken in the constant-current STM mode) of MoSe molecular wires deposited from a methanol or acetonitrile solution of $Li_2Mo_6Se_6$ onto Au substrates. The STM image of a single MoSe wire (Fig. 9.20a) exhibits a 0.45 nm lattice repeat distance in a MoSe molecular wire. When both STM and STS measurements are made on the same sample, the electronic and structural properties can be correlated. For example, joint STM/STS studies on Si nanowires [9.117] identified on single nanowires alternating segments grown along the [110] and [112] directions, and different I–V characteristics were measured for the [110] segments as compared with the [112] segments.

Magnetic force microscopy (MFM) has been employed to study magnetic polarization of magnetic nanowires embedded in an insulating template, such as an anodic alumina template. For example, Fig. 9.21a shows the topographic image of an anodic alumina template filled with Ni nanowires recorded in AFM mode, and Fig. 9.21b demonstrates the corresponding magnetic polarization of each nanowire in the template. This micrograph shows that an MFM probe can distinguish between spin-up and spin-down nanowires in the nanowire array, thereby providing a method for measuring magnetic dipolar interactions between wires [9.49].

X-ray Analysis

Other characterization techniques that are commonly used to study the crystal structures and chemical compositions of nanowires include x-ray diffraction and energy-dispersive x-ray spectroscopy (EDS). The peak positions in the x-ray diffraction pattern can used to determine the chemical composition and the crystal phase

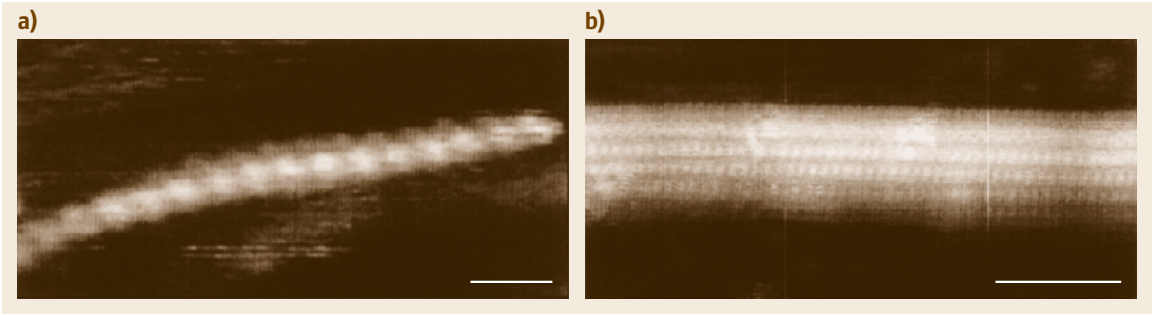

Fig. 9.20a,b STM height images, obtained in the constant-current mode, of MoSe chains deposited on an Au(111) substrate. **(a)** A single chain image, and **(b)** a MoSe wire bundle (after [9.152]). Scale bars: 1 nm

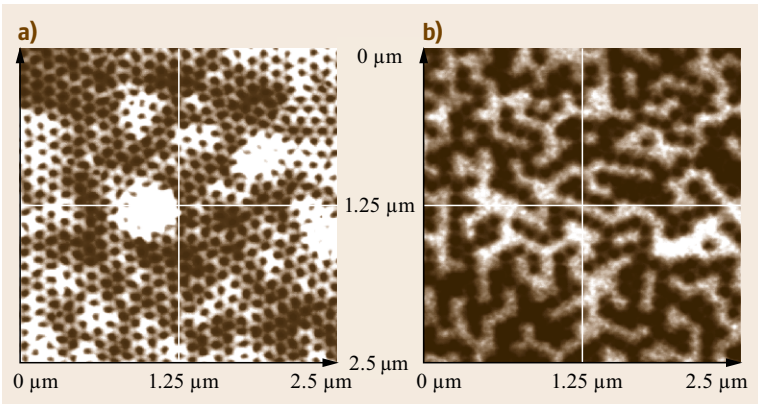

Fig. 9.21 **(a)** Topographic image of a highly ordered porous alumina template with a period of 100 nm filled with 35 nm-diameter nickel nanowires. **(b)** The corresponding MFM (magnetic force microscopy) image of the nano-magnet array, showing that the pillars are magnetized alternately *up* (*white*) and *down* (*black*) (after [9.49])

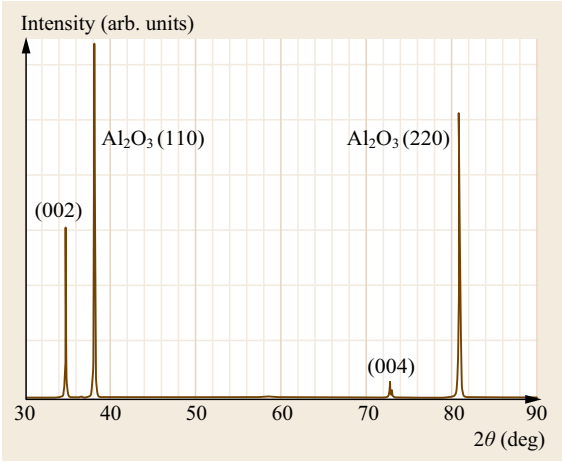

Fig. 9.22 X-ray diffraction pattern of aligned ZnO nanowires (Fig. 9.13) grown on a sapphire substrate. Only (00ℓ) diffraction peaks are observed for the nanowires, owing to their well-oriented growth orientation. Strong diffraction peaks for the sapphire substrate are found (after [9.110])

structure of the nanowires. For example, Fig. 9.2 shows that Bi nanowires have the same crystal structure and lattice constants as bulk bismuth. Both the x-ray diffraction pattern (XRD) for an array of aligned Bi nanowires (Fig. 9.2) and the SAED pattern for individual Bi nanowires [9.22] suggest that the nanowires have a common crystallographic alignment.

As another example of an XRD pattern for an array of aligned nanowires, Fig. 9.22 shows the x-ray diffraction pattern of the ZnO nanowires that are displayed in Fig. 9.13. Only (00ℓ) diffraction peaks are observed for these aligned ZnO nanowires, indicating that their preferred growth direction is [001] along the wire axis. Similarly, XRD was used to confirm the different growth directions of GaN nanowire arrays grown epitaxially on (100)$LiAlO_2$ and (111)MgO substrates [9.143].

EDS has been used to determine the chemical compositions and stoichiometry of compound nanowires or impurity contents in nanowires. However, the results from EDS analysis should be interpreted carefully to avoid systematic errors.

9.2.2 Mechanical Properties

Thermal Stability

Due to the large surface-to-volume ratio in nanowires and other nanoparticles, the thermal stability of na-

nowires is anticipated to differ significantly from that of the bulk material. Theoretical studies of materials in confined geometries show that the melting point of the material is reduced in nanostructures, as is the latent heat of fusion, and that large hysteresis can be observed in melting-freezing cycles. These phenomena have been studied experimentally in three types of nanowire systems: porous matrices impregnated with a plurality of nanowires, individual nanowires sheathed by a thin coating, and individual nanowires.

The melting-freezing of matrix-supported nanowires can be studied by differential scanning calorimetry (DSC), since large volumes of samples can thus be produced. *Huber* et al. investigated the melting of indium in porous silica glasses with mean pore diameters ranging from 6 to 141 nm [9.154]. The melting point of the pore-confined indium shows a linear dependence on inverse pore diameter, with a maximum melting point depression of 50 K. A similar shift was observed in the freezing temperature of pore-confined indium. The melting profile of the pore-confined indium in these samples is broader in temperature than for bulk indium, as expected for the heterogeneity in the pore diameter and in the indium crystal size aspect ratio within the samples.

Sheathed nanowires provide an opportunity to study the melting and recrystallization of individual nanowires. The shell layer surrounding the nanowire provides confinement to keep the liquid phase within the inner cylindrical volume. However, the shell-nanowire surface interaction should be taken into account when analyzing the phase transition thermodynamics and kinetics. *Wu* and *Yang* produced germanium nanowires coated with a thin (1−5 nm) graphite sheath, by pyrolysis of organic molecules over VLS-grown nanowires, and followed the melting and recrystallization of the germanium by variable-temperature TEM imaging [9.155]. The melting of the nanowires was followed by the disappearance of the electronic diffraction pattern. It was found that the nanowires began melting from their ends, with the melting front advancing towards the center of the nanowire as the temperature was increased. During the cool-down part of the cycle, the recrystallization of the nanowire occurred instantaneously following significant supercooling. The authors report both the largest melting point suppression recorded thus far for germanium ($\approx 300\,^{\circ}\mathrm{C}$), and a large melting-recrystallization hysteresis of up to $\approx 300\,^{\circ}\mathrm{C}$. Similarly, carbon nanotubes have been filled with various low-temperature metals [9.156]. A nanothermometer has been demonstrated using a 10 nm liquid gallium-filled carbon nanotube, showing an expansion coefficient that is linear in temperature and identical to the bulk value [9.157].

A different behavior was observed in free-standing copper nanowires [9.158]. In this system, there is little interaction between the nanowire surface and the surroundings, and the nanowire is not confined in its diameter, as in the case of the sheathed nanowires. Thermal treatment of the free-standing nanowires leads to their fragmentation into a linear array of metal spheres. Thinner nanowires are more vulnerable than thicker nanowires to the thermal treatment, showing constrictions and segmentation at lower temperatures. Analysis of the temperature response of the nanowires indicates that the nanowire segmentation is a result of the Rayleigh instability, starting with oscillatory perturbations of the nanowire diameter, leading to long cylindrical segments that become more separated and more spherical at higher temperatures. These observations indicate that annealing and melting are dominated by the surface diffusion of atoms on the entire surface of the nanowire (versus tip-initiated melting).

9.2.3 Transport Properties

The study of electrical transport properties of nanowires is important for nanowire characterization, electronic device applications, and the investigation of unusual transport phenomena arising from one-dimensional quantum effects. Important factors that determine the transport properties of nanowires include the wire diameter, material composition, surface conditions, crystal quality, and the crystallographic orientation along the wire axis for materials with anisotropic material parameters, such as the effective mass tensor, the Fermi surface, or the carrier mobility.

Electronic transport phenomena in low-dimensional systems can be roughly divided into two categories: ballistic transport and diffusive transport. Ballistic transport phenomena occur when the electrons can travel across the nanowire without any scattering. In this case, the conduction is mainly determined by the contacts between the nanowire and the external circuit, and the conductance is quantized into an integral number of universal conductance units $G_0 = 2\mathrm{e}^2/h$ [9.160, 161]. Ballistic transport phenomena are usually observed in very short quantum wires, such as those produced using mechanically-controlled break junctions (MCBJs) [9.162, 163] where the electron mean free path is much longer than the wire length and the conduction is a pure quantum phenomenon. To observe ballistic transport, the thermal energy must also obey the relation $k_\mathrm{B}T \ll \varepsilon_j - \varepsilon_{j-1}$, where $\varepsilon_j - \varepsilon_{j-1}$ is the energy separation between subband levels j and $j-1$. On the other hand, for nanowires with lengths much larger than the carrier mean free path, the electrons (or holes) undergo numerous scattering events when they travel

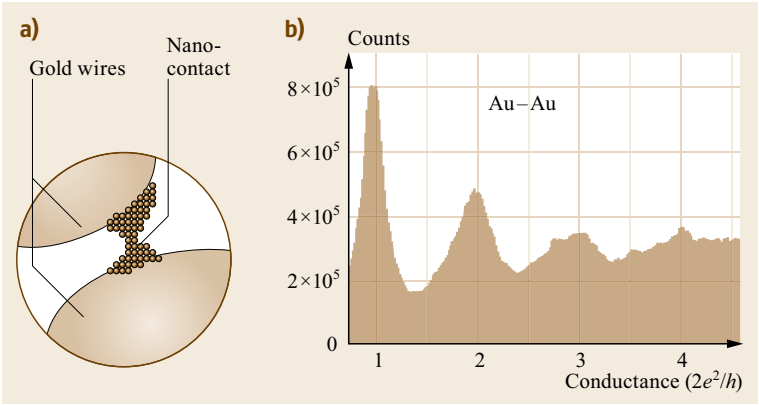

Fig. 9.23 **(a)** Schematic representation of the last stages of the contact breakage process (after [9.159]). **(b)** Histogram of conductance values built with 18 000 gold contact breakage experiments in air at room temperature, showing conductance peaks at integral values of G_0. In this experiment the gold electrodes approach and separate at 89 000 Å/s (after [9.159])

along the wire. In this case, the transport is in the diffusive regime, and the conduction is dominated by carrier scattering within the wires, due to phonons (lattice vibrations), boundary scattering, lattice and other structural defects, and impurity atoms.

Conductance Quantization in Metallic Nanowires

The ballistic transport of 1-D systems has been extensively studied since the discovery of quantized conductance in 1-D systems in 1988 [9.160, 161]. The phenomena of conductance quantization occurs when the diameter of the nanowire is comparable to the electron Fermi wavelength, which is on the order of 0.5 nm for most metals [9.164]. Most conductance quantization experiments up to the present were performed by bringing together and separating two metal electrodes. As the two metal electrodes are slowly separated, a nano-contact is formed before it breaks completely (Fig. 9.23a), and conductance in integral multiple values of G_0 is observed through these nano-contacts. Figure 9.23b shows the conductance histogram built with 18 000 contact breakage curves between two gold electrodes at room temperature [9.159], with the electrode separation up to ≈ 1.8 nm. The conductance quantization behavior is found to be independent of the contact material, and has been observed in various metals, such as Au [9.159], Ag, Na, Cu [9.165], and Hg [9.166]. For semimetals such as Bi, conductance quantization has also been observed for electrode separations as long as 100 nm at 4 K because of the long Fermi wavelength (≈ 26 nm) [9.164], indicating that the conductance quantization may be due to the existence of well-defined quantum states localized at a constriction instead of resulting from the atom rearrangement as the electrodes separate. Since conductance quantization is only observed in breaking contacts, or for very narrow and very short nanowires, most nanowires of practical interest (possessing lengths of several micrometers) lie in the diffusive transport regime, where the carrier scattering is significant and should be considered.

I–V Characterization of Semiconducting Nanowires

The electronic transport behavior of nanowires may be categorized based on the relative magnitudes of three length scales: carrier mean free path ℓ_W, the de Broglie wavelength of electrons λ_e, and the wire diameter d_W. For wire diameters much larger than the carrier mean free path ($d_W \gg \ell_W$), the nanowires exhibit transport properties similar to bulk materials, which are independent of the wire diameter, since the scattering due to the wire boundary is negligible compared to other scattering mechanisms. For wire diameters comparable to or smaller than the carrier mean free path ($d_W \approx \ell_W$ or $d_W < \ell_W$), but still much larger than the de Broglie wavelength of the electrons ($d_W \gg \lambda_e$), the transport in nanowires is in the classical finite size regime, where the band structure of the nanowire is still similar to that of bulk, while the scattering events at the wire boundary alter their transport behavior. For wire diameters comparable to the electronic wavelength $d_W \approx \lambda_e$, the electronic density of states is altered dramatically and discrete subbands are formed due to the quantum confinement effect at the wire boundary. In this regime, the transport properties are further influenced by the change in the band structure. Therefore, transport properties for nanowires in the classical finite size and quantum size regimes are highly diameter-dependent.

Researchers have investigated the transport properties of various semiconducting nanowires and have demonstrated their potential for diverse electronic devices, such as for p-n diodes [9.167, 168], field effect transistors [9.167], memory cells, and switches [9.169] (Sect. 9.3.1). So far, the nanowires studied in this context have usually been made from conventional semiconducting materials, such as group IV and III–V

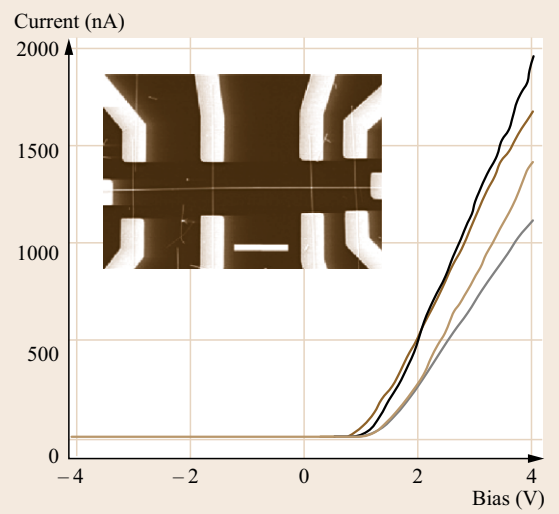

Fig. 9.24 *I–V* behavior for a 4(p) by 1(n) crossed p-Si/n-GaN junction array shown in the *inset*. The *four curves* represent the *I–V* response for each of the four junctions, showing similar current rectifying characteristics in each case. The length scale bar between the two middle junctions is 2 μm (after [9.167]). The p-Si and n-GaN nanowires are 10−25 and 10−30 nm in diameter respectively

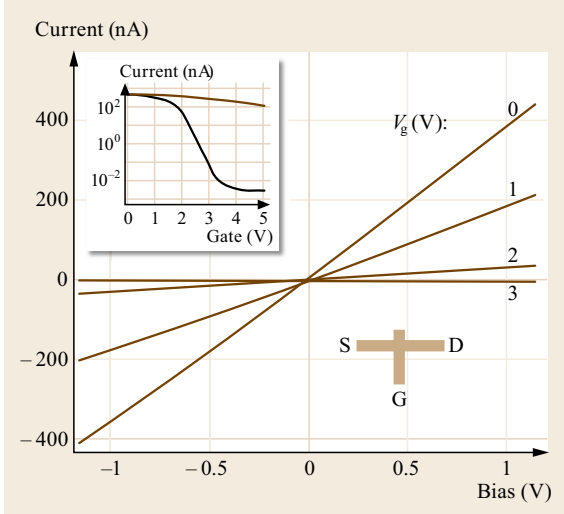

Fig. 9.25 Gate-dependent *I–V* characteristics of a crossed nanowire field-effect transistor (FET). The n-GaN nanowire is used as the nanogate, with the gate voltage indicated (0, 1, 2, and 3 V). The *inset* shows the current versus V_{gate} for a nanowire gate (*lower curve*) and for a global back-gate (*top curve*) when the bias voltage is set to 1 V (after [9.167])

compound semiconductors, via the VLS growth method (Sect. 9.1.2), and their nanowire properties have been compared to their well-established bulk properties. Interestingly, the physical principles for describing bulk semiconductor devices also hold for devices based on these semiconducting nanowires with wire diameters of tens of nanometers. For example, Fig. 9.24 shows the current-voltage (*I–V*) behavior of a four-by-one crossed p-Si/n-GaN junction array at room temperature [9.167]. The long horizontal wire in the figure is a p-Si nanowire (10−25 nm in diameter) and the four short vertical wires are n-GaN nanowires (10−30 nm in diameter). Each of the four nanoscale cross-points independently forms a p-n junction with current rectification behavior, as shown by the *I–V* curves in Fig. 9.24. The junction behavior (for example, the turn-on voltage) can be controlled by varying the oxide coating on these nanowires [9.167].

Huang et al. have demonstrated nanowire junction diodes with a high turn-on voltage (≈ 5 V) by increasing the oxide thickness at the junctions. The high turn-on voltage enables the use of the junction in a nanoscale field-effect transistor (FET), as shown in Fig. 9.25 [9.167] where *I–V* data for a p-Si nanowire are presented, for which the n-GaN nanowire with a thick oxide coating is used as a nanogate. By varying the nanogate voltage, the conductance of the p-Si nanowire can be changed by more than a factor of 10^5 (lower curve in the inset), whereas the conductance changes by only a factor of ten when a global back-gate is used (top curve in the inset of Fig. 9.25). This behavior may be due to the thin gate dielectric between the crossed nanowires and the better control of the local carrier density through a nanogate. Based on the gate-dependent *I–V* data from these p-Si nanowires, it is found that the mobility of the holes in the p-Si nanowires may be higher than that for bulk p-Si, although further investigation is required for complete understanding.

Because of the enhanced surface-to-volume ratios of nanowires, their transport behavior may be modified by changing their surface conditions. For example, researchers have found that by coating n-InP nanowires with a layer of redox molecules, such as cobalt phthalocyanine, the conductance of the InP nanowires may change by orders of magnitude upon altering the charge state of the redox molecules to provide bistable nanoscale switches [9.169]. The resistance (or conductance) of some nanowires (such as Pd nanowires) is also very sensitive to the presence of certain gases (e.g., H_2) [9.170, 171], and this property may be utilized for sensor applications to provide improved sensitivity compared to conventional sensors based on bulk material (Sect. 9.3.4).

Although it remains unclear how the size effect may influence the transport properties and device performance of semiconducting nanowires, many of the

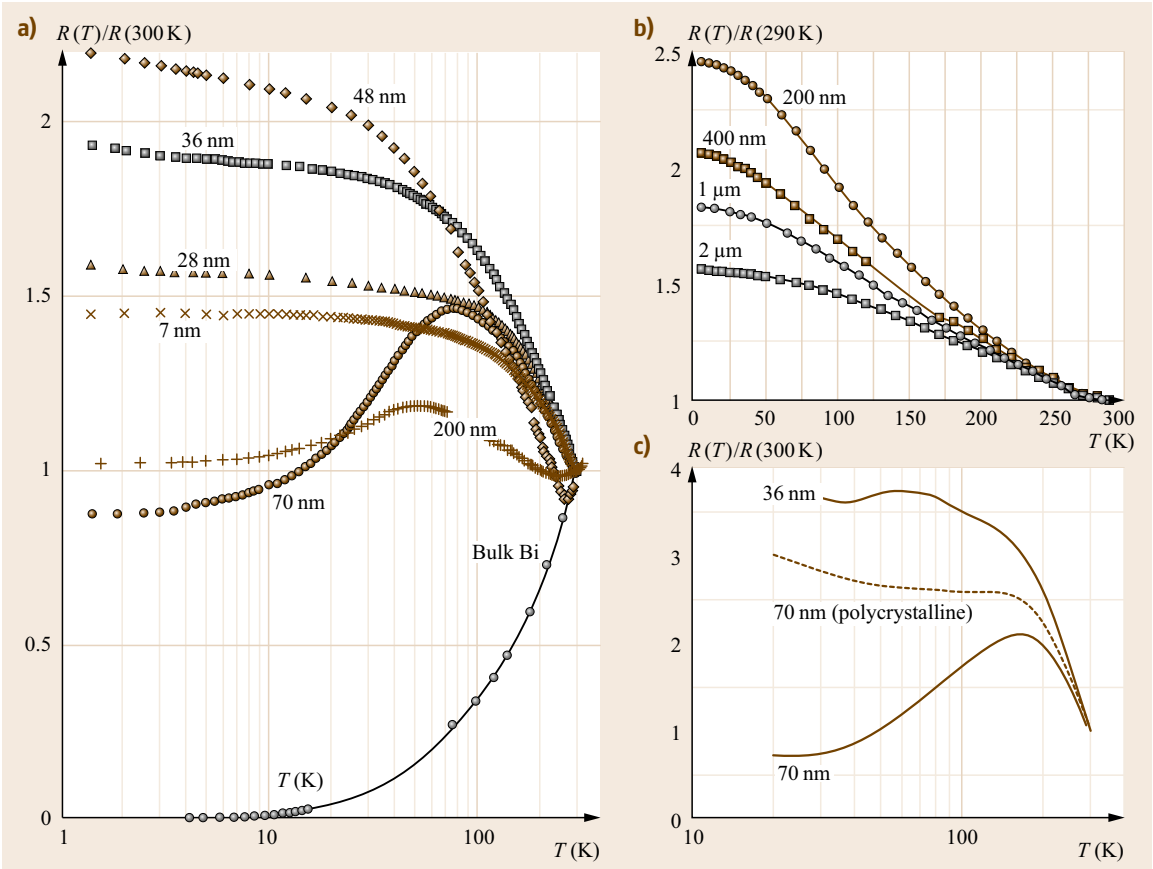

Fig. 9.26 **(a)** Measured temperature dependence of the resistance $R(T)$ normalized to the room temperature (300 K) resistance for bismuth nanowire arrays of various wire diameters d_W (after [9.17]). **(b)** $R(T)/R(290\,K)$ for bismuth wires of larger d_W and lower mobility (after [9.19]). **(c)** Calculated $R(T)/R(300\,K)$ of 36 and 70 nm bismuth nanowires. The *dashed curve* refers to a 70 nm polycrystalline wire with increased boundary scattering (after [9.93])

larger-diameter semiconducting nanowires are expected to be described by classical physics, since their quantization energies $\hbar^2/(2m_e d_W^2)$ are usually smaller than the thermal energy $k_B T$. By comparing the quantization energy with the thermal energy, the critical wire diameter below which quantum confinement effects become significant is estimated to be 1 nm for Si nanowires at room temperature, which is much smaller than the sizes of many of the semiconducting nanowires that have been investigated so far. By using material systems with much smaller effective carrier masses m_e (such as bismuth), the critical diameter for which such quantum effects can be observed increases, thereby facilitating the study of quantum confinement effects. It is for this reason that the bismuth nanowire system has been studied so extensively. Furthermore, since the crystal structure and lattice constants of bismuth nanowires are the same as for 3-D crystalline bismuth, it is possible to carry out detailed model calculations to guide and to interpret transport and optical experiments on bismuth nanowires. For these reasons, bismuth can be considered a model system for studying 1-D effects in nanowires.

Temperature-Dependent Resistance Measurements

Although nanowires with electronic properties similar to their bulk counterparts are promising for constructing nanodevices based on well-established knowledge of their bulk counterparts, it is expected that quantum size effects in nanowires will likely be utilized to generate new phenomena absent in bulk materials, and thus provide enhanced performance and novel functionality for certain applications. In this context, the transport properties of bismuth (Bi) nanowires have been extensively studied, both theoretically [9.172] and experimentally [9.17, 19, 93, 173–175] because of their promise for enhanced thermoelectric performance.

Transport studies of ferromagnetic nanowire arrays, such as Ni or Fe, have also received much attention because of their potential for high-density magnetic storage applications [9.176].

As mentioned in the previous section, the very small electron effective mass components and the long carrier mean free paths in Bi facilitate the study of quantum size effects in the transport properties of nanowires. Quantum size effects are expected to become significant in bismuth nanowires with diameters smaller than 50 nm [9.172], and the fabrication of crystalline nanowires with this diameter range is relatively easy.

Figure 9.26a shows the T dependence of the resistance $R(T)$ for Bi nanowires ($7\,\text{nm} \leq d_W < 200\,\text{nm}$) synthesized by vapor deposition and pressure injection [9.17], illustrating quantum effects in their temperature-dependent resistance. In Fig. 9.26a, the $R(T)$ behavior of Bi nanowires is dramatically different from that of bulk Bi, and is highly sensitive to the wire diameter. Interestingly, the $R(T)$ curves in Fig. 9.26a show a non-monotonic trend for large-diameter (70 and 200 nm) nanowires, although $R(T)$ becomes monotonic with T for small-diameter ($\leq 48\,\text{nm}$) nanowires. This dramatic change in the behavior of $R(T)$ as a function of d_W is attributed to a unique semimetal-semiconductor transition phenomena in Bi [9.93], induced by quantum size effects. Bi is a semimetal in bulk form, in which the T-point valence band overlaps with the L-point conduction band by 38 meV at 77 K. As the wire diameter decreases, the lowest conduction subband increases in energy and the highest valence subband decreases in energy. Model calculations predict that the band overlap should vanish in Bi nanowires (with their wire axes along the trigonal crystallographic direction) at a wire diameter $\approx 50\,\text{nm}$ [9.172].

The resistance of Bi nanowires is determined by two competing factors: the carrier density that increases with T, and the carrier mobility that decreases with T. The non-monotonic $R(T)$ for large-diameter Bi nanowires is due to a smaller carrier concentration variation at low temperature ($\leq 100\,\text{K}$) in semimetals, so that the electrical resistance is dominated by the mobility factor in this temperature range. Based on the semiclassical transport model and the established band structure of Bi nanowires, the calculated $R(T)/R(300\,\text{K})$ for 36 and 70 nm Bi nanowires is shown by the solid curves in Fig. 9.26c to illustrate different $R(T)$ trends for semiconducting and semimetallic nanowires respectively [9.93]. The curves in Fig. 9.26c exhibit trends consistent with experimental results. The condition for the semimetal-semiconductor transition in Bi nanowires can be experimentally determined, as shown by the measured resistance ratio $R(10\,\text{K})/R(100\,\text{K})$ of Bi nanowires as a function of wire diameter [9.177] in Fig. 9.27. The maximum in the resistance ratio $R(10\,\text{K})/R(100\,\text{K})$ at $d_W \approx 48\,\text{nm}$ indicates the wire diameter for the transition of Bi nanowires from a semimetallic phase to a semiconducting phase. The semimetal-semiconductor transition and the semiconducting phase in Bi nanowires are examples of new transport phenomena resulting from low dimensionality that are absent in the bulk 3-D phase. These phenomena further increase the possible benefits of exploiting properties of nanowires for desired applications.

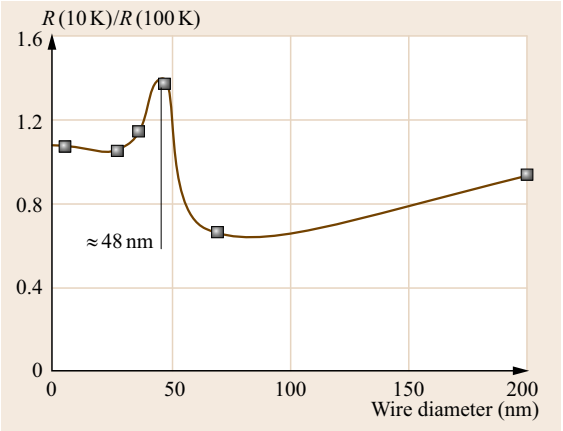

Fig. 9.27 Measured resistance ratio $R(10\,\text{K})/R(100\,\text{K})$ of a Bi nanowire array as a function of diameter. The *peak* indicates the transition from a semimetallic phase to a semiconducting phase as the wire diameter decreases (after [9.178])

It should be noted that good crystal quality is essential for observing the quantum size effect in nanowires, as shown by the $R(T)$ plots in Fig. 9.26a. Fig. 9.26b shows the normalized $R(T)$ measurements of Bi nanowires with larger diameters (200 nm–2 μm) prepared by electrochemical deposition [9.19]. These nanowires possess monotonic $R(T)$ behaviors, quite different from those of the corresponding nanowire diameters shown in Fig. 9.26a. The absence of the resistance maximum in Fig. 9.26b is due to the lower crystalline quality for nanowires prepared by electrochemical deposition, which tends to produce polycrystalline nanowires with a much lower carrier mobility. This monotonic $R(T)$ curve for semimetallic Bi nanowires with a higher defect level is also confirmed by theoretical calculations, as shown by the dashed curve in Fig. 9.26c for 70 nm wires with increased grain boundary scattering [9.179].

The theoretical model developed for Bi nanowires not only provides good agreement with experimental results, but it also plays an essential role in understanding the influence of the quantum size effect, the boundary scattering, and the crystal quality on their electrical

properties. While the electronic density of states may be significantly altered due to quantum confinement effects, various scattering mechanisms related to the transport properties of nanowires can be accounted for by Matthiessen's rule. Furthermore, the transport model has also been generalized to predict the transport properties of Te-doped Bi nanowires [9.93], Sb nanowires [9.180], and BiSb alloy nanowires [9.181], and good agreement between experiment and theory has also been obtained for these cases.

For nanowires with diameters comparable to the phase-breaking length, their transport properties may be further influenced by localization effects. It has been predicted that in disordered systems, the extended electronic wavefunctions become localized near defect sites, resulting in the trapping of carriers and giving rise to different transport behavior. Localization effects are also expected to be more pronounced as the dimensionality and sample size are reduced. Localization effects on the transport properties of nanowire systems have been studied on Bi nanowires [9.182] and Zn nanowires [9.63]. Figure 9.28 shows the measured $R(T)/R(300\,\mathrm{K})$ of Zn nanowires fabricated by vapor deposition in porous silica or alumina [9.63]. While 15 nm Zn nanowires exhibit an $R(T)$ behavior with a T^1 dependence as expected for a metallic wire, the $R(T)$ of 4 nm Zn nanowires exhibits a temperature dependence of $T^{-1/2}$ at low temperatures, consistent with 1-D localization theory. Thus, due to this localization effect, the use of nanowires with very small diameters for transport applications may be limited.

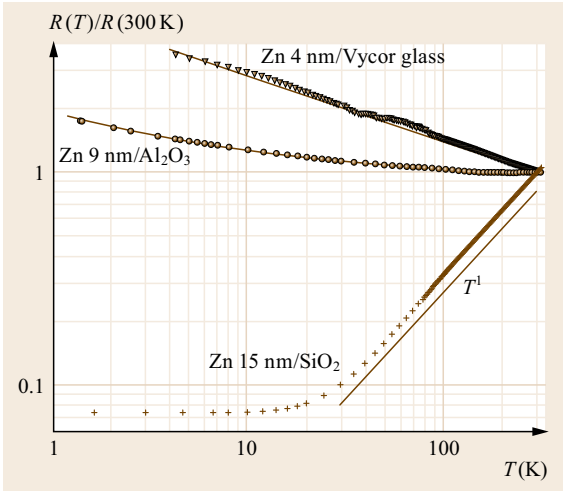

Fig. 9.28 Temperature dependence of the resistance of Zn nanowires synthesized by vapor deposition in various porous templates (after [9.63]). The data are given as *points*, the *full lines* are fits to a T^1 law for 15 nm diameter Zn nanowires in an SiO_2 template, denoted by Zn/SiO_2. Fits to a combined T^1 and $T^{-1/2}$ law were made for the smaller nanowire diameter composite samples denoted by Zn (9 nm)/Al_2O_3 and Zn 4 nm/Vycor glass

Magnetoresistance

Magnetoresistance (MR) measurements for characterizing nanowires yield a great deal of information about the effects of wire boundary, doping and annealing on electron scattering, and about localization effects in nanowires [9.175]. For example, at low fields the MR data show a quadratic dependence on the B field from which carrier mobility estimates can be made (Fig. 9.29 at low B field).

Figure 9.29 shows the longitudinal magnetoresistance ($\boldsymbol{B}$ parallel to the wire axis) for 65 and 109 nm Bi nanowire samples (before thermal annealing) at 2 K. The MR maxima in Fig. 9.29a are due to the classical size effect, where the wire boundary scattering is reduced as the cyclotron radius becomes smaller than the wire radius in the high field limit, resulting in a decrease in resistivity. This behavior is typical for the longitudinal MR of Bi nanowires in the diameter range of 45–200 nm [9.17, 174, 175, 183], and the peak position B_m moves to lower B field values as the wire diameter increases, as shown in Fig. 9.29c [9.183], where B_m varies linearly with $1/d_\mathrm{W}$. The condition for the occurrence of B_m is approximately given by $B_\mathrm{m} \approx 2c\hbar k_\mathrm{F}/(ed_\mathrm{W})$, where k_F is the wave vector at the Fermi energy. The peak position B_m is found to increase linearly with increasing temperature in the range of 2–100 K, as shown in Fig. 9.29b [9.183]. As T is increased, phonon scattering becomes increasingly important, and therefore a higher magnetic field is required to reduce the resistivity associated with boundary scattering sufficiently to change the sign of the MR. Likewise, increasing the grain boundary scattering is also expected to increase the value of B_m at a given T and wire diameter.

The presence of the peak in the longitudinal MR of nanowires requires a high crystal quality with long carrier mean free paths along the nanowire axis, so that most scattering events occur at the wire boundary instead of at a grain boundary, at impurity sites, or at defect sites within the nanowire. *Liu* et al. have investigated the MR of 400 nm Bi nanowires synthesized by electrochemical deposition [9.84], and no peak in the longitudinal MR is observed. The absence of a magnetoresistance peak may be attributed to a higher defect level in the nanowires produced electrochemically and to a large wire diameter, much longer than the carrier mean free path. The negative MR observed for the Bi nanowire arrays above B_m (Fig. 9.29) shows that wire boundary scattering is a dominant scattering process for the longitudinal magnetoresistance, thereby estab-

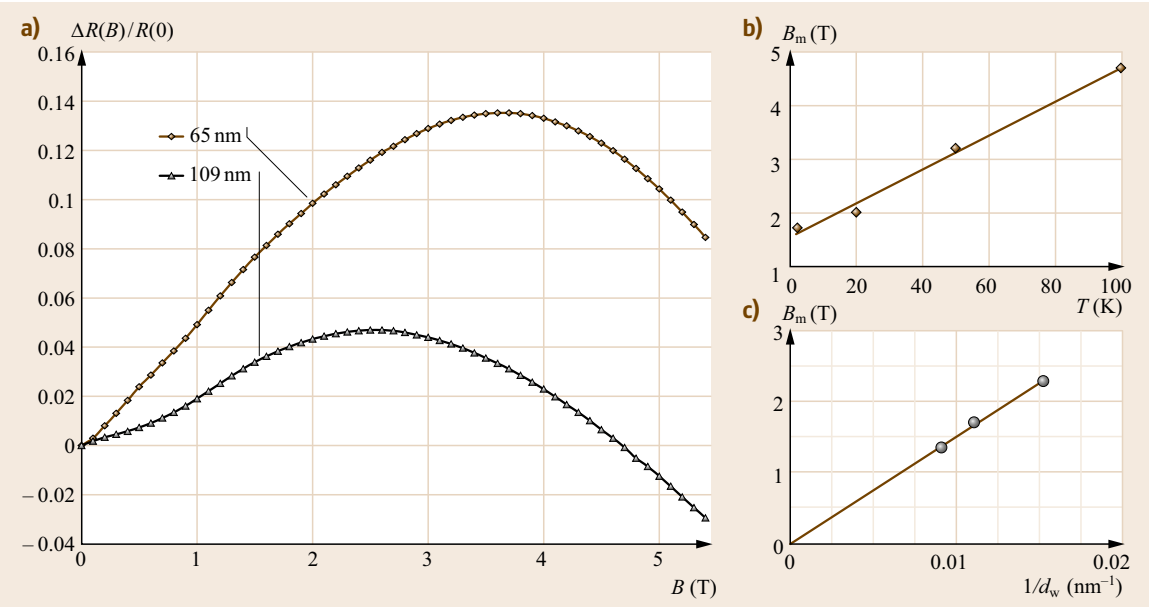

Fig. 9.29 **(a)** Longitudinal magnetoresistance, $\Delta R(B)/R(0)$, at 2 K as a function of B for Bi nanowire arrays with diameters of 65 and 109 nm before thermal annealing. **(b)** The peak position B_m as a function of temperature for the 109 nm diameter Bi nanowire array after thermal annealing. **(c)** The peak position B_m of the longitudinal MR (after thermal annealing) at 2 K as a function of $1/d_W$, the reciprocal of the nanowire diameter (after [9.183])

lishing that the mean free path is larger than the wire diameter.

In addition to the longitudinal magnetoresistance measurements, transverse magnetoresistance measurements (***B*** perpendicular to the wire axis) have also been performed on Bi nanowire array samples [9.17, 175, 183], where a monotonically increasing B^2 dependence over the entire range $0\,\mathrm{T} \leq B \leq 5.5\,\mathrm{T}$ is found for all Bi nanowires studied. This is expected, since the wire boundary scattering cannot be reduced by a magnetic field perpendicular to the wire axis. The transverse magnetoresistance is also found to be always larger than the longitudinal magnetoresistance in nanowire arrays.

The Shubnikov–de Haas (SdH) quantum oscillatory effect, which results from the passage of the quantized Landau levels through the Fermi energy as the field strength varies, should, in principle, provide the most direct measurement of the Fermi energy and carrier density. For example, *Heremans* and *Thrush* have demonstrated that SdH oscillations can be observed in Bi nanowire samples with diameters down to 200 nm [9.184], and they have demonstrated that Te doping can be used to raise the Fermi energy in Bi nanowires. Such information on the Fermi energy is important because, for certain applications based on nanowires, it is necessary to place the Fermi energy near a subband edge where the density of states has a sharp feature. However, due to the unusual 1-D geometry of nanowires, other characterization techniques that are commonly used in bulk materials to determine the Fermi energy and the carrier concentration (such as Hall effect measurement) cannot be applied to nanowire systems.

Thermal Conductivity of Nanowires

The thermal conductivity in nanowires can be significantly reduced as the dimensions of the nanowire become comparable to the phonon mean free path and the phonon wavelength [9.185]. The confinement in the nanowire may modify the phononphonon density of states, while defects in the nanowire enhance scattering. The most dominant suppression of thermal conductivity is achieved when multiple mechanisms operate to impede phonon transport at various length scales: atomic point-defects scatter high-frequency phonons, and interfaces and grain boundaries scatter primarily low-to-mid frequency phonons. Silicon nanowires with smooth and rough surfaces [9.186–188], segmented Si/SiGe nanowires [9.189], and indium gallium zinc oxide nanowires [9.190] have been selected as testbeds for fundamental studies. The enhancement of a new mechanism of phonon scattering in nanowires is evident by the lower thermal conductivity and by the change in its temperature dependence [9.185].

Measurements of the thermal conductivity of nanowires have been carried out on nanowire arrays embed-

ded in a matrix and individual free-standing nanowires. The former provides data of relevance to device performance, while only the latter can provide reliable data that are not distorted by thermal transport via the matrix or substrate and by sample polydispersity. Single-nanowire thermal measurements are very challenging and are now possible thanks to technological developments in the micro- and nanofabrication of miniature thermal sensors [9.191], and the use of nanometer-size thermal scanning probes [9.153, 192, 193]. In a typical fabricated device, shown in Fig. 9.30, a nanowire is suspended across a gap between two SiN_x membranes supported by long beams. On the membranes, metal lines form heating elements, resistive temperature sensors, and electrodes. Using a heat flow model, the thermal conductivity $\kappa(T)$ of the individual suspended nanowires can be extracted from the sensor data [9.194].

The experiments show that the thermal conductivity of small-diameter homogeneous nanowires may be more than one order of magnitude smaller than in the bulk, mainly due to the effect of strong phonon boundary scattering [9.195]. Phonon confinement effects may eventually become important in nanowires with even smaller diameters. The most extensive experimental thermal conductivity measurements have been done on Si nanowires [9.186], where $\kappa(T)$ measurements have been made on nanowires in the diameter range of 22−115 nm. As d_W decreases a large decrease is observed in the peak of $\kappa(T)$, associated with Umklapp processes, indicating a growing importance of boundary scattering and a corresponding decreasing importance of phonon-phonon scattering (Fig. 9.31). At the smallest wire diameter of 22 nm, a linear $\kappa(T)$ dependence is found experimentally, consistent with a linear T dependence of the specific heat for a 1-D system, and a temperature-independent mean free path and sound velocity. Introduction of scattering elements through alloying and composition modulation, such as in Si/SiGe superlattice nanowires, pushed the thermal conductivity values further down [9.189]. Remarkably, surface roughness, observed in some Si nanowires fabricated by the MACE method (Sect. 9.1.3), also reduces $\kappa(T)$ by an order of magnitude, such that 50 nm diameter rough Si nanowires have thermal conductivity values lower than 2 $Wm^{-1}K^{-1}$ at room temperature [9.188].

Model calculations for $\kappa(T)$ based on a radiative heat transfer model have been carried out for Si nanowires [9.196–198]. These results show that the predicted $\kappa(T)$ behavior for Si nanowires is similar to that observed experimentally in the range of 37 nm $\leq d_W \leq$ 115 nm regarding both the functional form of $\kappa(T)$ and the magnitude of the relative decrease in the maximum thermal conductivity as a function of

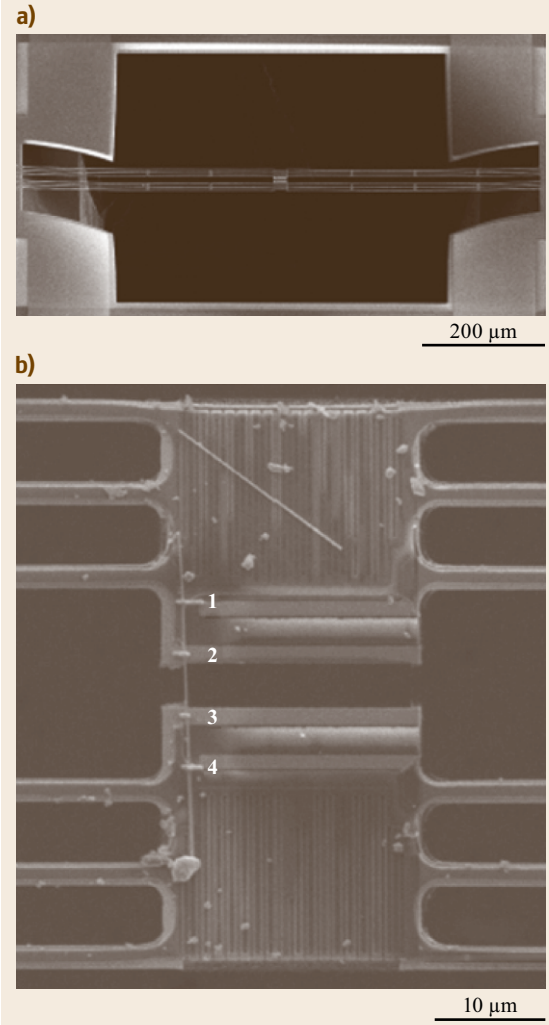

Fig. 9.30a,b Microfabricated device for the measurement of the thermal conductivity and thermoelectric properties of individual nanowires. **(a)** Low magnification view of the full length of the microscale device. **(b)** High magnification view of the probed nanowire and metalization lines on the membranes. IOP Publishing. Reproduced with permission. All right reserved (after [9.191])

d_W. However, the model calculations often overestimate κ_{max}, with agreement improved by using the full phonon dispersion relations. Furthermore, the model calculations (Fig. 9.31) do not reproduce the experimentally observed linear T dependence for the 22 nm nanowires, but rather predict a 3-D behavior for both the density of states and the specific heat in 22 nm nanowires [9.196, 199]. *Kazan* et al. resolved the discrepancies by considering also optical phonon decay and an angle-dependent specularity function for the boundary scattering, and

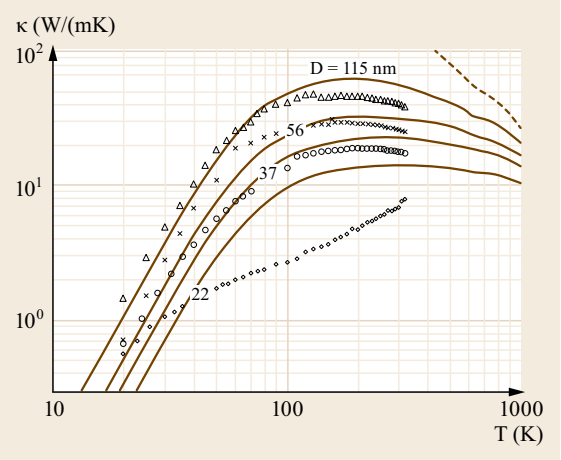

Fig. 9.31 Predicted thermal conductivities of Si nanowires of various diameters (*solid lines*) and the corresponding experimental data (symbols, from [9.186]) (after [9.196])

they were able to model both the diameter and surface roughness effects [9.200].

Thermal conductance measurements on GaAs nanowires below 6 K show a power law dependence, but the T dependence becomes somewhat less pronounced below ≈ 2.5 K [9.192]. This deviation from the power law temperature dependence led to a more detailed study of the quantum limit for the thermal conductance. To carry out more detailed experiments, a mesoscopic phonon resonator and waveguide device were constructed that included four ≈ 200 nm wide and 60 nm thick silicon nitride nanowire-like nano-constrictions (Fig. 9.32a), and this was used to establish the quantized thermal conductance limit of $g_0 = \pi^2 k_B^2 T/(3h)$ (Fig. 9.32b) for ballistic phonon transport [9.201, 202].

For temperatures above 0.8 K, the thermal conductance in Fig. 9.32b follows a T^3 law, but as T is further reduced, a transition to a linear T dependence is observed, consistent with a phonon mean free path of $\approx 1\,\mu$m, and a thermal conductance value approaching $16g_0$, corresponding to four massless phonon modes per channel and four channels in their phonon waveguide structure (Fig. 9.32a). Ballistic phonon transport occurs when the thermal phonon wavelength (380 nm for the experimental structure) is somewhat greater than the width of the phonon waveguide at the waveguide constriction.

Thermoelectric Properties

Nanowires are predicted to hold great promise for thermoelectric applications [9.172, 203], due to their unique band structure compared to their bulk counterparts and the expected reduction in thermal conductivity associated with enhanced boundary scattering (see Sect. 9.2.3, *Thermal Conductivity of Nanowires* above). Due to the sharp density of states function at the 1-D subband edges (where the van Hove singularities occur), nanowires are expected to exhibit enhanced Seebeck coefficients compared to their bulk counterparts. Since the Seebeck coefficient measurement is intrinsically independent of the number of nanowires contributing to the signal, the measurements on nanowire arrays of uniform wire diameter are, in principle, as accurate as single-wire measurements. Individual nanowire measurements, on the other hand, allow for the simultaneous determination of the Seebeck coefficient S, the thermal conductivity κ, and the electrical conductivity σ (and thus, the power factor $S^2\sigma$ and the figure-of-merit $ZT = S^2\sigma T\kappa^{-1}$), as well as electrostatic gating of semiconductor nanowires for detailed stud-

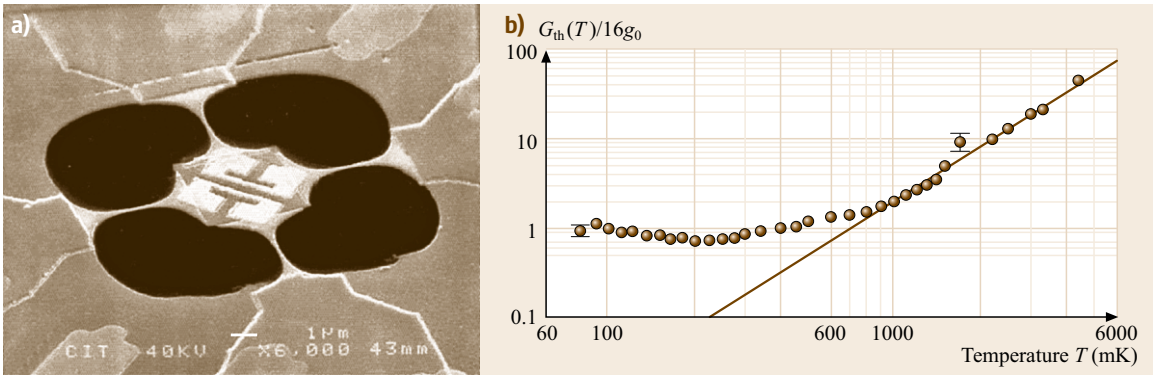

Fig. 9.32 **(a)** Suspended mesoscopic phonon device used to measure ballistic phonon transport. The device consists of a $4\times4\,\mu m^2$ *phonon cavity* (*center*) connected to four Si_3N_4 beams, 60 nm thick and less than 200 nm wide at the narrowest point. The two bright C-shaped objects on the phonon cavity are thin-film heating and sensing Cr/Au resistors, whereas the *dark regions* are empty space. **(b)** Log–log plot of the temperature dependence of the thermal conductance G_0 of the structure in **(a)** normalized to $16g_0$ (see text) (after [9.201])

ies of carrier concentration effects on thermoelectric properties.

Many nanowire systems have demonstrated enhanced Seebeck coefficient values as the diameter of the nanowire is reduced. Measured Seebeck coefficients $S(T)$ may also display a temperature dependence different than the bulk, indicative of carrier localization, enhanced scattering, or quantum confinement effects. In the well-known $Bi_{1-x}Sb_x$ thermoelectric material systems, $S(T)$ values are enhanced in arrays of nanowires with diameters of 40 and 65 nm (but not 200 nm), and by alloying with isoelectronic Sb [9.179]. Thermopower enhancement is attributed to the semimetal-semiconductor transition induced by quantum confinement and to Sb alloying effects in $Bi_{1-x}Sb_x$ nanowires [9.204]. *Heremans* et al. have observed a substantial increase in the thermopower of Bi in tiny nanowires in Bi(15 nm)/silica and Bi(9 nm)/alumina disordered nanocomposites [9.63]. The enhancement is due to the sharp density of states near the Fermi energy in a 1-D system. Measurements on individual or a small number of Si nanowires also showed dramatic enhancement of the Seebeck coefficient near and below room temperature, showing that non-traditional thermoelectric materials can become technologically relevant in nanowire form [9.187, 188]. This is particularly important in light of the poor mechanical properties, low abundance, and toxicity of some of the materials traditionally used for thermoelectrics. Since the Seebeck coefficient is a function of the carrier density, modulation of $S(T, V_G)$ is observed in individual electrostatically-gated nanowires (Sb_2Te_3 [9.205]; PbSe [9.206]; InAs [9.207, 208]), offering an additional strategy for tuning the thermoelectric properties. At cryogenic temperatures, the $S(V_G)$ function shows distinct peaks. The interpretation of these peaks is still under debate; the features may originate from the quantization in the band structure (subband formation) or from nanowire nonuniformities.

For applications in cooling and power generation, enhancing only the thermopower is not sufficient. In fact, in all the nanowire examples quoted above, the enhanced thermopower is accompanied by a significant reduction of the electrical conductivity, detrimental to the power factor $S^2\sigma$. Theoretical work demonstrates that quantum confinement in nanowires effectively reduces that density-of-states for electrons and holes in two-band semiconductors. As a result, as the nanowire diameter decreases, a decrease in the power factor is expected (Fig. 9.33) [9.209, 210]. This trend is reversed in small-diameter nanowires where electrons in the single lowest subband dominate transport ($d < 37$ nm for InSb, see Fig. 9.33). At this strongly confined regime, the power factor goes as d^{-2}; however, electron scattering and localization effects put a cap on the benefits of size reduction. The notable breakthroughs in low-dimensional systems for thermoelectric applications are related to the high figure-of-merit values that were achieved by drastically reducing the thermal conductivity while maintaining the power factor only slightly below bulk values. In smooth- and rough-edge silicon nanowires, reduction of the thermal conductivity by two orders of magnitude led to ZT values of up to 0.6 at 300 K (compare to 0.01 for bulk silicon) [9.187, 188]. Further improvements will likely involve materials with more complex band structures [9.204, 211] and more complex geometries [9.212].

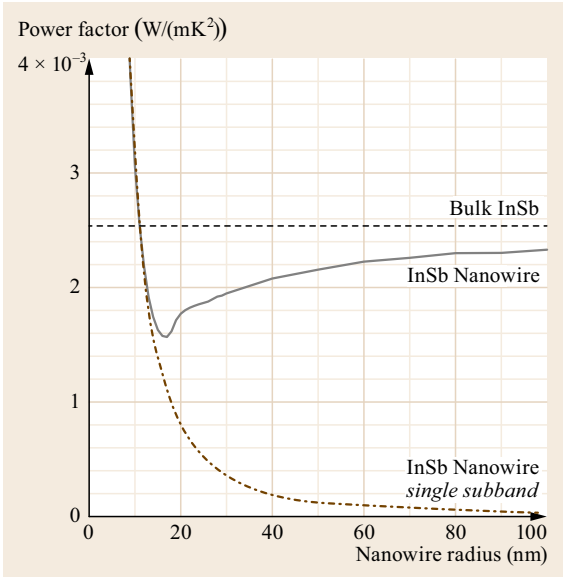

Fig. 9.33 Calculated thermoelectric power factor for n-type InSb nanowires (*solid line*). The power factor surpasses the bulk value (*dashed line*) only for very narrow nanowires, where electrons in one subband dominate transport. The *dash-dotted* line illustrates the size dependence of the power factor in a model considering just one subband (adapted from [9.209])

In 3-D systems, the electronic contribution to κ is proportional to σ in accordance with the Wiedemann–Franz law, and normally materials with high S have a low σ. Hence an increase in the electrical conductivity (for example by electron donor doping) results in an adverse variation in both the Seebeck coefficient (decreasing) and the thermal conductivity (increasing). These two trade-offs set the upper limit for increasing ZT in bulk materials, with the maximum ZT remaining ≈ 1 at room temperature for the 1960–1995 time frame.

The high electronic density of states in quantum-confined structures is proposed as a promising possibil-

ity to bypass the Seebeck/electrical conductivity tradeoff and to control each thermoelectric-related variable independently, thereby allowing for increased electrical conductivity, relatively low thermal conductivity, and a large Seebeck coefficient simultaneously [9.213]. The quantum size effect in nanowires can be combined with other parameters to tailor the band structure and electronic transport behavior (for instance, Sb alloying in Bi) to further optimize ZT. For example, Fig. 9.34 shows the predicted ZT for p-type $Bi_{1-x}Sb_x$ alloy nanowires as a function of wire diameter and Sb content x [9.204]. The occurrence of a local ZT maximum in the vicinity of $x \approx 0.13$ and $d_W \approx 45$ nm is due to the coalescence of the energies of ten valence bandextrema in the nanowire and the resulting unusually high density of states for holes, which is a phenomenon absent in bulk $Bi_{1-x}Sb_x$ alloys. For nanowires with very small diameters, it is speculated that localization effects will eventually limit the enhancement of ZT. However, in bismuth nanowires, localization effects are not significant for wires with diameters larger than 9 nm [9.63]. In addition to 1-D nanowires, ZT values as high as ≈ 2 have also been experimentally demonstrated in macroscopic samples containing PbSe quantum dots (0-D) [9.214] and stacked two-dimensional (2-D) films [9.195].

Quantum Wire Superlattices

The studies on superlattice nanowires, which possess a periodic modulation in their material composition along the wire axis, have attracted much attention recently because of their promise in various applications, such as thermoelectrics [9.107, 215], nanobarcodes (Sect. 9.3.2) [9.216], nanolasers (Sect. 9.3.2) [9.111], one-dimensional waveguides, and resonant tunneling diodes [9.113, 217]. Figure 9.35a shows a schematic structure of a superlattice nanowire consisting of interlaced quantum dots of two different materials, as denoted by A and B. Various techniques have been developed to synthesize superlattice nanowire structures with different interface conditions, as mentioned in Sects. 9.1.1 and 9.1.2.

In this superlattice nanowire structure, the electronic transport along the wire axis is made possible by the tunneling between adjacent quantum dots, while the uniqueness of each quantum dot and its 0-D characteristic behavior is maintained by the energy difference of the conduction or valence bands between quantum dots of different materials (Fig. 9.35b), which provides some amount of quantum confinement. *Björk* et al. have observed interesting nonlinear I–V characteristics with a negative differential resistance in one-dimensional heterogeneous structures made of InAs and InP, where InP serves as the potential barrier [9.113, 217]. The nonlinear I–V behavior is associated with the double barrier resonant tunneling process in one-dimensional structures, demonstrating that transport phenomena occur in superlattice nanowires via tunneling, and the possibility of controlling the electronic band structure of the superlattice nanowires by carefully selecting the constituent materials. These structures are especially attractive for thermoelectric applications, because the interfaces between the nanodots can reduce the lattice thermal conductivity by blocking the phonon conduction along the wire axis, while electrical conduction may be sustained and even benefit from the unusual electronic band structures due to the periodic potential perturbation.

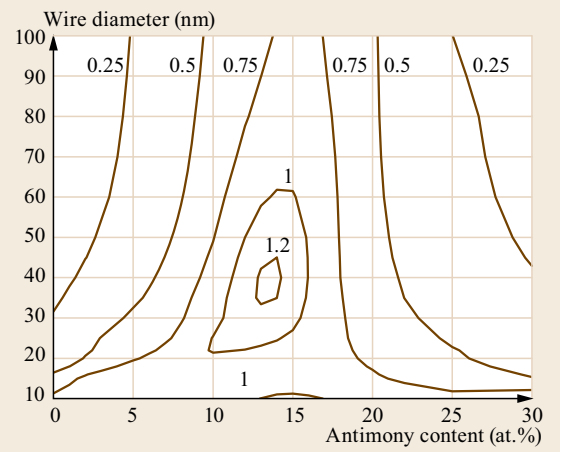

Fig. 9.34 Contour plot of optimal ZT values calculated for p-type $Bi_{1-x}Sb_x$ nanowires versus wire diameter and antimony concentration calculated at 77 K (after [9.204])

9.2.4 Optical Properties

Optical methods provide a convenient tool for measuring the electronic structures of nanowires, since optical

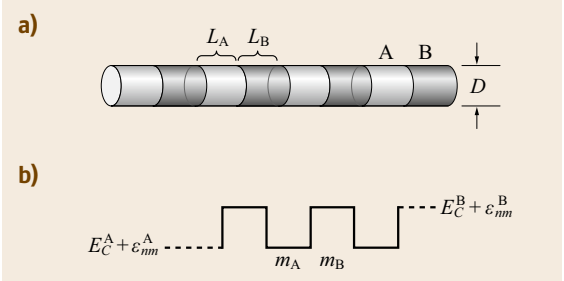

Fig. 9.35 (a) Schematic diagram of superlattice (segmented) nanowires consisting of interlaced nanodots A and B of the indicated length and wire diameter. **(b)** Schematic potential profile of the subbands in the superlattice nanowire (after [9.215])

measurements require minimal sample preparation (for example, contacts are not required) and are sensitive to quantum effects. A variety of optical techniques have shown that the properties of nanowires are different from those of their bulk counterparts. For example, optical spectra of 1-D systems often show intense features at specific energies near singularities in the joint density of states that are formed under strong quantum confinement conditions.

Although optical methods are an extremely important tool for characterizing nanowires, the interpretation of these measurements for nanowires is not always straightforward. The wavelength of light used to probe the sample is usually smaller than the wire length, but larger than the wire diameter. Hence, the probe light used in an optical measurement cannot be focused solely onto the wire, and the wire and the substrate on which the wire rests (or host material, if the wires are embedded in a template) are probed simultaneously.

In this section we discuss the determination of the dielectric function for nanowires from optical measurements. We then discuss various optical techniques with appropriate examples that sensitively differentiate nanowire properties from those also found in the parent bulk material. Finally, phonon confinement effects are reviewed.

The Dielectric Function

The observable optical properties of materials can be related to their complex dielectric function [9.218, 219]. Since nanowire diameters are typically smaller than the wavelength of light, photons at visible or infrared wavelengths *see* a dielectric function for the composite nanowire array/substrate system that is different from that of the nanowire itself. Effective medium theories [9.220, 221] can be applied to model the nanowire and substrate as one continuous composite with a single complex dielectric function $(\epsilon_1 + \mathrm{i}\epsilon_2)$, where the real and imaginary parts of the dielectric function ϵ_1 and ϵ_2 are related to the index of refraction (n) and the absorption coefficient (K) by the relation $\epsilon_1 + \mathrm{i}\epsilon_2 = (n + \mathrm{i}K)^2$. One commonly observed consequence of effective medium theory is the lower (higher) energy of the plasma frequency (when $\epsilon_1(\omega)$ becomes zero), when the magnitude of the dielectric function of the host materials is larger (smaller) than that of the nanowire [9.222].

The dielectric function of the nanowires and the substrate can be separated out by using effective medium theory in reverse. Since the dielectric function of the host material is often known, and the dielectric function of the composite material can be measured (using reflection and transmission measurements in combination with either the Kramer–Kronig relations or Maxwell's equations), the complex dielectric function of the nanowires can be deduced. As an example, this technique was used to determine the frequency dependence of the real and imaginary parts of the dielectric function $\epsilon_1(\omega)$ and $\epsilon_2(\omega)$ for an array of parallel bismuth nanowires filling the pores of an alumina template [9.223].

If both the dielectric permittivity and the magnetic permeability are negative, the material will display a negative index of refraction. A material with a negative index of refraction has interesting physics and can be used to make a lens that is not limited by the diffraction limit [9.224]. Such materials are artificially designed composites with components of subwavelength dimensions, often metallic and magnetic (nano)wires. Negative refraction is also observed in hyperbolic metamaterials, where the permeability is positive and the permittivity tensor has both positive and negative components. Parallel metallic nanowires in a dielectric matrix satisfy this condition [9.225]. Negative refraction at visible light was first realized using a silver nanowire array in porous anodic alumina [9.226].

Characteristic Optical Properties of Nanowires

Reflection and transmission measurements are often used for nanowire characterization. Infrared spectroscopy, for example, can be used to determine the plasma frequency, free carrier density, and donor impurity concentration as a function of temperature. This is especially useful for nanowire research, since Hall effect measurements cannot be made on nanowires. For example, the bandgap of gallium nitride and its temperature dependence were determined by infrared spectroscopy in nanowires in the 10–50 nm range in comparison to bulk values [9.227].

Another common method used to study nanowires is photoluminescence spectrum (PL) or fluorescence spectroscopy. PL has been used to study many properties of nanowires, such as the optical gap behavior, oxygen vacancies in ZnO nanowires [9.66], strain in Si nanowires [9.229], and quantum confinement effects in InP and Si nanowires [9.228, 230]. Figure 9.36 shows the photoluminescence spectrum of InP nanowires as a function of wire diameter, thereby providing direct information on the effective bandgap. As the wire diameter of an InP nanowire is decreased so that it becomes smaller than the bulk exciton diameter of 19 nm, quantum confinement effects set in, and the bandgap is increased. This results in an increase in the PL peak energy. The smaller the effective mass, the larger the quantum confinement effects. When the shift in the peak energy as a function of nanowire diameter (Fig. 9.36) is analyzed using an effective mass model, the reduced effective mass of the ex-

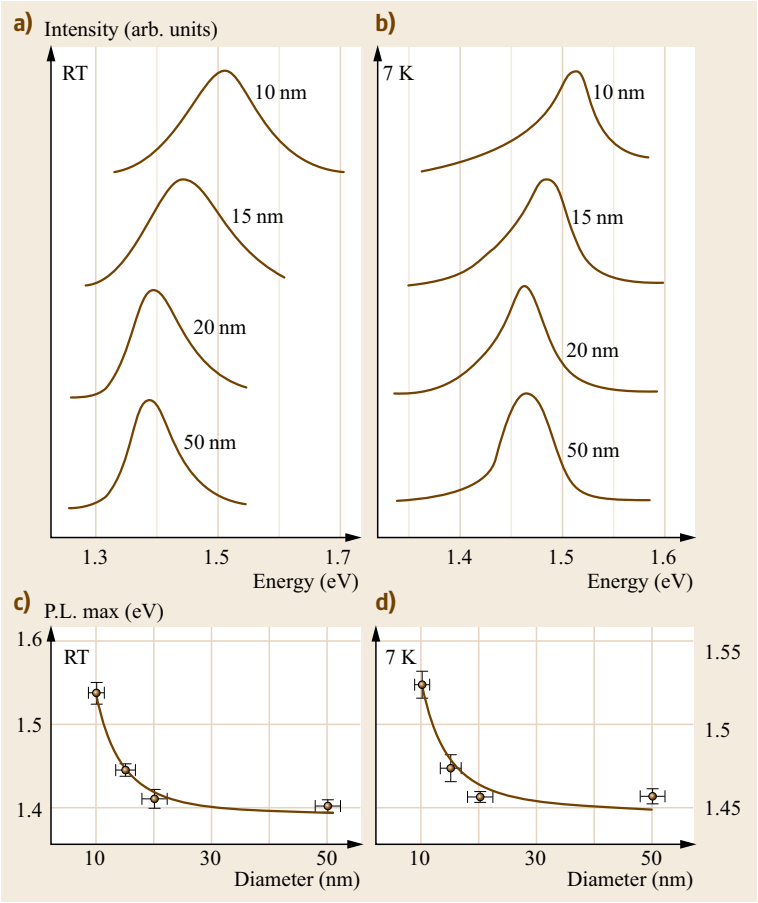

Fig. 9.36 Photoluminescence of InP nanowires of varying diameters at 7 K (**b**,**d**) and room temperature (**a**,**c**) showing quantum confinement effects of the exciton for wire diameters of less than 20 nm (after [9.228])

citon is deduced to be $0.052m_0$, which agrees quite well with the literature value of $0.065m_0$ for bulk InP. Although the line widths of the PL peak for the small-diameter nanowires (10 nm) are smaller at low temperature (7 K), strong quantum confinement and bandgap tunability effects persist at room temperature and thus are significant for photonics applications of nanowires (Sect. 9.3.2).

The resolution of photoluminescence (PL) optical imaging of a nanowire is, in general, limited by the wavelength of light. However, when a sample is placed very close to the detector, the light is not given a chance to diffract, and so samples much smaller than the wavelength of light can be resolved. This technique is known as near-field scanning optical microscopy (NSOM) and has been used to successfully image nanowires [9.231]. For example, Fig. 9.37 shows the topographical (a) and (b) NSOM PL images of a single ZnO nanowire.

Magneto-optics can be used to measure the electronic band structure of nanowires. For example, magneto-optics in conjunction with photoconductance has been proposed as a tool to determine band parameters of nanowires, such as the Fermi energy, electron effective mass, and the number of subbands to be considered [9.232]. Since different nanowire subbands have different electrical transmission properties, the electrical conductivity changes when light is used to excite electrons to higher subbands, thereby providing a method for studying the electronic structure of nanowires optically. Magneto-optics can also be used to study the magnetic properties of nanowires in relation to bulk properties [9.36, 233]. For example, the surface magneto-optical Kerr effect has been used to measure the dependence of the magnetic ordering temperature of Fe-Co alloy nanowires on the relative concentration of Fe and Co [9.233], and it was used to find that, unlike in the case of bulk Fe-Co alloys, cobalt in nanowires inhibits magnetic ordering. Nickel nanowires were found to have a strong increase in their magneto-optical activity with respect to bulk nickel. This increase is attributed to the plasmon resonance in the wires [9.234].

Nonlinear optical properties of nanowires have received particular attention since the nonlinear behavior

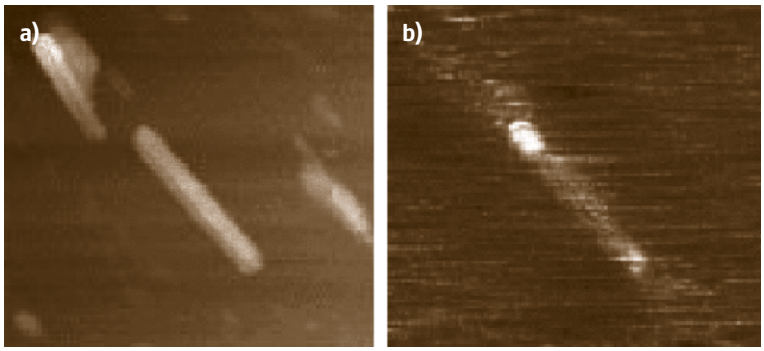

Fig. 9.37 **(a)** Topographical and **(b)** photoluminescence (PL) near-field scanning optical microscopy (NSOM) images of a single ZnO nanowire waveguide (after [9.231])

is often enhanced compared to bulk materials and the nonlinear effects can be utilized for a number of applications. One such study measured the second harmonic generation (SHG) and third harmonic generation (THG) in a single nanowire using near-field optical microscopy [9.235]. ZnO nanowires were shown to have strong SHG and THG effects that are highly polarization sensitive, and this polarization sensitivity can be explained on the basis of optical and geometrical considerations. Some components of the second harmonic polarization tensor are found to be enhanced in nanowires while others are suppressed as the wire diameter is decreased, and such effects could be of interest for device applications. It was also shown that the second-order nonlinearities are mostly wavelength-independent for $\lambda < 400\,\text{nm}$, which is in the transparent regime for ZnO, below the onset of bandgap absorption, and this observation is also of interest for device applications.

Reflectivity and transmission measurements have also been used to study the effects of quantum confinement and surface effects on the low-energy indirect transition in bismuth nanowires [9.236]. *Black* et al. investigated an intense and sharp absorption peak in bismuth nanowires, which is not observed in bulk bismuth. The energy position E_p of this strong absorption peak increases with decreasing diameter. However, the rate of increase in energy with decreasing diameter $|\partial E_\text{p}/\partial d_\text{W}|$ is an order of magnitude less than that predicted for either a direct interband transition or for intersubband transitions in bismuth nanowires. On the other hand, the magnitude of $|\partial E_\text{p}/\partial d_\text{W}|$ agrees well with that predicted for an indirect L-point valence to T-point valence band transition (Fig. 9.38). Since both the initial and final states for the indirect L–T point valence band transition downshift in energy as the wire diameter d_W is decreased, the shift in the absorption peak results from a difference between the effective masses and not from the actual value of either of the masses. Hence the diameter dependence of the absorption peak energy is an order of magnitude less for a valence-to-valence band indirect transition than for a direct interband L-point transition. Furthermore, the band-tracking effect for the indirect transition gives rise to a large value for the joint density of states, thus accounting for the high intensity of this feature. Figure 9.38 shows the experimentally observed transmission spectrum in bismuth nanowires of $\approx 45\,\text{nm}$ diameter (a), and the simulated optical transmission from an indirect transition in bismuth nanowires of $\approx 45\,\text{nm}$ diameter is also shown for comparison in (b). The indirect L–T point valence band transition mechanism [9.237] is also consistent with observations of the effect on the optical spectra of a decrease in the nanowire diameter and of n-type doping of bismuth nanowires with Te.

Phonon Confinement Effects

Phonons in nanowires are spatially confined by the nanowire cross-sectional area, crystalline boundaries, and surface disorder. These finite size effects give rise to phonon confinement, causing an uncertainty in the phonon wavevector, which typically gives rise to a frequency shift and lineshape broadening. Since zone center phonons tend to correspond to maxima in the phonon dispersion curves, the inclusion of contributions from a broader range of phonon wave vectors results in both a downshift in frequency and an asymmetric broadening of the Raman line, which develops a low-frequency tail. These phonon confinement effects have been theoretically predicted [9.238, 239] and experimentally observed in GaN [9.240], as shown in Fig. 9.39 for GaN nanowires with diameters in the range 10–50 nm. The application of these theoretical models indicates that broadening effects should be noticeable as the wire diameter in GaN nanowires decreases to $\approx 20\,\text{nm}$. When the wire diameter decreases further to $\approx 10\,\text{nm}$, the frequency downshift and asymmetric Raman line broadening effects should become observable in the Raman spectra for the GaN nanowires but are not found in the corresponding spectra for bulk GaN.

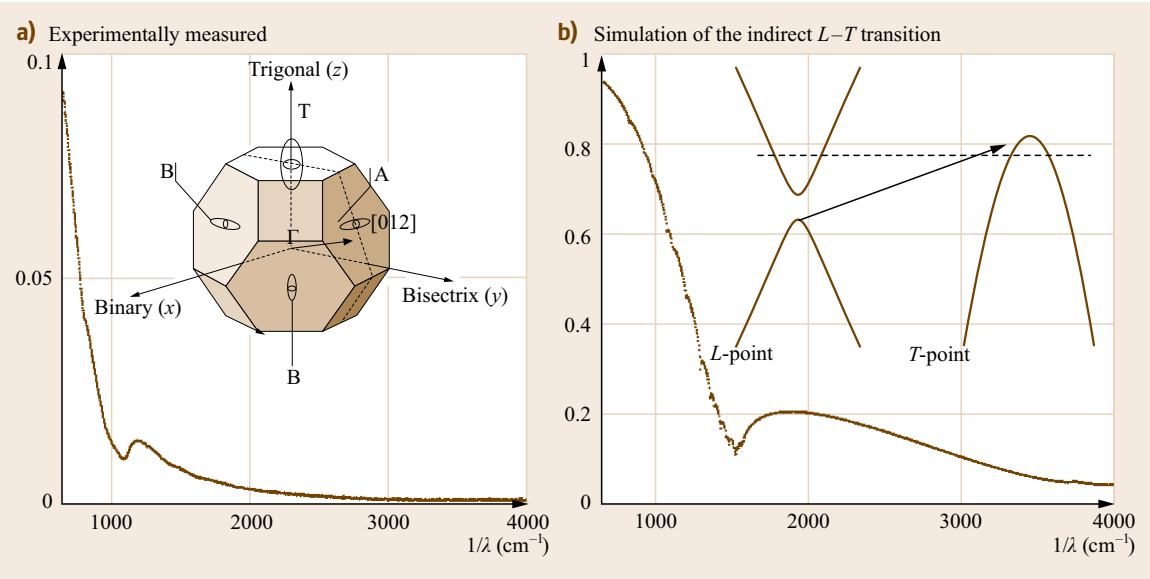

Fig. 9.38 **(a)** The measured optical transmission spectra as a function of wavenumber $(1/\lambda)$ of a ≈ 45 nm diameter bismuth nanowire array. **(b)** The simulated optical transmission spectrum resulting from an indirect transition of an L-point electron to a T-point valence subband state. The *insert* in **(a)** shows the bismuth Brillouin zone, and the locations of the T-point hole and the three L-point electron pockets, including the nondegenerate A, and the doubly degenerate B pockets. The *insert* in **(b)** shows the indirect L–T point electronic transition induced by a photon with an energy equal to the energy difference between the initial and final states minus the phonon energy (about 100 cm^{-1}) needed to satisfy conservation of energy in a Stokes process (after [9.237])

The experimental spectra in Fig. 9.39 show the four $A_1 + E_1 + 2E_2$ modes expected from symmetry considerations for bulk GaN crystals. Two types of quantum confinement effects are observed. The first type is the observation of the downshift and the asymmetric broadening effects discussed above. Observations of such downshifts and asymmetric broadening have also been reported in 7 nm-diameter Si nanowires [9.241]. A second type of confinement effect found in Fig. 9.39 for GaN nanowires is the appearance of additional Raman features not found in the corresponding bulk spectra and associated with combination modes, and a zone boundary mode. Resonant enhancement effects were also observed for the $A_1(\text{LO})$ phonon at 728 cm^{-1} at higher laser excitation energies [9.240].

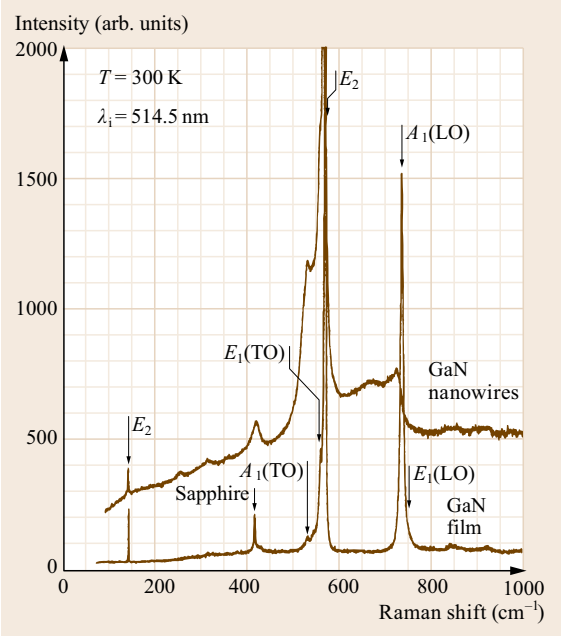

Fig. 9.39 Room-temperature Raman scattering spectra of GaN nanowires and of a 5 μm-thick GaN epilayer film with green (514.5 nm) laser excitation. The Raman scattering response was obtained by dividing the measured spectra by the Bose–Einstein thermal factor (after [9.240]) ►

9.3 Applications

In the preceding sections we have reviewed many of the central characteristics that make nanowires in some cases similar to and in some cases very different from their parent materials. We have also shown that some properties are diameter dependent, and these properties are therefore tunable during synthesis. Thus, nanowires offer a new toolbox of materials for engineers to design systems that could benefit in unprecedented ways from both the unique and tunable properties of nanowires and the small sizes of these nanostructures. As the synthetic methods for the production of nanowires continue to mature (Sect. 9.1) and nanowires are made in reproducible and cost-effective ways, the number of applications utilizing nanowires will continue to expand. This is a timely development, as the semiconductor industry will soon be reaching what seems to be its limit in feature size reduction, and approaching a classical-to-quantum size transition. At the same time, the field of biotechnology is expanding through the availability of tremendous genome information and innovative screening assays. Since nanowires are similar in size to the shrinking electronic components and to cellular biomolecules, it is only natural for nanowires to be good candidates for applications in these fields. Commercialization of nanowire devices, however, will require reliable mass production, effective assembly techniques, and quality control methods.

In this section, applications of nanowires to electronics (Sect. 9.3.1), optics (Sect. 9.3.2), energy (Sect. 9.3.3), chemical and biochemical sensing (Sect. 9.3.4), and magnetic media (Sect. 9.3.5) are discussed.

9.3.1 Electrical Applications

Nanowires are uniquely suited for some electrical applications. They are nano-sized in two dimensions and have one dimension that is not confined, providing a path for electrical conduction without the need for tunneling or carrier hopping. The microelectronics industry continues to face technological and economic challenges as the device feature size is decreased, especially below 20 nm. The self-assembly of nanowires might present a way to construct unconventional devices that do not rely on improvements in photolithography and, therefore, do not necessarily imply increasing fabrication costs. In addition, unlike traditional silicon processing, different semiconductors can be used simultaneously in nanowire devices to produce diverse functionalities. Not only can wires of different materials be combined, but a single wire can be made of different materials. For example, junctions of GaAs and GaP nanowire segments show rectifying behavior [9.111], thus demonstrating that good electronic interfaces between two different semiconductors can be achieved in the synthesis of multicomponent nanowires.

Electronic devices made from nanowires could also hold advantages due to their unique morphology. For example, in bulk field-effect transistors (FETs), the depletion layer formed below the source and drain region results in a source-drain capacitance that limits the operation speed. However, in nanowires, the source-drain contact can be wrapped around the semiconductor wire and thus the depletion layer can be limited to the nanowire volume inside the contact. Thus, depending on the device design, the source-drain capacitance in nanowires could be greatly minimized and possibly eliminated.

Device functionalities common in conventional semiconductor technologies, such as p-n junction diodes [9.167], field-effect transistors [9.169], logic gates [9.167], and light-emitting diodes [9.111, 242], have been demonstrated in nanowires, showing their promise as building blocks that could be used to construct complex integrated circuits by employing the *bottom-up* paradigm. In fact, as of June 2017 there are over 8000 US patent and patent applications containing the words *nanowire* and *transistor*. Several approaches have been investigated to form nanowire diodes (Sect. 9.2.2). For example, Schottky diodes can be formed by contacting a GaN nanowire with Al electrodes [9.168]. Furthermore, p-n junction diodes can be formed at the crossing of two nanowires, such as the crossing of n- and p-type InP nanowires doped by Te and Zn respectively [9.242], or Si nanowires doped by phosphorus (n-type) and boron (p-type) [9.243]. In addition to the crossing of two distinctive nanowires, heterogeneous junctions have also been constructed inside a single wire, either along the wire axis in the form of a nanowire superlattice [9.111], or perpendicular to the wire axis by forming a core-shell structure of silicon and germanium [9.151]. These various nanowire junctions not only possess current rectifying properties (Fig. 9.24) expected of bulk semiconductor devices, but they also exhibit electroluminescence (EL) that may be useful for optoelectronic applications, as shown in Fig. 9.40 for the electroluminescence of a crossed junction of n- and p-type InP nanowires [9.242] (see also Sect. 9.3.2).

The conductance of a semiconductor nanowire can be significantly modified by applying voltage at a third gate terminal, implying the utilization of nanowires in field-effect transistors (FETs). This gate terminal can either be the substrate [9.39, 244–247], a separate metal contact located close to the nanowire [9.248],

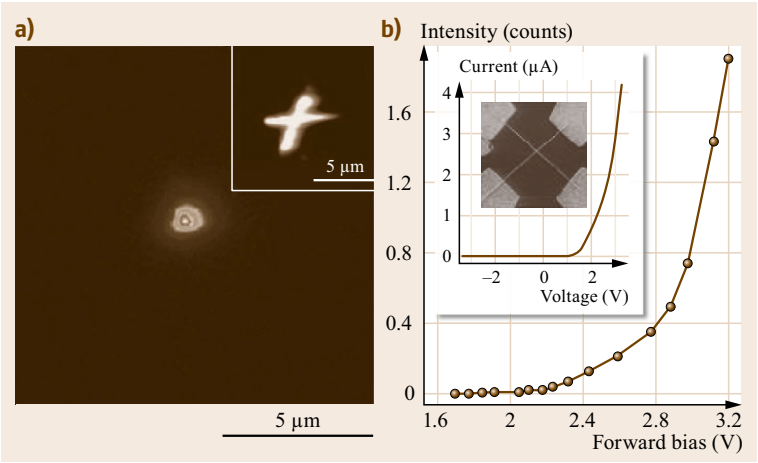

Fig. 9.40a,b Optoelectrical characterization of a crossed nanowire junction formed between 65 nm n-type and 68 nm p-type InP nanowires. **(a)** Electroluminescence (EL) image of the light emitted from a forward-biased nanowire p-n junction at 2.5 V. *Inset*, photoluminescence (PL) image of the junction. **(b)** EL intensity as a function of operation voltage. *Inset*, the SEM image and the *I–V* characteristics of the junction (after [9.242])

or another nanowire with a thick oxide coating in the crossed nanowire junction configuration [9.167]. Various logic devices performing basic logic functions have been demonstrated using nanowire junctions [9.167], as shown in Fig. 9.41 for the OR and AND logic gates constructed from two-by-one and one-by-three nanowire p-n junctions respectively. By functionalizing nanowires with redox-active molecules to store charge, nanowire FETs were demonstrated with two-level [9.169] and with eight-level [9.249] memory effects, which may be used for non-volatile memory or as switches. In another advance, In_2O_3 nanowire FETs with high-k dielectric materials were demonstrated, and substantially enhanced performance was obtained due to the highly efficient coupling of the gate [9.250]. A vertical FET with a surrounding gate geometry has also been demonstrated, which has the potential for high-density nanoscale memory and logic devices [9.251]. In addition, nanowire transistors were made without conventional doping [9.252, 253]. In these devices the gate surrounds the nanowire and fully or partially depletes the nanowire, thus controlling the carrier transport between the source and drain. These nanowire transistors were used in field-programmable logic arrays (FPGA), using an order of magnitude less area and operating power compared to conventional CMOS designs [9.252].

One challenge in making wrap-around transistors is finding a low-cost way to make the gate contact. For the application of tactile imaging, *Wu* et al. demonstrated the use of piezotronic ZnO nanowires that do not require a wrap-around gate [9.254]. The pressure applied to a ZnO nanowire in an array leads to a change in the polarization of immobile ions in the crystal that are present at the interface of the metal contact and the nanowire. This allows pressure to be sensed electrically without needing a gate terminal in each device.

Nanowires have also been proposed for applications associated with electron field emission [9.255, 256], such as flat panel displays, because of their small diameter and large curvature at the nanowire tip, which may reduce the threshold voltage for electron emission [9.257]. In this regard, the demonstration of very high field emission currents from the sharp tip ($\approx$ 10 nm radius) of a Si cone [9.255], from carbon nanotubes [9.258], from Si nanowires inside a carbon nanotube [9.259], and from Co nanowires [9.260], has stimulated interest in this potential area of application for nanowires.

Although the application of nanowires to thermoelectrics appears very promising, these materials are still in the research phase of the development cycle and are far from being commercialized. One challenge for thermoelectric devices based on nanowires lies in finding a suitable host material that will not reduce ZT too much due to the unwanted heat conduction through the host material. Therefore, the host material should have a low thermal conductivity and occupy a volume fraction in the composite material that is as low as possible, while still providing the quantum confinement and the support for the nanowires. In addition, the technology to scale up the sequential bonding of individual nanowires by dopant type (p-type to n-type to p-type, and so on) still needs to be developed.

Meshes of nanowires in the percolation limit have a combination of mechanical, electrical, and optical properties that make them useful for displays and tactile devices. Silver nanowire meshes, in particular, are being tested as transparent conduction films since their properties were shown to be similar to those of state-of-the-art indium tin oxide (ITO) [9.261]. These films are prepared from Ag nanowire suspensions, allowing for inkjet printing and low-temperature processing.

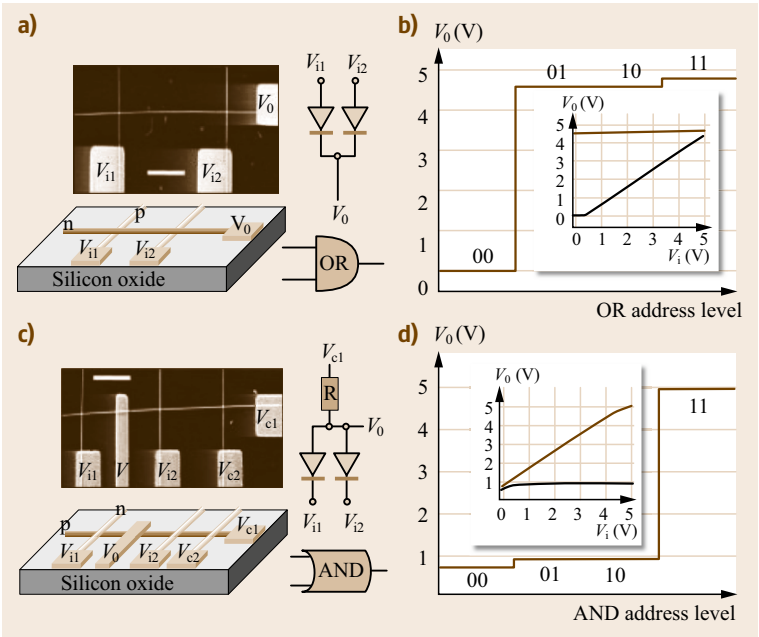

Fig. 9.41 Nanowire logic gates: **(a)** Schematic of logic OR gate constructed from a two (p-Si) by one (n-GaN) crossed nanowire junction. The *inset* shows the SEM image (scale bar: 1 μm) of an assembled OR gate and the symbolic electronic circuit. **(b)** The output voltage of the circuit in **(a)** versus the four possible logic address level inputs: (0,0); (0,1); (1,0); (1,1), where logic 0 input is 0 V and logic 1 is 5 V (same for below). **(c)** Schematic of logic AND gate constructed from a one (p-Si) by three (n-GaN) crossed nanowire junction. The *inset* shows the SEM image (scale bar: 1 μm) of an assembled AND gate and the symbolic electronic circuit. **(d)** The output voltage of the circuit in **(c)** versus the four possible logic address level inputs (after [9.167])

9.3.2 Optical Applications

Nanowires also hold promise for optical applications. One-dimensional systems exhibit a singularity in their joint density of states, allowing quantum effects in nanowires to be optically observable, sometimes even at room temperature. Since the density of states of a nanowire in the quantum limit (small wire diameter) is highly localized in energy, the available states quickly fill up with electrons as the intensity of the incident light is increased. This filling up of the subbands, as well as other effects that are unique to low-dimensional materials, lead to strong optical nonlinearities in quantum wires. Quantum wires may thus yield optical switches with a lower switching energy and increased switching speed compared to currently available optical switches.

Light-emitting diodes (LEDs) have been achieved in junctions between a p-type and an n-type nanowire (Fig. 9.40) [9.242] and in superlattice nanowires with p-type and n-type segments [9.111]. The light emission was localized to the junction area, and was polarized in the superlattice nanowire. An electrically driven laser was fabricated from CdS nanowires. The devices were fabricated by patterning a metal contact onto an n-type CdS nanowire, which resided on a p^+ silicon wafer. The cleaved ends of the wire formed the laser cavity, so that in forward bias, the light characteristic of lasing was observed at the end of the wire [9.262]. LEDs have also been achieved with core-shell structured nanowires made of n-GaN/InGaN/p-GaN [9.263].

Light emission from quantum wire p-n junctions is especially interesting for laser applications, because quantum wires can form lasers with lower excitation thresholds than their bulk counterparts and they also exhibit decreased sensitivity of performance to temperature [9.264]. Furthermore, the emission wavelength can be tuned for a given material composition by simply altering the geometry of the wire.

Lasing action has been reported in ZnO nanowires with wire diameters that are much smaller than the wavelength of the light emitted ($\lambda = 385\,\text{nm}$) [9.110] (Fig. 9.42). Since the edges and lateral surfaces of ZnO nanowires are faceted (Sect. 9.2.1), they form optical cavities that sustain desired cavity modes. Compared to conventional semiconductor lasers, the exciton laser action employed in zinc oxide nanowire lasers exhibits a lower lasing threshold ($\approx 40\,\text{kW/cm}^2$) than their 3-D counterparts ($\approx 300\,\text{kW/cm}^2$). In order to utilize exciton confinement effects in the lasing action, the exciton binding energy ($\approx 60\,\text{meV}$ in ZnO) must be greater than the thermal energy ($\approx 26\,\text{meV}$ at 300 K). Decreasing the wire diameter increases the excitation binding energy and lowers the threshold for lasing. PL NSOM imaging confirmed the waveguiding properties of the anisotropic and the well-faceted structure of ZnO nanowires, limiting the emission to the tips of the ZnO nanowires [9.231]. Time-resolved studies have illuminated the dynamics of the emission process [9.265].

Lasing nanowires were also obtained with other materials systems, such as ZnS nanowires in anodic aluminum oxide templates [9.266], GaN nanowires

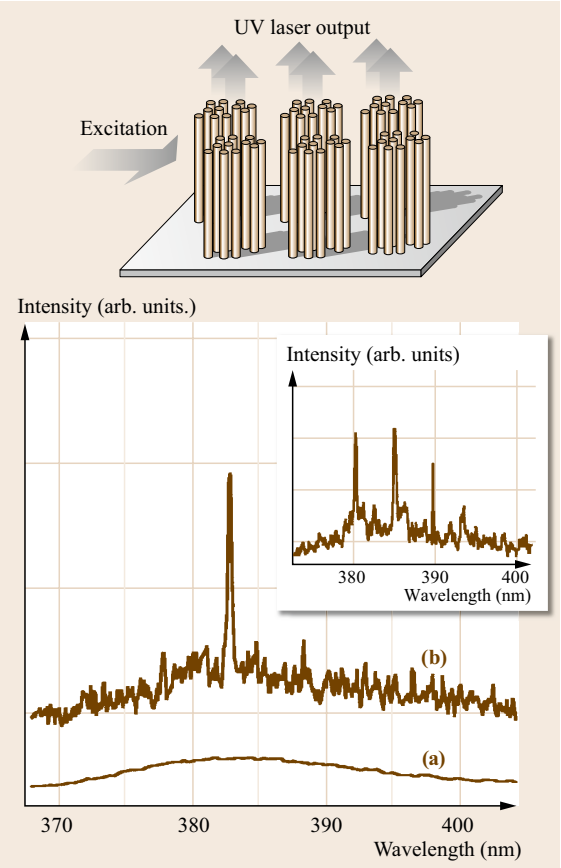

Fig. 9.42 A schematic of lasing in ZnO nanowires and the PL spectra of ZnO nanowires at two excitation intensities. The emission spectrum of trace (a) is taken below the lasing threshold (20 kW/cm^2) and the spectrum of trace (b) above it (100 kW/cm^2) (after [9.110])

[9.267], and a low-lasing-threshold, self-organized GaN(core)/AlGaN(shell) structure [9.268].

Nanowires have also been demonstrated to have good waveguiding properties. Quantitative studies of cadmium sulfide (CdS) nanowire structures show that light propagation takes place with only moderate losses through sharp and even acute angle bends. In addition, active devices made with nanowires have shown that efficient injection into and modulation of light through nanowire waveguides can be achieved [9.269]. By linking ZnO nanowire light sources to SnO_2 waveguides, the possibility of optical integrated circuitry is introduced [9.270].

Nanowire photodetectors were also proposed. ZnO nanowires were found to display a strong photocurrent response to ultraviolet (UV) light irradiation [9.271]. The conductivity of the nanowire increased by four orders of magnitude compared to the dark state. The response of the nanowire was reversible, and selective to photon energies above the bandgap, suggesting that ZnO nanowires could be good candidates for optoelectronic switches.

Nanowires have been also proposed for another type of optical switching. Light with its electric field normal to the wire axis excites a transverse free carrier resonance inside the wire, while light with its electric field parallel to the wire axis excites a longitudinal free carrier resonance inside the wire. Since nanowires are highly anisotropic, these two resonances occur at two different wavelengths and thus result in absorption peaks at two different energies. Gold nanowires dispersed in an aqueous solution align along the electric field when a DC voltage is applied. The energy of the absorption peak can be toggled between the transverse and longitudinal resonance energies by changing the alignment of the nanowires under polarized light illumination using an electric field [9.272, 273]. Thus, electro-optical modulation is achieved.

Nanowires may also be used as barcode tags for optical readout. Nanowires containing gold, silver, nickel, palladium, and platinum were fabricated [9.216] by electrochemical filling of porous anodic alumina, so that each nanowire consisted of segments of various metal constituents. Thus many types of nanowires can be made from a handful of materials, and identified by the order of the metal segments along their main axis, and the length of each segment. Barcode readout is possible by reflectance optical microscopy. The segment length is limited by the Rayleigh diffraction limit, and not by synthesis limitations, and thus can be as small as 145 nm. Figure 9.43a shows an optical image of many Au-Ag-Au-Ag barcoded wires, where the silver segments show higher reflectivity. Figure 9.43b is a backscattering mode field electron SEM (FE-SEM) image of a single nanowire, highlighting the composition and segment length variations along the nanowire.

Nanowires have found applications in solar cells or photovoltaics. Both the large surface area and the high conductivity along the length of nanowires are favorable for their use in photovoltaics. An early example involved n-type nanorods for inorganic-organic solar cells [9.274], which offer promise from a manufacturing and cost-effectiveness standpoint. In a hybrid nanocrystal-organic solar cell, the incident light forms bound electron-hole pairs (excitons) in both the inorganic nanocrystal and in the surrounding organic medium. These excitons diffuse to the inorganic-organic interface and disassociate to form an electron and a hole. Since conjugated polymers usually have poor electron mobilities, the inorganic phase is chosen to have a higher electron affinity than the organic phase so that the organic phase carries the holes and the

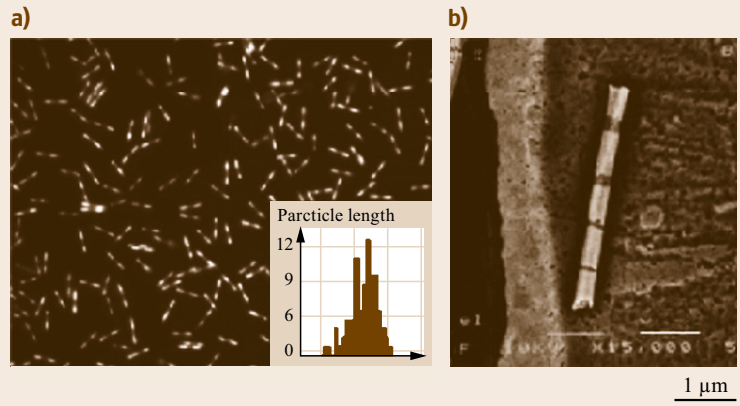

Fig. 9.43 **(a)** An optical image of many short barcoded Au-Ag-Au-Au wires and **(b)** an FE-SEM image of an Au/Ag barcoded wire with multiple strips of varying length. The *insert* in **(a)** shows a histogram of the particle lengths for 106 particles in this image (after [9.216])

semiconductor carries the electrons. The separated electrons and holes drift to the external electrodes through the inorganic and organic materials respectively. However, only those excitons formed within an exciton diffusion length from an interface can dissociate before recombining, and therefore the distance between the dissociation sites limits the efficiency of a solar cell. A solar cell prepared from a composite of CdSe nanorods inside poly(3-ethylthiophene) [9.274] yielded monochromatic power efficiencies of 6.9% and power conversion efficiencies of 1.7% under air mass AM1.5 (AM) illumination. The nanorods provide a large surface area with good chemical bonding to the polymer for efficient charge transfer and exciton dissociation. Furthermore, they provide a good conduction path for the electrons to reach the electrode. Their enhanced absorption coefficient and their tunable bandgap are also characteristics that can be used to enhance the energy conversion efficiency of solar cells.

Inorganic solar cells have the highest efficiencies to date, and nanowire photovoltaics can be an avenue for reduced cost and improved efficiency, by reducing material usage, increasing light absorption, and reducing recombination. Sol Voltaics AB is working to commercialize nanowire solar cells using a low-cost process based on VLS-grown vertical nanowire arrays with built-in axial p-n junctions [9.275, 276]. Devices of InP nanowires and GaAs nanowires achieved 13.8% and 15.3% efficiencies respectively. Silicon nanowires have also been used to make high-efficiency solar cells. Vertically aligned silicon nanowire arrays for solar cells are often made by either MACE or RIE (Sect. 9.1.3). Many studies on silicon nanowires put the p-n junction radially inside the wires [9.277]. These nanowire solar cells may be able to circumvent the Shockley–Queisser limit [9.278]. In radially doped nanowires, the solar-cell junction runs down the nanowire axis, and due to their small diameter, photocarriers are always generated near the junction. Thus in radially doped nanowires, hot carriers can be extracted out of the cell before they relax to the band edge.

Solar cells with silicon nanowire arrays on bulk silicon and the junction inside the bulk silicon are being commercialized by Advanced Silicon Group [9.279]. This cell design combines some of the advantages of nanowire cells with traditional silicon photovoltaics. In particular, these nanowire cells (sometimes called black silicon cells) have very low reflection and efficiently trap light inside the solar cell, with both effects leading to improved efficiency. Since the nanowires are smaller than the wavelength of light, the incident light sees an effective medium (Sect. 9.2.4) [9.280]. By tapering the wires, the index of refraction can be graded leading to a very low reflection of light. In black silicon cells, the junction is placed below the nanowires. It is formed by standard doping in the bulk single-crystal silicon substrate. Such pristine junctions are critical for low carrier recombination, low dark current, and thus high-efficiency cells. Pristine junctions are more challenging to create in the radial nanowire cell design.

9.3.3 Energy Applications

Energy Storage

Nanowires have been researched for energy application. Electrochemical and photoelectrochemical systems benefit from the nanowire array high surface area and one-dimensional conductivity. Individual nanowires can be used as in-situ electrochemical probes to explore intrinsic electrochemical processes and behaviors at the nanoscale.

Silicon has the highest lithium-ion absorption capacity of any known anode material for lithium ion batteries, but it expands and contracts by four times its volume when charged and discharged. This extensive expansion leads to pulverization of the electrode mate-

rial and the capacity of the anode quickly degrades with cycling. Nanowires allow for expansion and contraction during lithiation and delithiation in the radial direction while maintaining the structural integrity of the anode. In addition, compared to silicon nanoparticles, nanowires allow for conduction down the nanowire axis [9.281]. *Mai* et al. reported the characterization of single nanowire anode capacity fading in Li ion–based energy storage devices [9.282], while *Oleshko* et al. incorporated all the battery components in a single heterostructure nanowire for a detailed structural and electrochemical performance study using in-situ multimode analytical STEM imaging [9.283]. Several companies are commercializing silicon nanowire anodes including Nexeon, Advanced Silicon Group, Silexta, and Amprius [9.284–286]. Complete nanowire nanobattery arrays embedded in porous anodic alumina were demonstrated; however, these employed vanadium oxide chemistry [9.287].

Qui and coauthors used TiO_2 passivated InP nanowire arrays to create a photocatalytic system that reduces CO_2 with water to produce methanol [9.288]. More recently, the importance of uniformity of the nanowires in photocatalytic reactions was demonstrated with individual Si nanowire devices [9.289].

Nanowire-based capacitors can be readily produced as arrays in templates, for example by ALD [9.290]. Synthesis of individual nanowire capacitors as coaxial heterostructures by CVD offers extensive material flexibility. Following this approach, *Ajayan* et al. demonstrated the fabrication of single-nanowire capacitors made of a Cu-Cu_2O-C nanowire with capacitance values up to $140\,\mu F/cm^2$, well above the values reported for metal-insulator-metal micro-/nanocapacitors [9.291].

Piezoelectric Generators

Mechanical energy is abundant in the environment and in industrial processes but such energy is usually wasted, be it in the form of mechanical vibration, hydraulic pressure, or air flow, among others. One way to harvest these forms of energy is through the piezoelectric effect, which converts mechanical energies into electricity. This effect is well known at the macroscale in bulk materials such as lead zirconate titanate (PZT) and lead magnesium niobate-lead titanate (PMN–PT). The development of energy nanogenerators, which convert mechanical energy into electricity using one-dimensional piezoelectric materials, now enables the harvesting of small-scale mechanical energy, which can, in turn, be used to charge electrochemical systems or to power low-consumption microdevices [9.292, 293]. *Wang* and *Song* reported the first piezoelectric nanogenerators in 2006. In this seminal work, an output voltage pulse of several millivolts was obtained after bending a ZnO nanowire with an AFM tip [9.294]. With the ultimate objective of improving energy conversion efficiency and output power for practical applications, much research in optimizing materials [9.295–297] and system design [9.298, 299] continues to be performed in the field of nanowire-based technology [9.300, 301].

The major types of piezoelectric nanogenerator structures include the vertically aligned nanowire networks, the laterally aligned nanowire arrays, and the nanowire-based nanocomposites. The fundamental working principle applicable to the various realizations of vertically aligned nanowire arrays, hinges on the electromechanical coupling of the semiconductor behavior and the piezoelectric property of the piezoelectric nanowire. In this case, the application of external stress induces the appearance of a piezoelectric potential along the nanowire, which affects the details of the Schottky barrier at the interface between the nanowire and metallic pads. This, in turn, accounts for the flow of electrons between the metallic electrodes, through the closed circuit, to ensure thermodynamic equilibrium. In addition to the original ZnO-based device, AFM tip-induced lateral bending was also demonstrated for nanowires with other chemical compositions such as GaN, CdS, InN, and ZnS [9.302–306]. To avoid the use of an AFM tip, simplify the fabrication process, and improve the device stability, *Xu* and coworkers proposed a vertical nanowire array integrated nanogenerator (VING), which is created by packaging an array of vertically aligned ZnO nanowires with polymethyl methacrylate (PMMA) and by connecting the nanowire with top and bottom flat electrodes [9.307]. ZnO VINGs are currently among the most popular nanogenerators. Moving beyond ZnO (which has a relatively low piezoelectric constant and therefore yields low-performance nanogenerators), researchers are also exploring more efficient nanowire perovskite piezoelectric materials such as $Pb(Zr, Ti)O_3$ (PZT) [9.308]. This path is promising but suffers from a number of difficulties that are absent in ZnO-based VINGs, namely a more difficult synthesis process and the limited flexibility of the substrate typically used for materials growth.

The first lateral type of piezoelectric nanogenerator (where deformation is always induced by laterally bending the nanowires via the substrate or by applying a pressure in the radial nanowire direction) was demonstrated by *Wang* et al. in 2007 [9.309]. This device is based on the voltage generation of an individual $BaTiO_3$ nanowire under periodic tensile mechanical load. The nanofabrication process of the flexural stage involves complex and expensive steps due to the need to manipulate materials of extremely small sizes. In con-

trast, laterally integrated nanogenerators (LINGs) using a flexible polymer substrate are not only easier to fabricate but also feature improved performance [9.310]. In addition to ZnO, LINGs were made using other nanowire materials, such as potassium sodium niobate, which have the advantage of displaying a much higher piezoelectric constant and a lower free charge carrier density (which reduces stray screening responsible for lower piezoelectric response), and of being biocompatible [9.311]. The field of LINGs is still fairly recent and much effort is being made to simplify the fabrication processes, including the development of a scalable sweeping-printing method for fabricating flexible devices with ZnO nanowire arrays [9.312], or a one-step fabrication of ZnO nanowire networks [9.307]. Notably, the development of electrospinning techniques has enabled the use of ultralong piezoelectric nanofibers and large-scale LING fabrication [9.313, 314].

A novel type of piezoelectric nanogenerator based on nanowire-polymer composites has been explored to simplify the fabrication process compared to that of VINGs and LINGs. In this case, the nanogenerator assembly consists of four functional layers: top and bottom electrodes, flexible substrate, and a nanowire-composite layer. This multilayer structure is reminiscent of that of conventional piezoelectric ceramics. While the composite may feature piezoelectric properties inferior to those of ceramics, the presence of the polymer matrix significantly enhances the flexibility of the device. Compared to VINGs and LINGs, where the device fabrication is largely dictated by the assembly process of the nanowire arrays, the nanowire-composite design can be easily obtained by directly mixing as-synthesized nanowires with the polymer matrix such as polydimethylsiloxane (PDMS). *Hu* et al. realized large output nanogenerators by rational unipolar assembly of conical ZnO nanowires [9.315] and similar structures were also reported for composites of $NaNbO_3$ or GaN nanowires mixed with PDMS [9.296, 316].

Although much effort has already been made in promoting the practical application of piezoelectric nanogenerators, a number of critical issues remain to be fully resolved. This includes issues related to the integration of nanogenerators for high-output power sources, the structural design for increasing the energy harvesting efficiency in different practical conditions, and the need for improved stability and reliability [9.300].

9.3.4 Chemical and Biochemical Sensing Devices

Sensors for chemical and biochemical substances with nanowires as the sensing probe are a very attractive application area for nanowires based on a variety of materials and specific applications. Nanowire sensors will potentially be smaller and more sensitive, demand less power, and react faster than their macroscopic counterparts. Arrays of nanowire sensors could, in principle, achieve nanometer-scale spatial resolution and therefore provide accurate real-time information regarding not only the concentration of a specific analyte but also its spatial distribution. Such arrays could be very useful, for example, for dynamic studies on the effects of chemical gradients on biological cells.

The operation of many sensors made with nanowires, nanotubes, or nano-contacts is based on the reversible change in the conductance of the nanostructure upon absorption of the agent to be detected. The increased sensitivity and faster response time of nanowires are a result of the large surface-to-volume ratio and the small cross-section available for conduction channels, thus increasing the interaction between stray fields and the charge carriers. In the bulk, on the other hand, the abundance of charges can effectively shield external fields, and the volume of material can afford many alternative conduction channels. Therefore, a stronger chemical stimulus and longer response time are necessary to observe changes in the physical properties of a 3-D sensor in comparison to a nanowire.

It is often necessary to modify the surface of the nanowires to achieve a strong interaction with the analytes that need to be detected. Surface modifications utilize the self-assembly, chemisorption, or chemical reactivity of selected organic molecules and polymers towards metal and oxide surfaces. Examples include thiols on gold, isocyanides on platinum, and siloxanes on silica. These surface coatings regulate the binding and chemical reactivity of other molecules towards the nanowire in a predictable manner [9.317].

Cui et al. placed silicon nanowires made by the VLS method (Sect. 9.1.2) between two metal electrodes and modified the silicon oxide coating of the wire through the addition of molecules that are sensitive to the analyte to be detected [9.318]. For example, a pH sensor was made by covalently linking an amine-containing silane to the surface of the nanowire. Variations in the pH of the solution into which the nanowire was immersed caused protonation and deprotonation of the $-NH_2$ and the $-SiOH$ groups on the surface of the nanowire. The variation in surface charge density regulates the conductance of the nanowire; due to the p-type characteristics of a silicon wire, the conductance increases with the addition of negative surface charge. The combined acid and base behavior of the surface groups results in an approximately linear dependence of the conductance on pH in the pH range 2–9, thus leading to a direct-readout pH meter. This same type of approach was used for the detection of

the binding of biomolecules, such as streptavidin using biotin-modified nanowires (Fig. 9.44). This nanowire-based device has high sensitivity and could detect streptavidin binding down to a concentration of 10 pM (10^{-12} mol). Subsequent results demonstrated the capabilities of these functionalized Si nanowire sensors as DNA sensors down to the femtomolar range [9.319].

A similar approach was used by *Favier* et al., who made a nanosensor for the detection of hydrogen from of an array of palladium nanowires between two metal contacts [9.53]. They demonstrated that nanogaps were present in their nanowire structure, and upon absorption of H_2 and formation of Pd hydride, the nanogap structure would close and improve the electrical contact, thereby increasing the conductance of the nanowire array. The response time of these sensors was 75 ms, and they could operate in the range 0.5–5% H_2 before saturation occurred.

A mechanical sensing paradigm typically employs the nanowires as oscillating cantilevers and detects shifts in their mechanical resonance frequency (related to changes in cantilever mass) upon chemical binding events. As above, molecular binding specificity is achieved through functionalization of the nanowire surface. Using a 103 µm-long ZnO nanowire, *Wang* et al. measured a 26 pg weight with ≈ 10% error and 1.2 pg sensitivity [9.320]. These conditions allow for the detection of small nanoparticles (e.g., in aerosols). Single-macromolecule detection was demonstrated through a multimode frequency analysis in a sophisticated doubly clamped nanoelectromechanical resonator [9.321, 322].

Nanowires can act as waveguides to deliver optical signals in the near field and improve signal-to-noise ratio and spatial resolution in spectroscopic measurements [9.323]. *Yang* et al. utilized a tin oxide nanowire to guide the optical signal from a laser passing through the sample. Light scattered by the end of the nanowire was detected in the far field to obtain the PL or Raman spectrum of the analyte. Tin oxide nanowires were further used as a probe to poke through a cell's membrane and collect PL light from the cytoplasm, demonstrating a nanoscale endoscope [9.324]. The device sensed the position of luminescent quantum dots artificially positioned in the cell. Waveguiding in silver nanowires through excitation of surface plasmon polaritons has also been employed to sense molecules through surface-enhanced Raman scattering and other plasmonic effects [9.325].

9.3.5 Magnetic Applications

It has been demonstrated that arrays of single-domain magnetic nanowires can be prepared with controlled nanowire diameter and length, aligned along a common direction and arranged in a close-packed ordered array (Sect. 9.1), and that the magnetic properties (coercivity, remanence, and dipolar magnetic interwire interaction) can be controlled to achieve a variety of magnetic applications [9.49, 88].

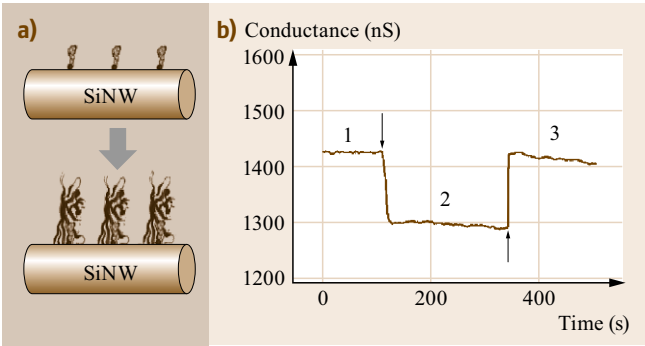

Fig. 9.44 **(a)** Streptavidin molecules bind to a silicon nanowire functionalized with biotin. The binding of streptavidin to biotin causes the nanowire to change its electrical resistance. **(b)** The electrical conductance of a biotin-modified silicon nanowire exposed to streptavidin in a buffer solution (regions 1 and 3) and with the introduction of a solution of antibiotin monoclonal antibody (region 2) (after [9.318])

The most interesting of these applications is for magnetic storage, where the large nanowire aspect ratio (length/diameter) is advantageous for preventing the onset of the *superparamagnetic* limit at which the magnetization direction in the magnetic grains can be reversed by the thermal energy $k_B T$, thereby resulting in loss of recorded data in the magnetic recording medium. The magnetic energy in a grain can be increased by increasing either the volume or the anisotropy of the grain. If the volume is increased, the particle size increases, so the resolution is decreased. For spherical magnetized grains, the superparamagnetic limit at room temperature is reached at 70 Gbit/in^2. In nanowires, the anisotropy is very large and yet the wire diameters are small, so that the magnetostatic switching energy can easily be above the thermal energy while the spatial resolution is large. For magnetic data storage applications, a large aspect ratio is needed for the nanowires in order to maintain a high coercivity, and a sufficient separation between nanowires is needed to suppress interwire magnetic dipolar coupling. Thus nanowires can form stable and highly dense magnetic memory arrays with packing densities in excess of 10^{11} wires/cm^2.

Developments in the controlled movement of domain walls in magnetic nanowires by short pulses of spin-polarized current show the possibility of nonvolatile memory devices with performance and relia-

bility comparable to conventional solid-state memory but at the affordability of conventional magnetic storage [9.326]. For instance, the racetrack memory design is a device made up of an array of horizontally or vertically oriented magnetic nanowires arranged on a silicon chip where individual spintronic read/write processes can operate on a train of tens of domain walls, thereby storing a series of data bits in each nanowire.

Moving beyond information storage, magnetic logic architectures, known as *domain-wall logic*, have the advantage of not requiring the use of transistors and therefore do not show significant heating associated with data switching [9.327]. A domain wall is a mobile interface between regions of magnetization aligned in opposite directions. In particular, a submicrometer planar nanowire made from a soft magnetic material such as Permalloy has been demonstrated as an excellent system featuring domain walls [9.328–330]. The large shape anisotropy of a nanowire provides a preferred magnetization alignment along the axis of the nanowires, leading to a robust binary information encoding. The role of the magnetic domain wall is to provide a transition edge in a changing signal. A logical *1* is defined as the magnetization pointing in the direction of propagation of domain walls and a logical *0* as the magnetization in the opposite direction. It was shown that cusp-shaped planar nanowires can be used to reverse the direction of magnetization, thereby providing the basis for the logical NOT operation [9.331]. Other basic logic functions, especially those with two-input functions, such as AND or OR, are also possible and are necessary elementary operations for computational applications. More complex logic circuits also require functions such as a fan-out structure, which creates two identical copies of an input signal and a cross-over structure, which makes it possible for two signals to pass over each other without interference [9.332].

9.4 Concluding Remarks

In this chapter, we reviewed the synthesis, characterization, and physical properties of nanowires, placing particular emphasis on nanowire properties that differ from those of their bulk counterparts and potential applications that might result from the special structures and properties of nanowires.

We have shown that the field of nanowire research continues to develop very rapidly year after year, driven by the development of a variety of complementary nanowire synthesis methods and effective tools for measuring nanowire structures and properties (Sects. 9.1 and 9.2). At present, much of the progress is at the demonstration-of-concept level, with many gaps in knowledge remaining to be elucidated, theoretical models to be developed, and new nanowire systems to be explored. Having demonstrated that many of the most interesting discoveries to date relate to nanowire properties not present in their bulk material counterparts, we can expect future research emphasis to be increasingly focused on smaller-diameter nanowires, where new unexplored physical phenomena related to quantum confinement effects are more likely to be found. We can also expect the development of applications to follow, some coming sooner and others later. Many promising applications are now at the early demonstration stage (Sect. 9.3), but are moving ahead rapidly because of their promise of new functionality not previously available in the fields of electronics, optoelectronics, biotechnology, magnetics, and energy conversion and generation, among others. Many exciting challenges remain in advancing both the nanoscience and the nanotechnological promise already demonstrated by the nanowire research described in this review.

Acknowledgments. In loving memory of our advisor, mentor, and friend Dr. Millie Dresselhaus who passed away during the production of this handbook.

O.R. acknowledges support from the National Science Foundation (DMR-1151614).

References

9.1 R.P. Feynman: There's plenty of room at the bottom, Eng. Sci. **23**, 22–36 (1960)

9.2 M.S. Dresselhaus, Y.-M. Lin, O. Rabin, A. Jorio, A.G. Souza Filho, M.A. Pimenta, R. Saito, G.G. Samsonidze, G. Dresselhaus: Nanowires and nanotubes, Mater. Sci. Eng. C **23**, 129–140 (2003), also in: Current trends in nanotechnologies: From materials to systems, Eur. Mater. Res. Soc. Symp. Proc., Vol. 140, ed. by W. Jantsch, H. Grimmeiss, G. Marietta (Elsevier, Amsterdam 2002)

9.3 R. Saito, G. Dresselhaus, M.S. Dresselhaus: *Physical Properties of Carbon Nanotubes* (Imperial College

Press, London 1998)
9.4 M.S. Dresselhaus, G. Dresselhaus, P. Avouris (Eds.): *Carbon Nanotubes: Synthesis, Structure, Properties and Applications*, Springer Ser. Top. Appl. Phys., Vol. 80 (Springer, Berlin, Heidelberg 2001) pp. 1–447
9.5 R.C. Haddon: Special issue on carbon nanotubes, Acc. Chem. Res. **35**, 997–1113 (2002)
9.6 Y. Mao, S.S. Wong: General, room-temperature method for the synthesis of isolated as well as arrays of single-crystalline ABO_4-type nanorods, J. Am. Chem. Soc. **126**, 15245–15252 (2004)
9.7 E. Braun, Y. Eichen, U. Sivan, G. Ben-Yoseph: DNA-templated assembly and electrode attachment of a conducting silver wire, Nature **391**, 775–778 (1998)
9.8 G. Sauer, G. Brehm, S. Schneider, K. Nielsch, R.B. Wehrspohn, J. Choi, H. Hofmeister, U. Gösele: Highly ordered monocrystalline silver nanowire arrays, J. Appl. Phys. **91**, 3243–3247 (2002)
9.9 K.E. Korte, S.E. Skrabalak, Y. Xia: Rapid synthesis of silver nanowires through a CuCl- or $CuCl_2$-mediated polyol process, J. Mater. Chem. **18**, 437–441 (2008)
9.10 S. Zhu, Y. Gao, B. Hu, J. Li, J. Su, Z. Fan, J. Zhou: Transferable self-welding silver nanowire network as high performance transparent flexible electrode, Nanotechnology **24**, 335202 (2013)
9.11 L.J. Andrés, M.F. Menéndez, D. Gómez, A.L. Martínez, N. Bristow, J.P. Kettle, A. Menéndez, B. Ruiz: Rapid synthesis of ultra-long silver nanowires for tailor-made transparent conductive electrodes: Proof of concept in organic solar cells, Nanotechnology **26**, 265201 (2015)
9.12 G.L. Hornyak, C.J. Patrissi, C.M. Martin: Fabrication, characterization and optical properties of gold nanoparticle/porous alumina composites: The non-scattering Maxwell–Garnett limit, J. Phys. Chem. B **101**, 1548–1555 (1997)
9.13 X.Y. Zhang, L.D. Zhang, Y. Lei, L.X. Zhao, Y.Q. Mao: Fabrication and characterization of highly ordered Au nanowire arrays, J. Mater. Chem. **11**, 1732–1734 (2001)
9.14 F. Kim, K. Sohn, J. Wu, J. Huang: Chemical synthesis of gold nanowires in acidic solutions, J. Am. Chem. Soc. **130**(44), 14442–14443 (2008) doi:10.1021/ja806759v
9.15 Y.-T. Cheng, A.M. Weiner, C.A. Wong, M.P. Balogh, M.J. Lukitsch: Stress-induced growth of bismuth nanowires, Appl. Phys. Lett. **81**, 3248–3250 (2002)
9.16 W. Shim, J. Ham, K.-I. Lee, W.Y. Jeung, M. Johnson, W. Lee: On-film formation of bi nanowires with extraordinary electron mobility, Nano Lett. **9**, 18–22 (2009) doi:10.1021/nl8016829
9.17 J. Heremans, C.M. Thrush, Y.-M. Lin, S. Cronin, Z. Zhang, M.S. Dresselhaus, J.F. Mansfield: Bismuth nanowire arrays: Synthesis, galvanomagnetic properties, Phys. Rev. B **61**, 2921–2930 (2000)
9.18 L. Piraux, S. Dubois, J.L. Duvail, A. Radulescu, S. Demoustier-Champagne, E. Ferain, R. Legras: Fabrication and properties of organic, metal nanocylinders in nanoporous membranes, J. Mater. Res. **14**, 3042–3050 (1999)
9.19 K. Hong, F.Y. Yang, K. Liu, D.H. Reich, P.C. Searson, C.L. Chien, F.F. Balakirev, G.S. Boebinger: Giant positive magnetoresistance of Bi nanowire arrays in high magnetic fields, J. Appl. Phys. **85**, 6184–6186 (1999)
9.20 A.J. Yin, J. Li, W. Jian, A.J. Bennett, J.M. Xu: Fabrication of highly ordered metallic nanowire arrays by electrodeposition, Appl. Phys. Lett. **79**, 1039–1041 (2001)
9.21 Z. Zhang, J.Y. Ying, M.S. Dresselhaus: Bismuth quantum-wire arrays fabricated by a vacuum melting and pressure injection process, J. Mater. Res. **13**, 1745–1748 (1998)
9.22 Z. Zhang, D. Gekhtman, M.S. Dresselhaus, J.Y. Ying: Processing and characterization of single-crystalline ultrafine bismuth nanowires, Chem. Mater. **11**, 1659–1665 (1999)
9.23 T.E. Huber, M.J. Graf, C.A. Foss, P. Constant: Processing and characterization of high-conductance bismuth wire array composites, J. Mater. Res. **15**, 1816–1821 (2000)
9.24 L. Li, G. Li, Y. Zhang, Y. Yang, L. Zhang: Pulsed electrodeposition of large-area, ordered $Bi_{1-x}Sb_x$ nanowire arrays from aqueous solutions, J. Phys. Chem. B **108**, 19380–19383 (2004)
9.25 M.S. Sander, A.L. Prieto, R. Gronsky, T. Sands, A.M. Stacy: Fabrication of high-density, high aspect ratio, large-area bismuth telluride nanowire arrays by electrodeposition into porous anodic alumina templates, Adv. Mater. **14**, 665–667 (2002)
9.26 M. Chen, Y. Xie, J. Lu, Y.J. Xiong, S.Y. Zhang, Y.T. Qian, X.M. Liu: Synthesis of rod-, twinrod-, and tetrapod-shaped CdS nanocrystals using a highly oriented solvothermal recrystallization technique, J. Mater. Chem. **12**, 748–753 (2002)
9.27 D. Xu, Y. Xu, D. Chen, G. Guo, L. Gui, Y. Tang: Preparation of CdS single-crystal nanowires by electrochemically induced deposition, Adv. Mater. **12**, 520–522 (2000)
9.28 D. Routkevitch, T. Bigioni, M. Moskovits, J.M. Xu: Electrochemical fabrication of CdS nanowire arrays in porous anodic aluminum oxide templates, J. Phys. Chem. **100**, 14037–14047 (1996)
9.29 L. Manna, E.C. Scher, A.P. Alivisatos: Synthesis of soluble and processable rod-, arrow-, teardrop-, and tetrapod-shaped CdSe nanocrystals, J. Am. Chem. Soc. **122**, 12700–12706 (2000)
9.30 D. Routkevitch, A.A. Tager, J. Haruyama, D. Al-Mawlawi, M. Moskovits, J.M. Xu: Nonlithographic nano-wire arrays: fabrication, physics, and device applications, IEEE Trans. Electron. Dev. **43**, 1646–1658 (1996)
9.31 D.S. Xu, D.P. Chen, Y.J. Xu, X.S. Shi, G.L. Guo, L.L. Gui, Y.Q. Tang: Preparation of II–VI group semiconductor nanowire arrays by dc electrochemical deposition in porous aluminum oxide templates, Pure Appl. Chem. **72**, 127–135 (2000)
9.32 R. Adelung, F. Ernst, A. Scott, M. Tabib-Azar, L. Kipp, M. Skibowski, S. Hollensteiner, E. Spiecker, W. Jäger, S. Gunst, A. Klein, W. Jägermann, V. Zaporojtchenko, F. Faupel: Self-assembled nanowire networks by deposition of copper onto layered-crystal

surfaces, Adv. Mater. **14**, 1056–1061 (2002)
9.33 T. Gao, G.W. Meng, J. Zhang, Y.W. Wang, C.H. Liang, J.C. Fan, L.D. Zhang: Template synthesis of single-crystal Cu nanowire arrays by electrodeposition, Appl. Phys. A **73**, 251–254 (2001)
9.34 D. Al-Mawlawi, N. Coombs, M. Moskovits: Magnetic-properties of Fe deposited into anodic aluminum-oxide pores as a function of particle-size, J. Appl. Phys. **70**, 4421–4425 (1991)
9.35 F. Li, R.M. Metzger: Activation volume of α-Fe particles in alumite films, J. Appl. Phys. **81**, 3806–3808 (1997)
9.36 A. Sugawara, T. Coyle, G.G. Hembree, M.R. Scheinfein: Self-organized Fe nanowire arrays prepared by shadow deposition on NaCl(110) templates, Appl. Phys. Lett. **70**, 1043–1045 (1997)
9.37 G.S. Cheng, L.D. Zhang, Y. Zhu, G.T. Fei, L. Li, C.M. Mo, Y.Q. Mao: Large-scale synthesis of single crystalline gallium nitride nanowires, Appl. Phys. Lett. **75**, 2455–2457 (1999)
9.38 G.S. Cheng, L.D. Zhang, S.H. Chen, Y. Li, L. Li, X.G. Zhu, Y. Zhu, G.T. Fei, Y.Q. Mao: Ordered nanostructure of single-crystalline GaN nanowires in a honeycomb structure of anodic alumina, J. Mater. Res. **15**, 347–350 (2000)
9.39 Y. Huang, X. Duan, Y. Cui, C.M. Lieber: Gallium nitride nanowire nanodevices, Nano Lett. **2**, 101–104 (2002)
9.40 X. Duan, C.M. Lieber: Laser-assisted catalytic growth of single crystal GaN nanowires, J. Am. Chem. Soc. **122**, 188–189 (2000)
9.41 A.D. Berry, R.J. Tonucci, M. Fatemi: Fabrication of GaAs and InAs wires in nanochannel glass, Appl. Phys. Lett. **69**, 2846–2848 (1996)
9.42 J.R. Heath, F.K. LeGoues: A liquid solution synthesis of single-crystal germanium quantum wires, Chem. Phys. Lett. **208**, 263–268 (1993)
9.43 Y. Wu, P. Yang: Germanium nanowire growth via simple vapor transport, Chem. Mater. **12**, 605–607 (2000)
9.44 Y.F. Zhang, Y.H. Tang, N. Wang, C.S. Lee, I. Bello, S.T. Lee: Germanium nanowires sheathed with an oxide layer, Phys. Rev. B **61**, 4518–4521 (2000)
9.45 S.J. May, J.-G. Zheng, B.W. Wessels, L.J. Lauhon: Dendritic nanowire growth mediated by a self-assembled catalyst, Adv. Mater. **17**, 598–602 (2005)
9.46 S. Han, C. Li, Z. Liu, B. Lei, D. Zhang, W. Jin, X. Liu, T. Tang, C. Zhou: Transition metal oxide core-shell nanowires: Generic synthesis and transport studies, Nano Lett. **4**, 1241–1246 (2004)
9.47 M.P. Zach, K.H. Ng, R.M. Penner: Molybdenum nanowires by electrodeposition, Science **290**, 2120–2123 (2000)
9.48 L. Sun, P.C. Searson, L. Chien: Electrochemical deposition of nickel nanowire arrays in single-crystal mica films, Appl. Phys. Lett. **74**, 2803–2805 (1999)
9.49 K. Nielsch, R. Wehrspohn, S. Fischer, H. Kronmüller, J. Barthel, J. Kirschner, U. Gösele: Magnetic properties of 100 nm nickel nanowire arrays obtained from ordered porous alumina templates, MRS Symp. Proc. **636**, D1.9-1–D1.9-6 (2001)
9.50 Y. Wang, X. Jiang, T. Herricks, Y. Xia: Single crystalline nanowires of lead: Large-scale synthesis, mechanistic studies, and transport measurements, J. Phys. Chem. B **108**, 8631–8640 (2004)
9.51 E. Lifshitz, M. Bashouti, V. Kloper, A. Kigel, M.S. Eisen, S. Berger: Synthesis and characterization of PbSe quantum wires, multipods, quantum rods, cubes, Nano Lett. **3**, 857–862 (2003)
9.52 W. Lu, P. Gao, W.B. Jian, Z.L. Wang, J. Fang: Perfect orientation ordered in-situ one-dimensional self-assembly of Mn-doped PbSe nanocrystals, J. Am. Chem. Soc. **126**, 14816–14821 (2004)
9.53 F. Favier, E.C. Walter, M.P. Zach, T. Benter, R.M. Penner: Hydrogen sensors and switches from electrodeposited palladium mesowire arrays, Science **293**, 2227–2231 (2001)
9.54 X. Huang, N. Zheng: One-pot, high-yield synthesis of 5-fold twinned Pd nanowires and nanorods, J. Am. Chem. Soc. **131**, 4602–4603 (2009) doi:10.1021/ja9009343
9.55 B. Gates, B. Mayers, B. Cattle, Y. Xia: Synthesis, characterization of uniform nanowires of trigonal selenium, Adv. Funct. Mater. **12**, 219–227 (2002)
9.56 C.A. Huber, T.E. Huber, M. Sadoqi, J.A. Lubin, S. Manalis, C.B. Prater: Nanowire array composites, Science **263**, 800–802 (1994)
9.57 Y. Cui, L.J. Lauhon, M.S. Gudiksen, J. Wang, C.M. Lieber: Diameter-controlled synthesis of single crystal silicon nanowires, Appl. Phys. Lett. **78**, 2214–2216 (2001)
9.58 A.M. Morales, C.M. Lieber: A laser ablation method for the synthesis of crystalline semiconductor nanowires, Science **279**, 208–211 (1998)
9.59 N. Wang, Y.F. Zhang, Y.H. Tang, C.S. Lee, S.T. Lee: SiO_2-enhanced synthesis of Si nanowires by laser ablation, Appl. Phys. Lett. **73**, 3902–3904 (1998)
9.60 M.K. Sunkara, S. Sharma, R. Miranda, G. Lian, E.C. Dickey: Bulk synthesis of silicon nanowires using a low-temperature vapor-liquid-solid method, Appl. Phys. Lett. **79**, 1546–1548 (2001)
9.61 K. Peng, M. Zhang, A. Lu, N.-B. Wong, R. Zhang, S.-T. Lee: Ordered silicon nanowire arrays via nanosphere lithography and metal-induced etching, Appl. Phys. Lett. **90**, 163123 (2007)
9.62 S. Vaddiraju, H. Chandrasekaran, M.K. Sunkara: Vapor phase synthesis of tungsten nanowires, J. Am. Chem. Soc. **125**, 10792–10793 (2003)
9.63 J.P. Heremans, C.M. Thrush, D.T. Morelli, M.-C. Wu: Thermoelectric power of bismuth nanocomposites, Phys. Rev. Lett. **88**, 216801-1–216801-4 (2002)
9.64 Y. Li, G.S. Cheng, L.D. Zhang: Fabrication of highly ordered ZnO nanowire arrays in anodic alumina membranes, J. Mater. Res. **15**, 2305–2308 (2000)
9.65 P. Yang, H. Yan, S. Mao, R. Russo, J. Johnson, R. Saykally, N. Morris, J. Pham, R. He, H.-J. Choi: Controlled growth of ZnO nanowires and their optical properties, Adv. Funct. Mater. **12**, 323–331 (2002)
9.66 M.J. Zheng, L.D. Zhang, G.H. Li, W.Z. Shen: Fabrication and optical properties of large-scale uniform zinc oxide nanowire arrays by one-step electrochemical deposition technique, Chem. Phys. Lett. **363**, 123–128 (2002)

9.67 G.A. Ozin: Nanochemistry: Synthesis in diminishing dimensions, Adv. Mater. **4**, 612–649 (1992)

9.68 R.J. Tonucci, B.L. Justus, A.J. Campillo, C.E. Ford: Nanochannel array glass, Science **258**, 783–785 (1992)

9.69 J.Y. Ying: Nanoporous systems and templates, Sci. Spec. **18**, 56–63 (1999)

9.70 J.W. Diggle, T.C. Downie, C.W. Goulding: Anodic oxide films on aluminum, Chem. Rev. **69**, 365–405 (1969)

9.71 J.P. O'Sullivan, G.C. Wood: The morphology and mechanism of formation of porous anodic films on aluminum, Proc. R. Soc. A **317**, 511–543 (1970)

9.72 A.P. Li, F. Müller, A. Birner, K. Nielsch, U. Gösele: Hexagonal pore arrays with a 50–420 nm interpore distance formed by self-organization in anodic alumina, J. Appl. Phys. **84**, 6023–6026 (1998)

9.73 J.P. Sullivan, G.C. Wood: The morphology, mechanism of formation of porous anodic films on aluminum, Proc. R. Soc. A **317**, 511–543 (1970)

9.74 O. Jessensky, F. Müller, U. Gösele: Self-organized formation of hexagonal pore arrays in anodic alumina, Appl. Phys. Lett. **72**, 1173–1175 (1998)

9.75 Y.-M. Lin, X. Sun, S. Cronin, Z. Zhang, J.Y. Ying, M.S. Dresselhaus: Fabrication, transport properties of Te-doped bismuth nanowire arrays. In: *Molecular Electronics: MRS Symposium Proceedings*, Vol. 582, ed. by S.T. Pantelides, M.A. Reed, J. Murday, A. Aviran (Materials Research Society Press, Pittsburgh 2000), pp. 1–6, Chap. H10.3

9.76 F. Li, L. Zhang, R.M. Metzger: On the growth of highly ordered pores in anodized aluminum oxide, Chem. Mater. **10**, 2470–2480 (1998)

9.77 H. Masuda, M. Satoh: Fabrication of gold nanodot array using anodic porous alumina as an evaporation mask, Jpn. J. Appl. Phys. **35**, L126–L129 (1996)

9.78 H. Masuda, H. Yamada, M. Satoh, H. Asoh, M. Nakao, T. Tamamura: Highly ordered nanochannel-array architecture in anodic alumina, Appl. Phys. Lett. **71**, 2770–2772 (1997)

9.79 W. Lee, R. Ji, C.A. Ross, U. Gösele, K. Nielsch: Wafer-scale Ni imprint stamps for porous alumina membranes based on interference lithography, Small **2**, 978–982 (2006)

9.80 C.R. Martin: Nanomaterials: A membrane-based synthetic approach, Science **266**, 1961–1966 (1994)

9.81 P. Apel: Track etching technique in membrane technology, Radiat. Meas. **34**, 559–566 (2001)

9.82 E. Ferain, R. Legras: Track-etched membrane: Dynamics of pore formation, Nucl. Instrum. Methods B **84**, 331–336 (1993)

9.83 A. Blondel, J.P. Meier, B. Doudin, J.-P. Ansermet: Giant magnetoresistance of nanowires of multilayers, Appl. Phys. Lett. **65**, 3019–3021 (1994)

9.84 K. Liu, C.L. Chien, P.C. Searson, Y.Z. Kui: Structural and magneto-transport properties of electrodeposited bismuth nanowires, Appl. Phys. Lett. **73**, 1436–1438 (1998)

9.85 C.A. Huber, T.E. Huber: A novel microstructure: semiconductor-impregnated porous Vycor glass, J. Appl. Phys. **64**, 6588–6590 (1988)

9.86 J.S. Beck, J.C. Vartuli, W.J. Roth, M.E. Leonowicz, C.T. Kresge, K.D. Schmitt, C.T.-W. Chu, D.H. Olson, E.W. Sheppard, S.B. McCullen, J.B. Higgins, J.L. Schlenker: A new family of mesoporous molecular sieves prepared with liquid crystal templates, J. Am. Chem. Soc. **114**, 10834–10843 (1992)

9.87 C.-G. Wu, T. Bein: Conducting polyaniline filaments in a mesoporous channel host, Science **264**, 1757–1759 (1994)

9.88 T. Thurn-Albrecht, J. Schotter, G.A. Kästle, N. Emley, T. Shibauchi, L. Krusin-Elbaum, K. Guarini, C.T. Black, M.T. Tuominen, T.P. Russell: Ultrahigh-density nanowire arrays grown in self-assembled diblock copolymer templates, Science **290**, 2126–2129 (2000)

9.89 P.-Y. Chen, X. Dang, M.T. Klug, N.M. Dorval Courchesne, J. Qi, M.N. Hyder, A.M. Belcher, P.T. Hammond: M13 virus-enabled synthesis of titanium dioxide nanowires for tunable mesoporous semiconducting networks, Chem. Mater. **27**, 1531–1540 (2015) doi:10.1021/cm503803u

9.90 J.C. Zhou, C.M. Soto, M.-S. Chen, M.A. Bruckman, M.H. Moore, E. Barry, B.R. Ratna, P.E. Pehrsson, B.R. Spies, T.S. Confer: Biotemplating rod-like viruses for the synthesis of copper nanorods and nanowires, J. Nanobiotechnol. **10**, 18 (2012) doi:10.1186/1477-3155-10-18

9.91 M. Knez, M. Sumser, A.M. Bittner, C. Wege, H. Jeske, T.P. Martin, K. Kern: Spatially selective nucleation of metal clusters on the tobacco mosaic virus, Adv. Funct. Mater. **14**, 116–124 (2004) doi:10.1002/adfm.200304376

9.92 X.Z. Fan, E. Pomerantseva, M. Gnerlich, A. Brown, K. Gerasopoulos, M. McCarthy, J. Culver, R. Ghodssi: Tobacco mosaic virus: A biological building block for micro/nano systems, J. Vac. Sci. Technol. A **31**, 050815-1–05081524 (2013)

9.93 Y.-M. Lin, S.B. Cronin, J.Y. Ying, M.S. Dresselhaus, J.P. Heremans: Transport properties of Bi nanowire arrays, Appl. Phys. Lett. **76**, 3944–3946 (2000)

9.94 A.W. Adamson: *Physical Chemistry of Surfaces* (Wiley, New York 1982) p. 338

9.95 R. Ferré, K. Ounadjela, J.M. George, L. Piraux, S. Dubois: Magnetization processes in nickel and cobalt electrodeposited nanowires, Phys. Rev. B **56**, 14066–14075 (1997)

9.96 H. Zeng, M. Zheng, R. Skomski, D.J. Sellmyer, Y. Liu, L. Menon, S. Bandyopadhyay: Magnetic properties of self-assembled Co nanowires of varying length and diameter, J. Appl. Phys. **87**, 4718–4720 (2000)

9.97 Y. Peng, H.L. Zhang, S.-L. Pan, H.-L. Li: Magnetic properties and magnetization reversal of α-Fe nanowires deposited in alumina film, J. Appl. Phys. **87**, 7405–7408 (2000)

9.98 L. Piraux, J.M. George, J.F. Despres, C. Leroy, E. Ferain, R. Legras, K. Ounadjela, A. Fert: Giant magnetoresistance in magnetic multilayered nanowires, Appl. Phys. Lett. **65**, 2484–2486 (1994)

9.99 S. Bhattacharrya, S.K. Saha, D. Chakravorty: Nanowire formation in a polymeric film, Appl. Phys. Lett. **76**, 3896–3898 (2000)

9.100 G. Yi, W. Schwarzacher: Single crystal superconductor nanowires by electrodeposition, Appl. Phys. Lett. **74**, 1746–1748 (1999)

9.101 D. Al-Mawlawi, C.Z. Liu, M. Moskovits: Nanowires formed in anodic oxide nanotemplates, J. Mater. Res. **9**, 1014–1018 (1994)

9.102 Z. Yao, C. Wang, Y. Li, N.-Y. Kim: AAO-assisted synthesis of highly ordered, large-scale TiO_2 nanowire arrays via sputtering and atomic layer deposition, Nanoscale Res. Lett. **10**, 166 (2015) doi:10.1186/s11671-015-0872-9

9.103 J.W. Elam, D. Routkevitch, P.P. Mardilovich, S.M. George: Conformal coating on ultrahigh-aspect-ratio nanopores of anodic alumina by atomic layer deposition, Chem. Mater. **15**, 3507–3517 (2003) doi:10.1021/cm0303080

9.104 M. Daub, M. Knez, U. Goesele, K. Nielsch: Ferromagnetic nanotubes by atomic layer deposition in anodic alumina membranes, J. Appl. Phys. **101**, 09J111 (2007) doi:10.1063/1.2712057

9.105 R.S. Wagner, W.C. Ellis: Vapor-liquid-solid mechanism of single crystal growth, Appl. Phys. Lett. **4**, 89–90 (1964)

9.106 Y. Wu, P. Yang: Direct observation of vapor-liquid-solid nanowire growth, J. Am. Chem. Soc. **123**, 3165–3166 (2001)

9.107 Y. Wu, R. Fan, P. Yang: Block-by-block growth of single-crystalline Si/SiGe superlattice nanowires, Nano Lett. **2**, 83–86 (2002)

9.108 S. Sharma, M.K. Sunkara, R. Miranda, G. Lian, E.C. Dickey: A novel low temperature synthesis method for semiconductor nanowires. In: *Synthesis, Functional Properties and Applications of Nanostructures, Mater. Res. Soc. Symp. Proc., San Francisco*, Vol. 676, ed. by H.W. Hahn, D.L. Feldheim, C.P. Kubiak, R. Tannenbaum, R.W. Siegel (Materials Research Society, Pittsburgh 2001) p. Y1.6

9.109 J. Johansson, B.A. Wacaser, K.A. Dick, W. Seifert: Growth related aspects of epitaxial nanowires, Nanotechnology **17**, S355–S361 (2006) doi:10.1088/0957-4484/17/11/S21

9.110 M.H. Huang, S. Mao, H. Feick, H. Yan, Y. Wu, H. Kind, E. Weber, R. Russo, P. Yang: Room-temperature ultraviolet nanowire nanolasers, Science **292**, 1897–1899 (2001)

9.111 M.S. Gudiksen, L.J. Lauhon, J. Wang, D.C. Smith, C.M. Lieber: Growth of nanowire superlattice structures for nanoscale photonics and electronics, Nature **415**, 617–620 (2002)

9.112 Y. Wu, J. Xiang, C. Yang, W. Lu, C.M. Lieber: Single-crystal metallic nanowires and metal/semiconductor nanowire heterostructures, Nature **430**, 61–65 (2004)

9.113 M.T. Björk, B.J. Ohlsson, T. Sass, A.I. Persson, C. Thelander, M.H. Magnusson, K. Deppert, L.R. Wallenberg, L. Samuelson: One-dimensional steeplechase for electrons realized, Nano Lett. **2**, 87–89 (2002)

9.114 N. Wang, Y.H. Tang, Y.F. Zhang, C.S. Lee, S.T. Lee: Nucleation and growth of Si nanowires from silicon oxide, Phys. Rev. B **58**, R16024–R16026 (1998)

9.115 Y.F. Zhang, Y.H. Tang, N. Wang, C.S. Lee, I. Bello, S.T. Lee: One-dimensional growth mechanism of crystalline silicon nanowires, J. Cryst. Growth **197**, 136–140 (1999)

9.116 S.T. Lee, Y.F. Zhang, N. Wang, Y.H. Tang, I. Bello, C.S. Lee, Y.W. Chung: Semiconductor nanowires from oxides, J. Mater. Res. **14**, 4503–4507 (1999)

9.117 D.D.D. Ma, C.S. Lee, Y. Lifshitz, S.T. Lee: Periodic array of intramolecular junctions of silicon nanowires, Appl. Phys. Lett. **81**, 3233–3235 (2002)

9.118 S.V. Thombare, A.F. Marshall, P.C. McIntyre: Kinetics of germanium nanowire growth by the vapor-solid-solid mechanism with a Ni-based catalyst, APL Mater. **1**, 061101 (2013) doi:10.1063/1.4833935

9.119 J. Lensch-Falk, E. Hemesath, D. Perea, L. Lauhon: Alternative catalysts for VSS growth of silicon and germanium nanowires, J. Mater. Chem. **19**, 849–857 (2009) doi:10.1039/b817391e

9.120 F. Wang, A. Dong, J. Sun, R. Tang, H. Yu, W.E. Buhro: Solution-liquid-solid growth of semiconductor nanowires, Inorganic Chem. **45**, 7511–7521 (2006)

9.121 H. Jansen, M. de Boer, R. Legtenberg, M. Elwenspoek: The black silicon method: A universal method for determining the parameter setting of a fluorine-based reactive ion etcher in deep silicon trench etching with profile control, J. Micromech. Microeng. **5**, 115–120 (1995)

9.122 Y.Q. Fu, A. Colli, A. Fasoli, J.K. Luo, A.J. Flewitt, A.C. Ferrari, W.I. Milne: Deep reactive ion etching as a tool for nanostructure fabrication, J. Vac. Sci. Technol. B **27**, 1520–1526 (2009)

9.123 X. Liu, P.R. Coxon, M. Peters, B. Hoex, J.M. Cole, D.J. Fray: Black silicon: Fabrication methods, properties and solar energy applications, Energy Environ. Sci. **7**, 3223–3263 (2014)

9.124 F. Toor, J.B. Miller, L.M. Davidson, L. Nichols, W. Duan, M.P. Jura, J. Yim, J. Forziati, M.R. Black: Nanostructured silicon via metal assisted catalyzed etch (MACE): Chemistry fundamentals and pattern engineering, Nanotechnology **27**(41), 412003 (2016)

9.125 Z. Huang, N. Geyer, P. Werner, J. de Boor, U. Gösele: Metal-assisted chemical etching of silicon: A review, Adv. Mater. **23**, 285–308 (2011)

9.126 B. Gates, Y. Yin, Y. Xia: A solution-phase approach to the synthesis of uniform nanowires of crystalline selenium with lateral dimensions in the range of 10–30 nm, J. Am. Chem. Soc. **122**, 12582–12583 (2000)

9.127 B. Mayers, B. Gates, Y. Yin, Y. Xia: Large-scale synthesis of monodisperse nanorods of Se/Te alloys through a homogeneous nucleation and solution growth process, Adv. Mater. **13**, 1380–1384 (2001)

9.128 B. Gates, Y. Wu, Y. Yin, P. Yang, Y. Xia: Single-crystalline nanowires of Ag_2Se can be synthesized by templating against nanowires of trigonal Se, J. Am. Chem. Soc. **123**, 11500–11501 (2001)

9.129 B. Gates, B. Mayers, Y. Wu, Y. Sun, B. Cattle, P. Yang, Y. Xia: Synthesis and characterization of crystalline Ag_2Se nanowires through a template-engaged reaction at room temperature, Adv. Funct. Mater. **12**, 679–686 (2002)

9.130 H. Yu, P.C. Gibbons, W.E. Buhro: Bismuth, tellurium and bismuth telluride nanowires, J. Mater. Chem. **14**, 595–602 (2004)

9.131 X. Peng, J. Wickham, A.P. Alivisatos: Kinetics of II–VI, III–V colloidal semiconductor nanocrystal growth: 'Focusing' of size distributions, J. Am. Chem. Soc. **120**, 5343–5344 (1998)

9.132 M.P. Zach, K. Inazu, K.H. Ng, J.C. Hemminger, R.M. Penner: Synthesis of molybdenum nanowires with millimeter-scale lengths using electrochemical step edge decoration, Chem. Mater. **14**, 3206–3216 (2002)

9.133 Dedi, P.-C. Lee, C.-H. Chien, G.-P. Dong, W.-C. Huang, C.-L. Chen, C.-M. Tseng, S.R. Harutyunyan, C.-H. Lee, Y.-Y. Chen: Stress-induced growth of single-crystalline lead telluride nanowires and their thermoelectric transport properties, Appl. Phys. Lett. **103**, 023115 (2013) doi:10.1063/1.4813606

9.134 J. Ham, W. Shim, D.H. Kim, S. Lee, J. Roh, S.W. Sohn, K.H. Oh, P.W. Voorhees, W. Lee: Direct growth of compound semiconductor nanowires by on-film formation of nanowires: Bismuth telluride, Nano Lett. **9**, 2867–2872 (2009) doi:10.1021/nl9010518

9.135 N.A. Melosh, A. Boukai, F. Diana, B. Gerardot, A. Badolto, P.M. Petroff, J.R. Heath: Ultrahigh-density nanowire lattices and circuits, Science **300**, 112–115 (2003)

9.136 P. Yang, F. Kim: Langmuir–Blodgett assembly of one-dimensional nanostructures, ChemPhysChem **3**, 503–506 (2002)

9.137 B. Messer, J.H. Song, P. Yang: Microchannel networks for nanowire patterning, J. Am. Chem. Soc. **122**, 10232–10233 (2000)

9.138 P.A. Smith, C.D. Nordquist, T.N. Jackson, T.S. Mayer, B.R. Martin, J. Mbindyo, T.E. Mallouk: Electric-field assisted assembly and alignment of metallic nanowires, Appl. Phys. Lett. **77**, 1399–1401 (2000)

9.139 D. Whang, S. Jin, C.M. Lieber: Large-scale hierarchical organization of nanowires for functional nanosystems, Jpn. J. Appl. Phys. **43**, 4465–4470 (2004)

9.140 S. Jin, D.M. Whang, M.C. McAlpine, R.S. Friedman, Y. Wu, C.M. Lieber: Scalable interconnection and integration of nanowire devices without registration, Nano Lett. **4**, 915–919 (2004)

9.141 M. Li, R.B. Bhiladvala, T.J. Morrow, J.A. Sioss, K.-K. Lew, J.M. Redwing, C.D. Keating, T.S. Mayer: Bottom-up assembly of large-area nanowire resonator arrays, Nat. Nanotechnol. **3**, 88–92 (2008)

9.142 S. Evoy, N. DiLello, V. Deshpande, A. Narayanan, H. Liu, M. Riegelman, B.R. Martin, B. Hailer, J.-C. Bradley, W. Weiss, T.S. Mayer, Y. Gogotsi, H.H. Bau, T.E. Mallouk, S. Raman: Dielectrophoretic assembly and integration of nanowire devices with functional CMOS operating circuitry, Microelectron. Eng. **75**, 31–42 (2004)

9.143 T. Kuykendall, P.J. Pauzauskie, Y.F. Zhang, J. Goldberger, D. Sirbuly, J. Denlinger, P.D. Yang: Crystallographic alignment of high-density gallium nitride nanowire arrays, Nat. Mater. **3**, 524–528 (2004)

9.144 O. Rabin, P.R. Herz, S.B. Cronin, Y.-M. Lin, A.I. Akinwande, M.S. Dresselhaus: Nanofabrication using self-assembled alumina templates. In: *Nonlithographic and Lithographic Methods for Nanofabrication, Mater. Res. Soc. Symp. Proc., Boston*, Vol. 636, ed. by J.A. Rogers, A. Karim, L. Merhari, D. Norris, Y. Xia (Materials Research Society, Pittsburgh 2001) pp. D4.7-1–D4.7-6

9.145 O. Rabin, P.R. Herz, Y.-M. Lin, A.I. Akinwande, S.B. Cronin, M.S. Dresselhaus: Formation of thick porous anodic alumina films and nanowire arrays on silicon wafers and glass, Adv. Funct. Mater. **13**, 631–638 (2003)

9.146 O. Rabin, P.R. Herz, Y.-M. Lin, S.B. Cronin, A.I. Akinwande, M.S. Dresselhaus: Arrays of nanowires on silicon wafers. In: *21st Int. Conf. Thermoelectr. Proc. ICT '02 Long Beach* (IEEE, Piscataway 2002) pp. 276–279

9.147 Y.H. Tang, Y.F. Zhang, N. Wang, C.S. Lee, X.D. Han, I. Bello, S.T. Lee: Morphology of Si nanowires synthesized by high-temperature laser ablation, J. Appl. Phys. **85**, 7981–7983 (1999)

9.148 Y. Ding, Z.L. Wang: Structure analysis of nanowires and nanobelts by transmission electron microscopy, J. Phys. Chem. B **108**, 12280–12291 (2004)

9.149 S.B. Cronin, Y.-M. Lin, O. Rabin, M.R. Black, G. Dresselhaus, M.S. Dresselhaus, P.L. Gai: Bismuth nanowires for potential applications in nanoscale electronics technology, Microsc. Microanal. **8**, 58–63 (2002)

9.150 M.S. Sander, R. Gronsky, Y.-M. Lin, M.S. Dresselhaus: Plasmon excitation modes in nanowire arrays, J. Appl. Phys. **89**, 2733–2736 (2001)

9.151 L.J. Lauhon, M.S. Gudiksen, D. Wang, C.M. Lieber: Epitaxial core-shell and core-multishell nanowire heterostructures, Nature **420**, 57–61 (2002)

9.152 L. Venkataraman, C.M. Lieber: Molybdenum selenide molecular wires as one-dimensional conductors, Phys. Rev. Lett. **83**, 5334–5337 (1999)

9.153 A. Majumdar: Scanning thermal microscopy, Annu. Rev. Mater. Sci. **29**, 505–585 (1999)

9.154 K.M. Unruh, T.E. Huber, C.A. Huber: Melting and freezing behavior of indium metal in porous glasses, Phys. Rev. B **48**, 9021–9027 (1993)

9.155 Y.Y. Wu, P.D. Yang: Melting and welding semiconductor nanowires in nanotubes, Adv. Mater. **13**, 520–523 (2001)

9.156 P.M. Ajayan, S. Iijima: Capillarity-induced filling of carbon nanotubes, Nature **361**, 333–334 (1993)

9.157 Y. Gao, Y. Bando: Carbon nanothermometer containing gallium, Nature **415**, 599 (2002)

9.158 M.E. Toimil-Molares, A.G. Balogh, T.W. Cornelius, R. Neumann, C. Trautmann: Fragmentation of nanowires driven by Rayleigh instability, Appl. Phys. Lett. **84**, 5337–5339 (2004)

9.159 J.L. Costa-Krämer, N. Garcia, H. Olin: Conductance quantization histograms of gold nanowires at 4 K, Phys. Rev. B **55**, 12910–12913 (1997)

9.160 D.A. Wharam, T.J. Thornton, R. Newbury, M. Pepper, H. Ahmed, J.E.F. Frost, D.G. Hasko, D.C. Peacock, D.A. Ritchie, G.A.C. Jones: One-dimensional transport and the quantization of the ballistic resistance, J. Phys. C **21**, L209–L214 (1988)

9.161 B.J. van Wees, H. van Houten, C.W.J. Beenakker, J.G. Williamson, L.P. Kouvenhoven, D. van der Marel, C.T. Foxon: Quantized conductance of point contacts in a two-dimensional electron gas, Phys.

Rev. Lett. **60**, 848–850 (1988)
9.162 C.J. Muller, J.M. van Ruitenbeek, L.J. de Jongh: Conductance and supercurrent discontinuities in atomic-scale metallic constrictions of variable width, Phys. Rev. Lett. **69**, 140–143 (1992)
9.163 C.J. Muller, J.M. Krans, T.N. Todorov, M.A. Reed: Quantization effects in the conductance of metallic contacts at room temperature, Phys. Rev. B **53**, 1022–1025 (1996)
9.164 J.L. Costa-Krämer, N. Garcia, H. Olin: Conductance quantization in bismuth nanowires at 4 K, Phys. Rev. Lett. **78**, 4990–4993 (1997)
9.165 C.Z. Li, H.X. He, A. Bogozi, J.S. Bunch, N.J. Tao: Molecular detection based on conductance quantization of nanowires, Appl. Phys. Lett. **76**, 1333–1335 (2000)
9.166 J.L. Costa-Krämer, N. Garcia, P. Garcia-Mochales, P.A. Serena, M.I. Marques, A. Correia: Conductance quantization in nanowires formed between micro and macroscopic metallic electrodes, Phys. Rev. B **55**, 5416–5424 (1997)
9.167 Y. Huang, X. Duan, Y. Cui, L.J. Lauhon, K.-H. Kim, C.M. Lieber: Logic gates and computation from assembled nanowire building blocks, Science **294**, 1313–1317 (2001)
9.168 J.-R. Kim, H. Oh, H.M. So, J.-J. Kim, J. Kim, C.J. Lee, S.C. Lyu: Schottky diodes based on a single GaN nanowire, Nanotechnology **13**, 701–704 (2002)
9.169 X. Duan, Y. Huang, C.M. Lieber: Nonvolatile memory and programmable logic from molecule-gated nanowires, Nano Lett. **2**, 487–490 (2002)
9.170 E.C. Walter, R.M. Penner, H. Liu, K.H. Ng, M.P. Zach, F. Favier: Sensors from electrodeposited metal nanowires, Surf. Interface Anal. **34**, 409–412 (2002)
9.171 E.C. Walter, K.H. Ng, M.P. Zach, R.M. Penner, F. Favier: Electronic devices from electrodeposited metal nanowires, Microelectron. Eng. **61/62**, 555–561 (2002)
9.172 Y.-M. Lin, X. Sun, M.S. Dresselhaus: Theoretical investigation of thermoelectric transport properties of cylindrical Bi nanowires, Phys. Rev. B **62**, 4610–4623 (2000)
9.173 K. Liu, C.L. Chien, P.C. Searson: Finite-size effects in bismuth nanowires, Phys. Rev. B **58**, R14681–R14684 (1998)
9.174 Z. Zhang, X. Sun, M.S. Dresselhaus, J.Y. Ying, J. Heremans: Magnetotransport investigations of ultrafine single-crystalline bismuth nanowire arrays, Appl. Phys. Lett. **73**, 1589–1591 (1998)
9.175 J. Heremans, C.M. Thrush, Z. Zhang, X. Sun, M.S. Dresselhaus, J.Y. Ying, D.T. Morelli: Magnetoresistance of bismuth nanowire arrays: A possible transition from one-dimensional to three-dimensional localization, Phys. Rev. B **58**, R10091–R10095 (1998)
9.176 L. Sun, P.C. Searson, C.L. Chien: Finite-size effects in nickel nanowire arrays, Phys. Rev. B **61**, R6463–R6466 (2000)
9.177 Y.-M. Lin, S.B. Cronin, O. Rabin, J.Y. Ying, M.S. Dresselhaus: Transport properties and observation of semimetal-semiconductor transition in Bi-based nanowires. In: *Quantum Confined Semiconductor Nanostructures: MRS Symposium Proceedings, Boston*, Vol. 737-C, ed. by J.M. Buriak, D.D.M. Wayner, F. Priolo, B. White, V. Klimov, L. Tsybeskov (Materials Research Society, Pittsburgh 2003) p. F3.14
9.178 Y.-M. Lin, M.S. Dresselhaus: Transport properties of superlattice nanowires and their potential for thermoelectric applications. In: *Quantum Confined Semiconductor Nanostructures: MRS Symposium Proceedings, Boston*, Vol. 737-C, ed. by J.M. Buriak, D.D.M. Wayner, F. Priolo, B. White, V. Klimov, L. Tsybeskov (Materials Research Society Press, Pittsburgh 2003) p. F8.18
9.179 Y.-M. Lin, O. Rabin, S.B. Cronin, J.Y. Ying, M.S. Dresselhaus: Semimetal-semiconductor transition in $Bi_{1-x}Sb_x$ alloy nanowires and their thermoelectric properties, Appl. Phys. Lett. **81**, 2403–2405 (2002)
9.180 J. Heremans, C.M. Thrush, Y.-M. Lin, S.B. Cronin, M.S. Dresselhaus: Transport properties of antimony nanowires, Phys. Rev. B **63**, 085406-1–085406-8 (2001)
9.181 Y.-M. Lin, S.B. Cronin, O. Rabin, J.Y. Ying, M.S. Dresselhaus: Transport properties of $Bi_{1-x}Sb_x$ alloy nanowires synthesized by pressure injection, Appl. Phys. Lett. **79**, 677–679 (2001)
9.182 D.E. Beutler, N. Giordano: Localization and electron-electron interaction effects in thin Bi wires and films, Phys. Rev. B **38**, 8–19 (1988)
9.183 Z. Zhang, X. Sun, M.S. Dresselhaus, J.Y. Ying, J. Heremans: Electronic transport properties of single crystal bismuth nanowire arrays, Phys. Rev. B **61**, 4850–4861 (2000)
9.184 J. Heremans, C.M. Thrush: Thermoelectric power of bismuth nanowires, Phys. Rev. B **59**, 12579–12583 (1999)
9.185 D. Li, S.T. Huxtable, A.R. Abramson, A. Majumdar: Thermal transport in nanostructured solid-state cooling devices, J. Heat Transfer **127**, 108–114 (2005) doi:10.1115/1.1839588
9.186 D. Li, Y. Wu, P. Kim, L. Shi, P. Yang, A. Majumdar: Thermal conductivity of individual silicon nanowires, Appl. Phys. Lett. **83**, 2934–2936 (2003)
9.187 A.I. Boukai, Y. Bunimovich, J. Tahir-Kheli, J.-K. Yu, W.A. Goddard III, J.R. Heath: Silicon nanowires as efficient thermoelectric materials, Nature **451**, 168–171 (2008) doi:10.1038/nature06458
9.188 A.I. Hochbaum, R. Chen, R.D. Delgado, W. Liang, E.C. Garnett, M. Najarian, A. Majumdar, P. Yang: Enhanced thermoelectric performance of rough silicon nanowires, Nature **451**, 163–167 (2008) doi:10.1038/nature06381
9.189 D. Li, Y. Wu, R. Fan, P. Yang, A. Majumdar: Thermal conductivity of Si/SiGe superlattice nanowires, Appl. Phys. Lett. **83**, 3186–3188 (2003)
9.190 S.C. Andrews, M.A. Fardy, M.C. Moore, S. Aloni, M. Zhang, V. Radmilovic, P. Yang: Atomic-level control of the thermoelectric properties in polytypoid nanowires, Chem. Sci. **2**, 706–714 (2011) doi:10.1039/C0SC00537A
9.191 F. Zhou, A.L. Moore, M.T. Pettes, Y. Lee, J.H. Seol, Q.L. Ye, L. Rabenberg, L. Shi: Effect of growth base pressure on the thermoelectric properties of

indium antimonide nanowires, J. Phys. D Appl. Phys. **43**, 025406 (2010) doi:10.1088/0022-3727/43/2/025406
9.192 T.S. Tighe, J.M. Worlock, M.L. Roukes: Direct thermal conductance measurements on suspended monocrystalline nanostructures, Appl. Phys. Lett. **70**, 2687–2689 (1997)
9.193 S.T. Huxtable, A.R. Abramson, C.-L. Tien, A. Majumdar, C. LaBounty, X. Fan, G. Zeng, J.E. Bowers, A. Shakouri, E.T. Croke: Thermal conductivity of Si/SiGe and SiGe/SiGe superlattices, Appl. Phys. Lett. **80**, 1737–1739 (2002)
9.194 L. Shi, C. Yu, J. Zhou: Thermal characterization and sensor applications of one-dimensional nanostructures employing microelectromechanical systems, J. Phys. Chem. B **109**, 22102–22111 (2005)
9.195 R. Venkatasubramanian, E. Siivola, T. Colpitts, B. O'Quinn: Thin-film thermoelectric devices with high room-temperature figures of merit, Nature **413**, 597–602 (2001)
9.196 C. Dames, G. Chen: Theoretical phonon thermal conductivity of Si-Ge superlattice nanowires, J. Appl. Phys. **95**, 682–693 (2004)
9.197 C. Dames, G. Chen: Modeling the thermal conductivity of a SiGe segmented nanowire. In: *21st Int. Conf. Thermoelectr. Proc. ICT '02, Long Beach* (IEEE, Piscataway 2002) pp. 317–320
9.198 N. Mingo, L. Yang, D. Li, A. Majumdar: Predicting the thermal conductivity of Si and Ge nanowires, Nano Lett. **3**, 1713–1716 (2003) doi:10.1021/nl034721i
9.199 G. Chen, M.S. Dresselhaus, G. Dresselhaus, J.-P. Fleurial, T. Caillat: Recent developments in thermoelectric materials, Int. Mater. Rev. **48**, 45–66 (2003)
9.200 M. Kazan, G. Guisbiers, S. Pereira, M.R. Correia, P. Masri, A. Bruyant, S. Volz, P. Royer: Thermal conductivity of silicon bulk and nanowires: Effects of isotopic composition, phonon confinement, and surface roughness, J. Appl. Phys. **107**, 083503 (2010) doi:10.1063/1.3340973
9.201 K. Schwab, J.L. Arlett, J.M. Worlock, M.L. Roukes: Thermal conductance through discrete quantum channels, Physica E **9**, 60–68 (2001)
9.202 K. Schwab, E.A. Henriksen, J.M. Worlock, M.L. Roukes: Measurement of the quantum of thermal conductance, Nature **404**, 974–977 (2000)
9.203 L.D. Hicks, M.S. Dresselhaus: Thermoelectric figure of merit of a one-dimensional conductor, Phys. Rev. B **47**, 16631–16634 (1993)
9.204 O. Rabin, Y.-M. Lin, M.S. Dresselhaus: Anomalously high thermoelectric figure of merit in $Bi_{1-x}Sb_x$ nanowires by carrier pocket alignment, Appl. Phys. Lett. **79**, 81–83 (2001)
9.205 Y.M. Zuev, J.S. Lee, C. Galloy, H. Park, P. Kim: Diameter dependence of the transport properties of antimony telluride nanowires, Nano Lett. **10**, 3037–3040 (2010)
9.206 W. Liang, A.I. Hochbaum, M. Fardy, O. Rabin, M. Zhang, P. Yang: Field-effect modulation of Seebeck coefficient in single PbSe nanowires, Nano Lett. **9**, 1689–1693 (2009)
9.207 Y. Tian, M.R. Sakr, J.M. Kinder, D. Liang, M.J. MacDonald, R.L.J. Qiu, H.-J. Gao, X.P.A. Gao: One-dimensional quantum confinement effect modulated thermoelectric properties in InAs nanowires, Nano Lett. **12**, 6492–6497 (2012)
9.208 P.M. Wu, J. Gooth, X. Zianni, S.F. Svensson, J.G. Gluschke, K.A. Dick, C. Thelander, K. Nielsch, H. Linke: Large thermoelectric power factor enhancement observed in InAs nanowires, Nano Lett. **13**, 4080–4086 (2013)
9.209 J.E. Cornett, O. Rabin: Thermoelectric figure of merit calculations for semiconducting nanowires, Appl. Phys. Lett. **98**, 182104 (2011)
9.210 J.E. Cornett, O. Rabin: Universal scaling relations for the thermoelectric power factor of semiconducting nanostructures, Phys. Rev. B **84**, 205410 (2011)
9.211 Y. Pei, X. Shi, A. LaLonde, H. Wang, L. Chen, G.J. Snyder: Convergence of electronic bands for high performance bulk thermoelectrics, Nature **473**, 66–69 (2011)
9.212 J. Tang, H. Wang, D.H. Lee, M. Fardy, Z. Huo, T.P. Russell, P. Yang: Holey silicon as an efficient thermoelectric material, Nano Lett. **10**, 4279–4283 (2010)
9.213 L.D. Hicks, M.S. Dresselhaus: The effect of quantum well structures on the thermoelectric figure of merit, Phys. Rev. B **47**, 12727–12731 (1993)
9.214 T.C. Harman, P.J. Taylor, M.P. Walsh, B.E. LaForge: Quantum dot superlattice thermoelectric materials and devices, Science **297**, 2229–2232 (2002)
9.215 Y.-M. Lin, M.S. Dresselhaus: Thermoelectric properties of superlattice nanowires, Phys. Rev. B **68**, 075304 (2003)
9.216 S.R. Nicewarner-Peña, R.G. Freeman, B.D. Reiss, L. He, D.J. Peña, I.D. Walton, R. Cromer, C.D. Keating, M.J. Natan: Submicrometer metallic barcodes, Science **294**, 137–141 (2001)
9.217 M.T. Björk, B.J. Ohlsson, C. Thelander, A.I. Persson, K. Deppert, L.R. Wallenberg, L. Samuelson: Nanowire resonant tunneling diodes, Appl. Phys. Lett. **81**, 4458–4460 (2002)
9.218 M. Cardona: *Light Scattering in Solids* (Springer, Berlin, Heidelberg 1982)
9.219 P.Y. Yu, M. Cardona: *Fundamentals of Semiconductors* (Springer, Berlin, Heidelberg 1995), Chap. 7
9.220 J.C.M. Garnett: Colours in metal glasses, in metallic films, and in metallic solutions, Philos. Trans. R. Soc. A **205**, 237–288 (1906)
9.221 D.E. Aspnes: Optical properties of thin films, Thin Solid Films **89**, 249–262 (1982)
9.222 U. Kreibig, L. Genzel: Optical absorption of small metallic particles, Surf. Sci. **156**, 678–700 (1985)
9.223 M.R. Black, Y.-M. Lin, S.B. Cronin, O. Rabin, M.S. Dresselhaus: Infrared absorption in bismuth nanowires resulting from quantum confinement, Phys. Rev. B **65**, 195417–1–195417–9 (2002)
9.224 Veselago 1967 Usp. Fiz. Nauk 92 517
9.225 A. Poddubny, I. Iorsh, P. Belov, Y. Kivshar: Hyperbolic metamaterials, Nat. Photonics **7**, 948–957 (2013)
9.226 J. Yao, Z. Liu, Y. Liu, Y. Wang, C. Sun, G. Bartal, A.M. Stacy, X. Zhang: Optical negative refraction

in bulk metamaterials of nanowires, Science **321**, 930–930 (2008)
9.227 M.W. Lee, H.Z. Twu, C.-C. Chen, C.H. Chen: Optical characterization of wurtzite gallium nitride nanowires, Appl. Phys. Lett. **79**, 3693–3695 (2001)
9.228 M.S. Gudiksen, J. Wang, C.M. Lieber: Size-depent photoluminescence from single indium phosphide nanowires, J. Phys. Chem. B **106**, 4036–4039 (2002)
9.229 D.M. Lyons, K.M. Ryan, M.A. Morris, J.D. Holmes: Tailoring the optical properties of silicon nanowire arrays through strain, Nano Lett. **2**, 811–816 (2002)
9.230 S. Bhattacharya, D. Banerjee, K.W. Adu, S. Samui, S. Bhattacharyya: Confinement in silicon nanowires: Optical properties, Appl. Phys. Lett. **85**, 2008–2010 (2004) doi:10.1063/1.1787164
9.231 J.C. Johnson, H. Yan, R.D. Schaller, L.H. Haber, R.J. Saykally, P. Yang: Single nanowire lasers, J. Phys. Chem. B **105**, 11387–11390 (2001)
9.232 S. Blom, L.Y. Gorelik, M. Jonson, R.I. Shekhter, A.G. Scherbakov, E.N. Bogachek, U. Landman: Magneto-optics of electronic transport in nanowires, Phys. Rev. B **58**, 16305–16314 (1998)
9.233 J.P. Pierce, E.W. Plummer, J. Shen: Ferromagnetism in cobalt-iron alloy nanowire arrays on w(110), Appl. Phys. Lett. **81**, 1890–1892 (2002)
9.234 S. Melle, J.L. Menendez, G. Armelles, D. Navas, M. Vazquez, K. Nielsch, R.B. Wehrsphon, U. Gösele: Magneto-optical properties of nickel nanowire arrays, Appl. Phys. Lett. **83**, 4547–4549 (2003)
9.235 J.C. Johnson, H. Yan, R.D. Schaller, P.B. Petersen, P. Yang, R.J. Saykally: Near-field imaging of nonlinear optical mixing in single zinc oxide nanowires, Nano Lett. **2**, 279–283 (2002)
9.236 M.R. Black, P.L. Hagelstein, S.B. Cronin, Y.-M. Lin, M.S. Dresselhaus: Optical absorption from an indirect transition in bismuth nanowires, Phys. Rev. B **68**, 235417 (2003)
9.237 M.R. Black, Y.-M. Lin, S.B. Cronin, M.S. Dresselhaus: Using optical measurements to improve electronic models of bismuth nanowires. In: *21st Int. Conf. Thermoelectr. Proc. ICT '02, Long Beach*, ed. by T. Caillat, J. Snyder (IEEE, Piscataway 2002) pp. 253–256
9.238 H. Richter, Z.P. Wang, L. Ley: The one phonon Raman-spectrum in microcrystalline silicon, Solid State Commun. **39**, 625–629 (1981)
9.239 I.H. Campbell, P.M. Fauchet: The effects of microcrystal size and shape on the one phonon Raman-spectra of crystalline semiconductors, Solid State Commun. **58**, 739–741 (1986)
9.240 H.-L. Liu, C.-C. Chen, C.-T. Chia, C.-C. Yeh, C.-H. Chen, M.-Y. Yu, S. Keller, S.P. DenBaars: Infrared and Raman-scattering studies in single-crystalline GaN nanowires, Chem. Phys. Lett. **345**, 245–251 (2001)
9.241 R. Gupta, Q. Xiong, C.K. Adu, U.J. Kim, P.C. Eklund: Laser-induced Fano resonance scattering in silicon nanowires, Nano Lett. **3**, 627–631 (2003)
9.242 X. Duan, Y. Huang, Y. Cui, J. Wang, C.M. Lieber: Indium phosphide nanowires as building blocks for nanoscale electronic and optoelectronic devices, Nature **409**, 66–69 (2001)
9.243 Y. Cui, C.M. Lieber: Functional nanoscale electronic devices assembled using silicon nanowire building blocks, Science **291**, 851–853 (2001)
9.244 Y. Cui, X. Duan, J. Hu, C.M. Lieber: Doping and electrical transport in silicon nanowires, J. Phys. Chem. B **104**, 101–104 (2000)
9.245 G.F. Zheng, W. Lu, S. Jin, C.M. Lieber: Synthesis and fabrication of high-performance n-type silicon nanowire transistors, Adv. Mater. **16**, 1890–1891 (2004)
9.246 J. Goldberger, D.J. Sirbuly, M. Law, P. Yang: ZnO nanowire transistors, J. Phys. Chem. B **109**, 9–14 (2005)
9.247 D.H. Kang, J.H. Ko, E. Bae, J. Hyun, W.J. Park, B.K. Kim, J.J. Kim, C.J. Lee: Ambient air effects on electrical characteristics of gap nanowire transistors, J. Appl. Phys. **96**, 7574–7577 (2004)
9.248 S.-W. Chung, J.-Y. Yu, J.R. Heath: Silicon nanowire devices, Appl. Phys. Lett. **76**, 2068–2070 (2000)
9.249 C. Li, W. Fan, B. Lei, D. Zhang, S. Han, T. Tang, X. Liu, Z. Liu, S. Asano, M. Meyyappan, J. Han, C. Zhou: Multilevel memory based on molecular devices, Appl. Phys. Lett. **84**, 1949–1951 (2004)
9.250 B. Lei, C. Li, D.Q. Zhang, Q.F. Zhou, K. Shung, C.W. Zhou: Nanowire transistors with ferroelectric gate dielectrics: Enhanced performance and memory effects, Appl. Phys. Lett. **84**, 4553–4555 (2004)
9.251 H.T. Ng, J. Han, T. Yamada, P. Nguyen, Y.P. Chen, M. Meyyappan: Single crystal nanowire vertical surround-gate field-effect transistor, Nano Lett. **4**, 1247–1252 (2004)
9.252 J.-P. Colinge, C.-W. Lee, A. Afzalian, N.D. Akhavan, R. Yan, I. Ferain, P. Razavi, B. O'Neill, A. Blake, M. White, A.-M. Kelleher, B. McCarthy, R. Murphy: Nanowire transistors without junctions, Nat. Nanotechnol. **5**, 225–229 (2010) doi:10.1038/nnano.2010.15
9.253 J.P. Colinge, A. Kranti, R. Yan, C.W. Lee, I. Ferain, R. Yu, A.N. Dehdashti, P. Razavi: Junctionless nanowire transistor (JNT): Properties and design guidelines, Solid-State Electron. **65/66**, 33–37 (2011) doi:10.1016/j.sse.2011.06.004
9.254 W. Wu, X. Wen, Z.L. Wang: Taxel-addressable matrix of vertical-nanowire piezotronic transistors for active and adaptive tactile imaging, Science **340**, 952–957 (2013)
9.255 M. Ding, H. Kim, A.I. Akinwande: Observation of valence band electron emission from n-type silicon field emitter arrays, Appl. Phys. Lett. **75**, 823–825 (1999)
9.256 F.-H. Chu, C.-W. Huang, C.-L. Hsin, C.-W. Wang, S.-Y. Yu, P.-H. Yeh, W.-W. Wu: Well-aligned ZnO nanowires with excellent field emission and photocatalytic properties, Nanoscale **4**, 1471–1475 (2012)
9.257 F.C.K. Au, K.W. Wong, Y.H. Tang, Y.F. Zhang, I. Bello, S.T. Lee: Electron field emission from silicon nanowires, Appl. Phys. Lett. **75**, 1700–1702 (1999)
9.258 P.M. Ajayan, O.Z. Zhou: Applications of carbon nanotubes. In: *Carbon Nanotubes: Synthesis, Structure, Properties and Applications*, Springer Ser. Top. Appl. Phys., Vol. 80, ed. by M.S. Dresselhaus, G. Dresselhaus, P. Avouris (Springer, Berlin, Heidel-

berg 2001) pp. 391–425
9.259 M. Lu, M.K. Li, Z.J. Zhang, H.L. Li: Synthesis of carbon nanotubes/si nanowires core-sheath structure arrays and their field emission properties, Appl. Surf. Sci. **218**, 196–202 (2003)
9.260 L. Vila, P. Vincent, L. Dauginet-DePra, G. Pirio, E. Minoux, L. Gangloff, S. Demoustier-Champagne, N. Sarazin, E. Ferain, R. Legras, L. Piraux, P. Legagneux: Growth and field-emission properties of vertically aligned cobalt nanowire arrays, Nano Lett. **4**, 521–524 (2004)
9.261 J.Y. Lee, S.T. Connor, Y. Cui, P. Peumans: Solution-processed metal nanowire mesh transparent electrodes, Nano Lett. **8**, 689–692 (2008) doi:10.1021/nl073296g
9.262 X. Duan, Y. Huang, R. Agarwal, C.M. Lieber: Single-nanowire electrically driven lasers, Nature **421**, 241 (2003)
9.263 F. Qian, Y. Li, S. Gradecak, D.L. Wang, C.J. Barrelet, C.M. Lieber: Gallium nitride-based nanowire radial heterostructures for nanophotonics, Nano Lett. **4**, 1975–1979 (2004)
9.264 V. Dneprovskii, E. Zhukov, V. Karavanskii, V. Poborchii, I. Salamatini: Nonlinear optical properties of semiconductor quantum wires, Superlattice. Microst. **23**(6), 1217–1221 (1998)
9.265 J.C. Johnson, K.P. Knutsen, H. Yan, M. Law, Y. Zhang, P. Yang, R.J. Saykally: Ultrafast carrier dynamics in single ZnO nanowire and nanoribbon lasers, Nano Lett. **4**, 197–204 (2004)
9.266 J.X. Ding, J.A. Zapien, W.W. Chen, Y. Lifshitz, S.T. Lee, X.M. Meng: Lasing in ZnS nanowires grown on anodic aluminum oxide templates, Appl. Phys. Lett. **85**, 2361 (2004)
9.267 J.C. Johnson, H.-J. Choi, K.P. Knutsen, R.D. Schaller, P. Yang, R.J. Saykally: Single gallium nitride nanowire lasers, Nat. Mater. **1**, 106–110 (2002)
9.268 H.J. Choi, J.C. Johnson, R. He, S.K. Lee, F. Kim, P. Pauzauskie, J. Goldberger, R.J. Saykally, P. Yang: Self-organized GaN quantum wire UV lasers, J. Phys. Chem. B **107**, 8721–8725 (2003)
9.269 C.J. Barrelet, A.B. Greytak, C.M. Lieber: Nanowire photonic circuit elements, Nano Lett. **4**, 1981–1985 (2004)
9.270 M. Law, D.J. Sirbuly, J.C. Johnson, J. Goldberger, R.J. Saykally, P. Yang: Ultralong nanoribbon waveguides for sub-wavelength photonics integration, Science **305**, 1269–1273 (2004)
9.271 H. Kind, H. Yan, B. Messer, M. Law, P. Yang: Nanowire ultraviolet photodetectors and optical switches, Adv. Mater. **14**, 158–160 (2002)
9.272 B.M.I. van der Zande, M.R. Böhmer, L.G.J. Fokkink, C. Schöneberger: Colloidal dispersions of gold rods: Synthesis and optical properties, Langmuir **16**, 451–458 (2000)
9.273 B.M.I. van der Zande, G.J.M. Koper, H.N.W. Lekkerkerker: Alignment of rod-shaped gold particles by electric fields, J. Phys. Chem. B **103**, 5754–5760 (1999)
9.274 W.U. Huynh, J.J. Dittmer, A.P. Alivisatos: Hybrid nanorod-polymer solar cells, Science **295**, 2425–2427 (2002)
9.275 I. Åberg, G. Vescovi, D. Asoli: A GaAs nanowire array solar cell with 15.3% efficiency at 1 Sun, IEEE J. Photovolt. **6**, 185–190 (2016)
9.276 J. Wallentin, N. Anttu, D. Asoli, M. Huffman, I. Åberg, M.H. Magnusson, G. Siefer, P. Fuss-Kailuweit, F. Dimroth, B. Witzigmann, H.Q. Xu, L. Samuelson, K. Deppert, M.T. Borgström: InP nanowire array solar cells achieving 13.8% efficiency by exceeding the ray optics limit, Science **339**, 1057–1060 (2013)
9.277 B.X. Tian, T.J. Zheng: Kempa, Y. Fang, N. Yu, G. Yu, J. Huang, C. M. Lieber: Coaxial silicon nanowires as solar cells and nanoelectronic power sources, Nature **449**, 885–889 (2007)
9.278 P. Krogstrup, H.I. Jørgensen, M. Heiss, O. Demichel, J.V. Holm, M. Aagesen, J. Nygard: A. Fontcuberta i Morral: Single-nanowire solar cells beyond the Shockley-Queisser limit, Nat. Photon. **7**, 306–310 (2013)
9.279 B. A. Buchine, F. Modawar, M. R. Black: Nanostructured Devices. US Patent No. 20,100,122,725. (2010)
9.280 L. Hu, G. Chen: Analysis of optical absorption in silicon nanowire arrays for photovoltaic applications, Nano Lett. **7**, 3249–3252 (2007)
9.281 C.K. Chan, H. Peng, G. Liu, K. McIlwrath, X.F. Zhang, R.A. Huggins, Y. Cui: High-performance lithium battery anodes using silicon nanowires, Nat. Nanotechnol. **3**, 31–35 (2008)
9.282 L. Mai, Y. Dong, L. Xu, C. Han: Single nanowire electrochemical devices, Nano Lett. **10**, 4273–4278 (2010) doi:10.1021/nl102845r
9.283 V.P. Oleshko, T. Lam, D. Ruzmetov, P. Haney, H.J. Lezec, A.V. Davydov, S. Krylyuk, J. Cumings, A.A. Talin: Miniature all-solid-state heterostructure nanowire Li-ion batteries as a tool for engineering and structural diagnostics of nanoscale electrochemical processes, Nanoscale **6**(20), 11756 (2014)
9.284 M. Green: U.S. Patent No. 7402829 (U.S. Patent and Trademark Office, Washington DC 2008)
9.285 B. A. Buchine, F. Modawar, M. R. Black: Nanostructured silicon for battery anodes, U.S. Patent No. 8791449. (2014)
9.286 G. E. Loveness, C.I. Stefan, S. Han: Multidimensional electrochemically active structures for battery electrodes, U.S. Patent No. 9172088. (2015)
9.287 C. Liu, E.I. Gillette, X. Chen, A.J. Pearse, A.C. Kozen, M.A. Schroeder, K.E. Gregorczyk, S.L. Bok, G.W. Rubloff: An all-in-one nanopore battery array, Nat. Nanotechnol. **9**, 1031–1039 (2014) doi:10.1038/nnano.2014.247
9.288 J. Qiu, G. Zeng, M.-A. Ha, M. Ge, Y. Lin, M. Hettick, B. Hou, A.N. Alexandrova, A. Javey, S.B. Cronin: Artificial photosynthesis on TiO_2-passivated InP nanopillars, Nano Lett. **15**, 6177–6181 (2015)
9.289 Y. Su, C. Liu, S. Brittman, J. Tang, A. Fu, N. Kornienko, Q. Kong, P. Yang: Single-nanowire photoelectrochemistry, Nat. Nanotechnol. **11**, 609–612 (2016) doi:10.1038/nnano.2016.30
9.290 P. Banerjee, I. Perez, L. Henn-Lecordier, S.B. Lee, G.W. Rubloff: Nanotubular metal–insulator–metal capacitor arrays for energy storage, Nat. Nanotech-

nol. **4**(5), 292–296 (2009)
9.291 Z. Liu, Y. Zhan, G. Shi, S. Moldovan, M. Gharbi, L. Song, L. Ma, W. Gao, J. Huang, R. Vajtai, F. Banhart, P. Sharma, J. Lou, P.M. Ajayan: Anomalous high capacitance in a coaxial single nanowire capacitor, Nat. Commun. (2012) doi:10.1038/ncomms1833
9.292 P.M. Rorvik, T. Grande, M.A. Einarsrud: One-dimensional nanostructures of ferroelectric perovskites, Adv. Mater. **23**, 4007–4034 (2011) doi:10.1002/adma.201004676
9.293 Z.L. Wang: From nanogenerators to piezotronics–A decade-long study of ZnO nanostructures, MRS Bull. **37**, 814–827 (2012) doi:10.1557/mrs.2012.186
9.294 Z.L. Wang, J.H. Song: Piezoelectric nanogenerators based on zinc oxide nanowire arrays, Science **312**, 242–246 (2006) doi:10.1126/science.1124005
9.295 L. Gu, N. Cui, L. Cheng, Q. Xu, S. Bai, M. Yuan, W. Wu, J. Liu, Y. Zhao, F. Ma, Y. Qin, Z. Lin Wang: Flexible fiber nanogenerator with 209 V output voltage directly powers a light-emitting diode, Nano Lett. **13**, 91–94 (2013) doi:10.1021/nl303539c
9.296 J.H. Jung, M. Lee, J.-I. Hong, Y. Ding, C.-Y. Chen, L.-J. Chou, Z.L. Wang: Lead-free $NaNbO_3$ nanowires for a high output piezoelectric nanogenerator, Acs Nano **5**, 10041–10046 (2011) doi:10.1021/nn2039033
9.297 J. Kwon, W. Seung, B.K. Sharma, S.W. Kim, J.H. Ahn: A high performance PZT ribbon-based nanogenerator using graphene transparent electrodes, Energy Environ. Sci. **5**, 8970–8975 (2012) doi:10.1039/c2ee22251e
9.298 C. Falconi, G. Mantinia, A. D'Amico, Z.L. Wang: Studying piezoelectric nanowires and nanowalls for energy harvesting, Sens. Actuat. B-Chem. **139**, 511–519 (2009) doi:10.1016/j.snb.2009.02.071
9.299 G. Mantini, Y.F. Gao, A. D'Amico, C. Falconi, Z.L. Wang: Equilibrium piezoelectric potential distribution in a deformed ZnO nanowire, Nano Res **2**, 624–629 (2009) doi:10.1007/s12274-009-9063-2
9.300 Z. Wang, X. Pan, Y. He, Y. Hu, H. Gu, Y. Wang: Piezoelectric nanowires in energy harvesting applications, Adv. Mater. Sci. Eng. (2015) doi:10.1155/2015/165631
9.301 H.D. Espinosa, R.A. Bernal, M. Minary-Jolandan: A review of mechanical and electromechanical properties of piezoelectric nanowires, Adv. Mater. **24**, 4656–4675 (2012) doi:10.1002/adma.201104810
9.302 C.-T. Huang, J. Song, W.-F. Lee, Y. Ding, Z. Gao, Y. Hao, L.-J. Chen, Z.L. Wang: GaN nanowire arrays for high-output nanogenerators, J. Am. Chem. Soc. **132**, 4766–4771 (2010) doi:10.1021/ja909863a
9.303 C.T. Huang, J. Song, C.-M. Tsai, W.-F. Lee, D.-H. Lien, Z. Gao, Y. Hao, L.-J. Chen, Z.L. Wang: Single-InN-nanowire nanogenerator with upto 1 V output voltage, Adv. Mater. **22**, 4008–4013 (2010) doi:10.1002/adma.201000981
9.304 Y.F. Lin, J. Song, Y. Ding, S.Y. Lu, Z.L. Wang: Alternating the output of a CdS nanowire nanogenerator by a white-light-stimulated optoelectronic effect, Adv. Mater. **20**, 3127–3130 (2008) doi:10.1002/adma.200703236
9.305 M.-Y. Lu, J. Song, M.-P. Lu, C.-Y. Lee, L.-J. Chen, Z.L. Wang: ZnO-ZnS heterojunction and ZnS nanowire arrays for electricity generation, Acs Nano **3**, 357–362 (2009) doi:10.1021/nn800804r
9.306 Y.F. Lin, J. Song, Y. Ding, S.Y. Lu, Z.L. Wang: Piezoelectric nanogenerator using CdS nanowires, Appl. Phys. Lett. **92**, 022105 (2008) doi:10.1063/1.2831901
9.307 S. Xu, Y. Qin, C. Xu, Y. Wei, R. Yang, Z.L. Wang: Self-powered nanowire devices, Nat. Nanotechnol. **5**, 366–373 (2010) doi:10.1038/nnano.2010.46
9.308 S. Xu, B.J. Hansen, Z.L. Wang: Piezoelectric-nanowire-enabled power source for driving wireless microelectronics, Nat. Commun. (2010) doi:10.1038/ncomms1098
9.309 Z.Y. Wang, J. Hu, A.P. Suryavanshi, K. Yum, M.F. Yu: Voltage generation from individual $BaTiO_3$ nanowires under periodic tensile mechanical load, Nano Lett. **7**, 2966–2969 (2007) doi:10.1021/nl070814e
9.310 R.S. Yang, Y. Qin, L.M. Dai, Z.L. Wang: Power generation with laterally packaged piezoelectric fine wires, Nat. Nanotechnol. **4**, 34–39 (2009) doi:10.1038/nnano.2008.314
9.311 Z. Wang, H. Gu, Y. Hu, K. Yang, M. Hu, D. Zhoua, J. Guan: Synthesis, growth mechanism and optical properties of $(K,Na)NbO_3$ nanostructures, Crystengcomm **12**, 3157–3162 (2010) doi:10.1039/c000169d
9.312 G.A. Zhu, R.S. Yang, S.H. Wang, Z.L. Wang: Flexible high-output nanogenerator based on lateral ZnO nanowire array, Nano Lett. **10**, 3151–3155 (2010) doi:10.1021/nl101973h
9.313 J.Y. Chang, M. Domnner, C. Chang, L.W. Lin: Piezoelectric nanofibers for energy scavenging applications, Nano Energy **1**, 356–371 (2012) doi:10.1016/j.nanoen.2012.02.003
9.314 X. Chen, S.Y. Xu, N. Yao, Y. Shi: 1.6 V nanogenerator for mechanical energy harvesting using PZT nanofibers, Nano Lett. **10**, 2133–2137 (2010) doi:10.1021/nl100812k
9.315 Y.F. Hu, Y. Zhang, C. Xu, G.A. Zhu, Z.L. Wang: High-output nanogenerator by rational unipolar assembly of conical nanowires and its application for driving a small liquid crystal display, Nano Lett. **10**, 5025–5031 (2010) doi:10.1021/nl103203u
9.316 L. Lin, C. Lai, Y. Hu, Y. Zhang, X. Wang, C. Xu, R.L. Snyder, L.J. Chen, Z.L. Wang: High output nanogenerator based on assembly of GaN nanowires, Nanotechnology (2011) doi:10.1088/0957-4484/22/47/475401
9.317 L.A. Bauer, N.S. Birenbaum, G.J. Meyer: Biological applications of high aspect ratio nanoparticles, J. Mater. Chem. **14**, 517–526 (2004)
9.318 Y. Cui, Q. Wei, H. Park, C. Lieber: Nanowire nanosensors for highly sensitive and selective detection of biological and chemical species, Science **293**, 1289–1292 (2001)
9.319 J. Hahm, C. Lieber: Direct ultra-sensitive electrical detection of DNA and DNA sequence variations using nanowire nanosensors, Nano Lett. **4**, 51–54 (2004)
9.320 J. Zhoua, C.S. Lao, P. Gao, W. Mai, W.L. Hughes, S. Zhi Deng, N.S. Xu, Z.L. Wang: Nanowire as picogram balance at workplace atmosphere, Solid State

Commun. **139**, 222–226 (2006)
9.321 M.S. Hanay, S. Kelber, A.K. Naik, D. Chi, S. Hentz, E.C. Bullard, E. Colinet, L. Duraffourg, M.L. Roukes: Single-protein nanomechanical mass spectrometry in real time, Nat. Nanotechnol. **7**, 602–608 (2012) doi:10.1038/nnano.2012.119.
9.322 M. L. Roukes, M. S. Hanay, S. Kelber, A. Naik: US Patent Application No. 13/890,087 (2013)
9.323 D.J. Sirbuly, M. Law, H. Yan, P. Yang: Semiconductor nanowires for subwavelength photonics integration, J. Phys. Chem. B **109**, 15190–15213 (2005)
9.324 R. Yan, J. Park, Y. Choi, C. Heo, S. Yang, L.P. Lee, P. Yang: Nanowire-based single cell endoscopy, Nat. Nanotechnol. **7**, 191–196 (2012)
9.325 Y. Huang, Y. Fang, Z. Zhang, L. Zhu, M. Sun: Nanowire-supported plasmonic waveguide for remote excitation of surface-enhanced Raman scattering, Light Sci. Appl. **3**, e199 (2014) doi:10.1038/lsa.2014.80
9.326 S.S.P. Parkin, M. Hayashi, L. Thomas: Magnetic domain-wall racetrack memory, Science **320**, 190–194 (2008) doi:10.1126/science.1145799
9.327 D.A. Allwood, G. Xiong, C.C. Faulkner, D. Atkinson, D. Petit, R.P. Cowburn: Magnetic domain-wall logic, Science **309**, 1688–1692 (2005) doi:10.1126/science.1108813
9.328 D. Atkinson, D.A. Allwood, G. Xiong, M.D. Cooke, C.C. Faulkner, R.P. Cowburn: Magnetic domain-wall dynamics in a submicrometre ferromagnetic structure, Nat. Mater. **2**, 85–87 (2003) doi:10.1038/nmat803
9.329 R.D. McMichael, M.J. Donahue: Head to head domain wall structures in thin magnetic strips, IEEE Trans. Magnet. **33**, 4167–4169 (1997) doi:10.1109/20.619698
9.330 T. Ono, H. Miyajima, K. Shigeto, K. Mibu, N. Hosoito, T. Shinjo: Propagation of a magnetic domain wall in a submicrometer magnetic wire, Science **284**, 468–470 (1999) doi:10.1126/science.284.5413.468
9.331 D.A. Allwood, G. Xiong, M.D. Cooke, C.C. Faulkner, D. Atkinson, N. Vernier, R.P. Cowburn: Submicrometer ferromagnetic NOT gate and shift register, Science **296**, 2003–2006 (2002) doi:10.1126/science.1070595
9.332 C.C. Faulkner, D.A. Allwood, M.D. Cooke, G. Xiong, D. Atkinson, R.P. Cowburn: Controlled switching of ferromagnetic wire junctions by domain wall injection, IEEE Trans. Magnet. **39**, 2860–2862 (2003) doi:10.1109/tmag.2003.816247